THE UNIVERSITY *of* EDINBURGH

Search for new physics via low-energy electron recoils with the LZ Experiment and low background technique enhancements with the Boulby Laboratory

Anh Van Thi Nguyen

Doctor of Philosophy
The University of Edinburgh
November 2024

Abstract

The fundamental nature of dark matter is one of the greatest mysteries in physics. Compelling evidence indicates that dark matter constitutes 84% of the total matter density in the universe, yet the detection of its constituent remains elusive. The LUX-ZEPLIN (LZ) experiment, located in Sanford Underground Research Facility, employs several tonnes of xenon in a dual-phase time projection chamber to conduct direct searches for dark matter particles. Recently, the LZ experiment set a world-leading limit on interactions between nucleons and weakly interacting massive particles (WIMPs), one of the most promising dark matter candidates.

To ensure the detector's stability and maintain data integrity, the LZ experiment implements extensive monitoring and quality assurance measures including the development of online monitoring tools, routine calibrations, and a structured shift system across collaborating institutes. This author's contributions include assuring PMT quality, conducting grid testing campaign and calibration tasks, and serving as a member of the PMT supervision team.

This thesis investigates the sensitivity and versatility of the LZ detector in extending its scientific programme beyond WIMPs to search for other novel physics from the hidden sector, such as axion-like particles, hidden photons, and mirror dark matter. All dark matter models discussed are expected to produce electron recoil (ER) interactions in the liquid xenon chamber and generating signals in the low-energy ER channels. The results rule out the areas of allowed parameter space for these signals using the LZ's experiment first exposure of 60 live days and a fiducial mass of 5.5 tonnes. Future science-runs from LZ with higher exposure will further improve the sensitivities of these searches. A crucial aspect in the field of direct detection is the continuous improvement of detector sensitivity. This often involves developing material assaying techniques to reduce background and providing accurate characterisations of residual radio-contaminants in the detector. The Boulby UnderGround Screening (BUGS)

facility is one of the few material screening facilities in the world that support rare-event search experiments such as LZ. Works have been conducted to improve the Boulby Underground Laboratory's overall assaying capabilities through the addition of the commercially manufactured XIA UltraLo-1800 alpha particle counters. These findings demonstrate how the XIA UltraLo-1800 are able to enhance the material assaying techniques at Boulby. These efforts summarised above, in ruling out allowed parameter space for dark matter models and improving low background techniques for rare event searches, aspire to unravel the characteristics of dark matter.

Lay summary

Dark matter is one of the biggest unsolved puzzles in science. It makes up about 84% of all the matter in the universe, yet we still don't know what it's made of or how to detect it directly. The LUX-ZEPLIN (LZ) experiment is a global collaboration to search for dark matter using a highly sensitive detector filled with liquid xenon located deep underground in South Dakota. Recently, the LZ experiment set a new global benchmark for detecting weakly interacting massive particles (WIMPs), which are one of the leading candidates for dark matter.

To ensure the detector works smoothly and produces reliable results, the LZ team monitors its performance constantly, runs regular tests, and coordinates shifts across research teams worldwide. This author's contributions to the project include testing and maintaining key parts of the detector, such as its light sensors, and helping ensure the system stays calibrated and ready for data collection.

This thesis explores other potential types of dark matter, including axion-like particles, hidden photons, and mirror dark matter. These types of dark matter are expected to leave specific signals in the detector which we search for in the data. Using 60 days' worth of data collected by LZ, this author's work has helped rule out certain possibilities for how these particles could behave, narrowing down where we should look in the future. Upcoming runs of the experiment with more data will allow even better chances of finding dark matter.

Another important part of this work is improving how we reduce background noises in the detector - signals that come from other sources, not dark matter. This involves developing better ways to test and clean the materials used in the experiment. At the Boulby Underground Laboratory in the UK, this author worked on improving these tests by using advanced equipment to measure and reduce contamination. Together, these efforts help create cleaner, more sensitive experiments, bringing us closer to uncovering the true nature of dark matter.

Declaration

I declare that this thesis was composed by myself, that the work contained herein is my own except where explicitly stated otherwise in the text, and that this work has not been submitted for any other degree or professional qualification except as specified.

Parts of this work have been published in [1, 2].

(*Anh Van Thi Nguyen, November 2024*)

Acknowledgements

Acknowledging everyone is impossible, but I am deeply grateful to each person who has been there for me and supported me throughout this journey.

First and foremost, I would like to express my immense gratitude to my two supervisors, Alex Murphy and Sally Shaw. Without their invaluable guidance and unwavering support, completing this PhD would not have been possible. Not only are Alex and Sally excellent physicists who provided countless insights into my work, but they are also two of the kindest supervisors one could hope for.

Within my EdiDM group, I must extend my thanks to my friend Harkirat for all the support he has provided. His kindness and caring nature have meant so much to me throughout this journey, and I am deeply grateful for his friendship. My thanks also go to Xinran, for being the coolest brotherly postdoc and landlord. Along with Kaan, Alberto, Ellie, Elizabeth, and Huan, it was truly a pleasure to be part of the EdiDM group.

From the LZ collaboration, I want to thank Tomasz, Dev, Dan, and David — you were all wonderful to work with and provided me with so much guidance. To my LZ friends Anna and Eli, thank you for being the people I could always talk to about anything and everything. Above all, I extend my deepest gratitude to Ayham for being the most considerate, benevolent, and kind friend, brother, and mentor. Your knowledge and care have helped me immeasurably. And yes, Ayham, please "get me out".

To all the amazing friends I made in Edinburgh. Han, for being such a wonderful flatmate whose opinion I greatly respect and for bringing Cabbage into our lives. My friend Jiaoyang, with whom I shared so much in common — our personalities are a match made in heaven, and we grew so close, even though we only overlapped for three months. William, for being such a fantastic "babushka" and friend. You made my coffee breaks far too enjoyable, which might have been why my PhD took this long! Finally, to my friends John, Filippo, Sam, Matthew, and Raj, thank you for being such wonderful companions. You guys have made it incredibly hard for me to part with Edinburgh.

To my dearest friends: Claude, Vanessa, Harry, Ulya, Eva and Mohit, you brought endless joy and laughter into my life, and for that, I am eternally thankful. Adam,

I am forever grateful for your guidance and friendship.

I am deeply grateful for two babies, Aisha and Dorsa, for all the love and support they have given me over the years. I cannot imagine what my life would be like without them. To my whole family, especially my two dearest sisters, chi Hai and chi Dao, thank you for your unwavering support and care throughout my life. I could not ask for more. Special gratitude and deepest love go to my mother, who has always been the anchor in my life.

Last but not least, thank you to my love, Sihyuk, for always being by my side and for your unwavering patience, support and love.

Contents

List of Figures

List of Tables

Introduction

Chapter 1 summarizes the evidence supporting the existence of dark matter, detailing its inferred properties and introducing several prominent dark matter candidates. This is followed by an overview of complementary dark matter searches, with a focus on direct detection methods.

Chapter 2 delves into the physics underlying xenon detectors, particularly dual-phase time projection chambers (TPCs) like the LZ detector. It explains how signals are generated within these detectors and outlines the operational principles and subsystems of the LZ experiment, highlighting its design optimisation for detecting rare dark matter events.

Chapter 3 details the efforts and tools employed to maintain detector stability and data quality, emphasising the author's contributions to testing, monitoring, and calibrating photomultiplier tubes.

Chapter 4 summarizes the results from LZ's first WIMP search.

Chapter 5 delves into the analysis of dark matter models that are expected to induce signals in the low-energy electron recoil channel in the LUX-ZEPLIN (LZ) experiment, focusing on axion-like particles (ALPs), hidden photons (HPs), and mirror dark matter. Conducted by the author, these analyses build upon the WIMP-search analysis framework.

Chapter 6 focuses on enhancing the low-background assay capabilities at the Boulby Laboratory through the integration of XIA UltraLo-1800 alpha counters. The author is responsible for developing Monte Carlo simulations for the UltraLo-1800 detector and analysing all samples assayed at Boulby.

Chapter 1

Overview of dark matter

The history of dark matter is extensive and complex, dating back more than a century. Theories among astronomers as early as the 19th century suggested that our cosmos is filled with 'unseen' matter. Astronomers explored the topic of whether these dark clouds or 'nebulae' were caused by absorbing matter along the line-of-sight or by a paucity of stars.

In 1904, Lord Kelvin was one of the first to propose the idea of dynamically estimating the mass of the galaxy using the velocities of stars [3]. Poincaré was impressed by the idea and applied Lord Kelvin's concept in 1906 to estimate the mass of the Milky Way. He pointed out that if Lord Kelvin's estimate of the velocity dispersion was identical to what was observed, then there was probably a similar or lesser amount of unseen matter compared to visible matter. His measurements suggested the presence of non-luminous matter, which he coined as 'dark matter' [4].

The pieces of evidence from the last century that point to the existence of dark matter will be covered in detail in the next section. An outline of some well-known dark matter candidates and a synopsis of some of the methods used by various experiments to look for dark matter are then provided in the later sections in this chapter.

1.1 Evidence for dark matter

1.1.1 Velocity dispersion

One of the earliest evidence for dark matter appeared in 1933 [5, 6] when the astronomer Fritz Zwicky used the virial theorem. This theorem relates the total kinetic energy to the total potential energy of a stable system, to analyse the Coma Cluster and calculate its mass based on the movements of the nebulae at its periphery. He assumed that, on average, the global cluster of N nebulae is uniformly distributed inside a sphere of radius R with roughly equal mass m and velocity v. The theorem relates the total kinetic energy T to the total potential energy U of a stable system as follows:

$$T = \frac{1}{2}|U| = \frac{1}{2}\sum_{i=1}^{N} m_i v_i^2 = \frac{1}{2}M\sigma^2, \tag{1.1}$$

$$|U| = \sum_{i=1}^{N} < \mathbf{F}_i \cdot \mathbf{r}_i >, \tag{1.2}$$

where M is the mass of the cluster, σ is the velocity dispersion, $\mathbf{F}_i$ and $\mathbf{r}_i$ are the gravitational force and distance from the center of mass for individual nebula i, respectively. Combining everything, Zwicky obtained a lower bound for the mass of the Coma cluster:

$$M > \frac{5R\sigma}{3G}, \tag{1.3}$$

where G is the gravitational constant. Using the mass-luminosity relation, Zwicky's calculations show that the cluster contains approximately 400 times more mass than the observed luminous mass. Based on this, Zwicky inferred the existence of unseen matter that provided the mass and associated gravitational attraction holding the cluster together. Zwicky's findings sparked debate and further investigation. In the 1950s, more publications reported higher mass-to-light ratios for various galaxy clusters [7], further supporting the presence of dark matter.

1.1.2 Galactic rotational curves

After the ripple in evidence from velocity dispersion, a shift to studying galactic rotation curves in the 1970s offered additional evidence for the existence of dark matter. According to Newtonian dynamics, gravity is proportional to centripetal acceleration for objects in circular orbits. This allows us to derive an expression that relates the velocity of an object in orbit of a galaxy with a mass distribution, $M(r)$, to its radial distance from the galactic center r as:

$$v(r) = \sqrt{\frac{GM(r)}{r}}, \tag{1.4}$$

where G is the gravitational constant.

For a galaxy like the Andromeda Galaxy (M31), it was expected that the velocity would decrease with radius as $v \propto \frac{1}{r^{1/2}}$ beyond the region where most of the luminous mass is situated. However, Rubin and Ford showed that this was not the case from their measurements of the Andromeda Galaxy (M31) [8] as shown in Figure 1.1. From their observations, the velocity approaches a constant value at a large radius [8]. This trend was also observed in numerous other galaxies [9, 10], such as the NGC 3198 barred spiral galaxy as shown in Figure 1.2. This can be explained if another mass component caused the total mass distribution to be $M(r) \propto r$, which is introduced as a spherical dark matter halo surrounding the galaxy.

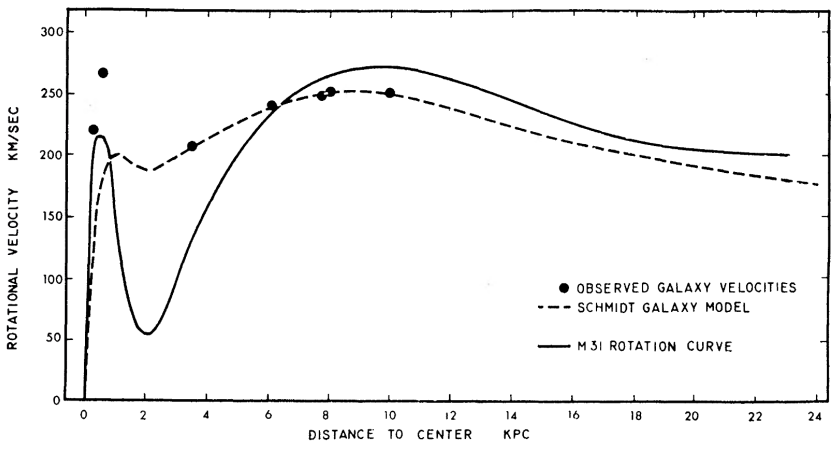

Figure 1.1 *Comparison of rotation curves for M31 and the Galaxy, as a function of distance from the centre. This is taken from [8].*

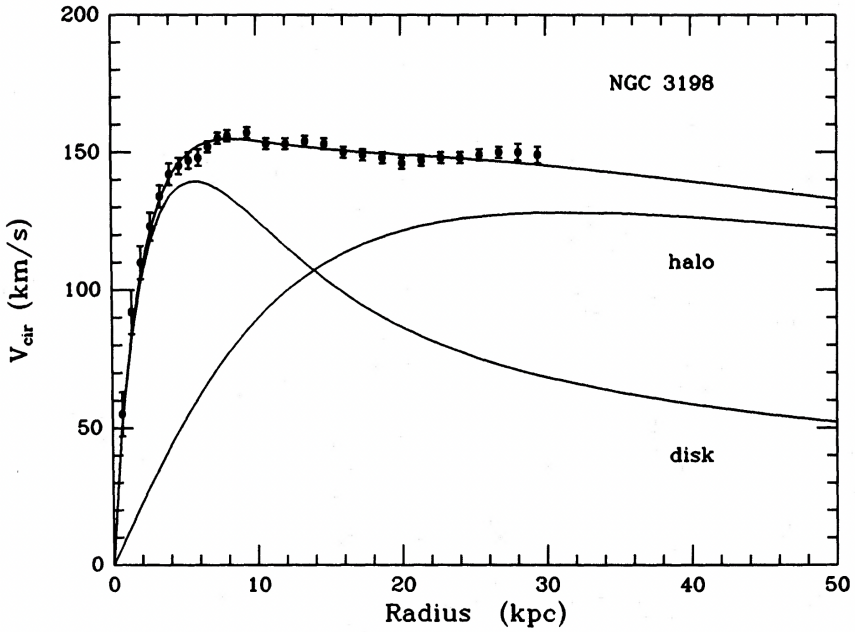

Figure 1.2 *Fits of the rotation curves for NGC 3198, a barred spiral galaxy in the Virgo Supercluster, are shown for its maximum disk mass and dark matter halo, plotted against its fitted measured data points. The plot is taken from [11].*

1.1.3 Gravitational lensing

One of the major pieces of evidence for the existence of dark matter comes from measurements of cluster mass using gravitational lensing [12]. Predicted by general relativity [13], gravitational lensing is the distortion in the path of light caused by an intervening massive object that distorts the spacetime between the source and observer. Effectively, the massive object acts as a lens, deflecting multiple light rays and converging them towards a point. The extent of the lensing depends on the relative positions of the source, observer, mass, and shape of the intervening object. By analysing the degree of these distortions, the mass of the intervening object can be deduced. To summarise, there are two main types of gravitational lensing of interest:

- **Strong lensing:** This occurs when the gravitational field of an intervening massive object is strong enough to produce highly distorted and multiple, magnified images and arcs of the background source. Strong lensing is a rare phenomenon as the distant galaxy or quasar must be closely aligned with the intervening object to create multiple, highly distorted images of the background object. To date, strong lensing has been used to study how

dark matter is distributed in galaxies and clusters [14, 15].

- **Weak lensing:** Weak lensing results from smaller intervening masses and larger separations. While the lensing effect may not be strong enough to produce multiple images or arcs, it can still distort background sources by stretching and magnifying them. If the sources, such as a known cluster of galaxies, are well understood in terms of their shape and size, the statistics of these sources can be used to deduce information about the lens. Weak lensing is a valuable statistical method for measuring the distribution of mass—both luminous and dark—in the Universe.

Dark matter can cause normal matter to accumulate, leading to the formation of stars and galaxies. Gravitational lensing detects its influence by observing how the gravity of massive galaxy clusters, which contain dark matter, bends and distorts the light from more distant galaxies located behind the cluster.

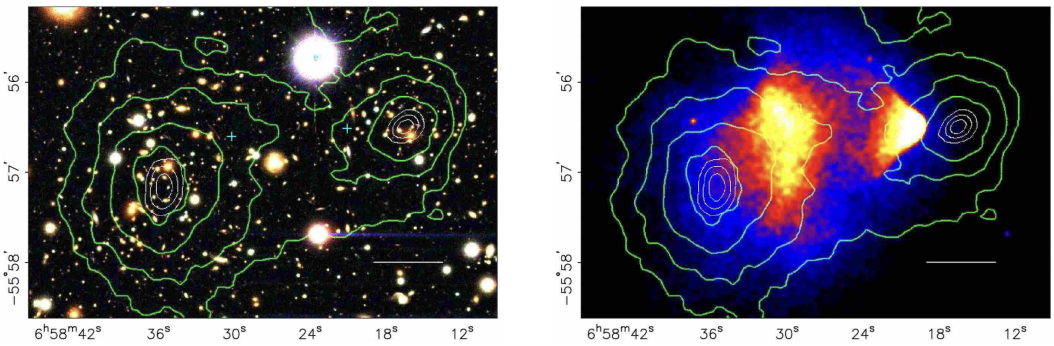

Figure 1.3 *The images depict the mapping of the Bullet cluster captured by the Chandra X-ray Observatory. The white bars indicate 200 kpc at the distance of the cluster. The green contours in both images are the weak lensing signal reconstruction, with the inferred mass distribution for the left image depicted in blue on the right image. These are taken from [16].*

One of the most prominent pieces of evidence for dark matter comes from the study of the Bullet cluster mass using weak lensing [17]. As depicted in Figure 1.3, weak lensing reveals that the distribution of mass in the Bullet cluster does not align with the centroid of its luminous matter. Instead, this suggests that most of the mass does not come from the visible component of the cluster but from dark matter components.

1.1.4 The CMB and Large Scale Structure

The cosmic microwave background (CMB) radiation is a remnant of the early Universe and serves as evidence that supports the Big Bang theory and our understanding of the Universe. It was first predicted in the 1940s to explain the expanding Universe and was then discovered in 1965 by Wilson and Penzias [18].

The CMB is composed of microwave photons originating from the thermal radiation left over from the epoch of recombination [19]. Before the recombination period, these photons were coupled to the ionised plasma and were constantly scattered off free electrons. Approximately 380,000 years after the Big Bang, the Universe started to cool, causing the free protons and electrons to form hydrogen atoms. During that time, the photons decoupled from the plasma and started propagating through the Universe. These CMB photons are visible today but have been redshifted significantly due to the expansion of the Universe over billions of years. The redshift of the CMB is a direct consequence of the expanding Universe and provides a powerful tool to study the evolution of the Universe and the formation of large-scale structures.

Although the CMB is nearly isotropic in temperature and appears uniform on large scales, tiny fluctuations or anisotropies in temperature exist at a level of one part per 100,000 [20]. These fluctuations are believed to be caused by quantum fluctuations in the density of matter in the early Universe, caused by the conflicts between radiation pressure and gravitational attractions in the photon-baryon plasma, also known as the acoustic oscillations. Measurements of the anisotropies were conducted by experiments like WMAP in the 2000s [21] and then by the Planck experiment [22] to determine cosmological parameters using the CMB power spectrum.

The power spectrum in Figure 1.4 is produced by mapping the CMB across the sky with unprecedented precision and then decomposing the CMB map into spherical harmonics to separate it into various angular scales. A larger multipole moment ℓ represents a smaller angular scale and vice versa.

The angular spectrum can be fitted to a cosmological model to determine the values of its parameters; in this case, it is well described by the ΛCDM model, as outlined in Section 1.1.5. The first peak provides information about the curvature of the Universe, the second peak reflects the ordinary matter content, and the third peak is associated with the amount of dark matter.

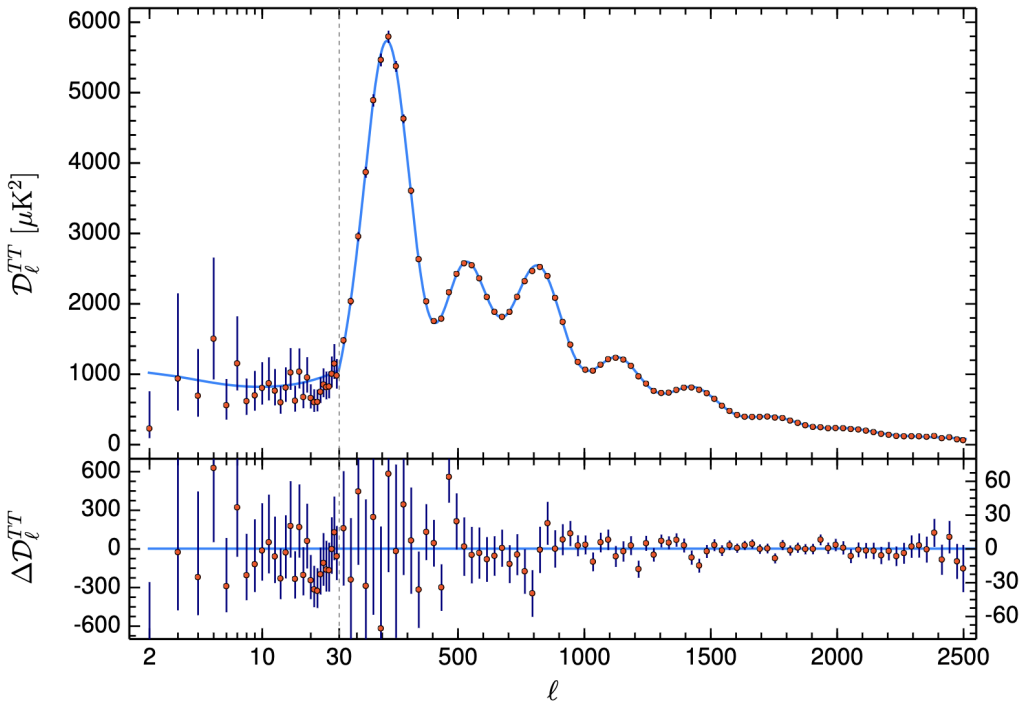

Figure 1.4 *The 2018 results from the Planck collaboration [22] display the power spectrum of temperature anisotropies plotted against angular scale, expressed in terms of the spherical multipole moment ℓ. The data is fitted with the ΛCDM model (blue curve), and the residuals from this model are depicted in the lower panel. The error bars represent $\pm 1\sigma$, and a dotted vertical line indicates the transition from logarithmic to normal scales in ℓ values.*

Experiments such as WMAP and Planck have employed this approach to extract cosmological parameters from CMB anisotropies by fitting the six independent free parameters of the ΛCDM model. These parameters are the physical baryon density, physical dark matter density, dark energy density, scalar spectral index, curvature fluctuation amplitude, and reionisation optical depth. Results for energy density parameters using the Planck CMB power spectrum, combined with lensing reconstruction, are shown in Table 1.1. These results imply that dark matter accounts for approximately 84% of the matter density of the Universe, given that it contributes a fraction of 0.261/0.315 to the total matter density.

At the beginning of the Universe, infinitesimal quantum fluctuations gave rise to variations in density across the primordial soup of elementary particles and radiation. Imprinted during cosmic inflation, these fluctuations were stretched as the Universe expanded and laid the groundwork for the formation of the cosmic web. Over billions of years, regions of higher density attracted more matter through gravitational forces, leading to the formation of galaxies and galaxy

Table 1.1 *The energy density parameters using the latest Planck 2018 results of the ΛCDM model [23].*

Parameter	Name	Value
Ω_b	Baryonic matter density	0.04898 ± 0.00031
Ω_{dm}	Dark matter density	0.26070 ± 0.00199
Ω_m	Total matter density	0.315 ± 0.007

clusters, while voids developed in regions with lower matter density. Together, these gravity-driven processes gave rise to what is known as the Large-Scale Structure (LSS) of the Universe, on scales of ∼1–3 megaparsecs (Mpc), where galaxies are observed to be in coherent patterns such as groups and clusters.

Dark matter, comprising a significant portion of the Universe's mass, played a pivotal role in sculpting the LSS [24]. Unlike baryonic matter, dark matter does not interact via electromagnetic forces but exerts gravitational influence. Its gravitational pull attracted ordinary matter, including gas and dust, leading to the formation of proto-galactic clouds and subsequent galaxies and galaxy clusters.

Studying the LSS not only unveils the cosmic history but also deepens our understanding of fundamental cosmological principles. The intricate interplay between quantum fluctuations, dark matter, and gravitational dynamics elucidated through simulations like the Millennium Simulation [25] enriches cosmological models and underscores the significance of dark matter in cosmic evolution.

1.1.5 The ΛCDM model

Data collected from CMB observations can be used to constrain and fit different cosmological models, such as the ΛCDM model mentioned previously. The ΛCDM model has been very successful because it can provide explanations for observed phenomena like acoustic oscillations, Large Scale Structure (LSS), and the abundances of hydrogen, deuterium, and helium [26].

This is a mathematical model of Big Bang cosmology, predicated on the idea that the Universe began as a hot big bang and then expanded to become statistically uniform on large scales. The cosmological constant for dark energy, or Λ, is assumed to be the cause of the Universe's observed accelerated expansion. This model assumes that the energy density of dark energy is constant across space.

The CDM part stands for 'Cold Dark Matter', referring to a type of dark matter that moves at non-relativistic speeds and interacts with normal matter only via gravity. Together with dark energy, this theory includes both Standard Model (SM) baryonic matter and dark matter to model the evolution of the Universe, successfully explaining the formation of the large-scale structure of the Universe we observe today.

1.2 Dark matter candidates

This section will first provide a summary of the fundamental characteristics that dark matter candidates are likely to possess, as determined by available data and observations. Subsequently, a brief overview of some of the most popular dark matter candidates will be discussed.

1.2.1 Properties

From the astrophysical evidence collected and discussed in the previous sections, several conclusions can be drawn about the basic properties of proposed dark matter candidates.

- **Dark:** It is known that dark matter does not emit or absorb light, making it unobservable by conventional means. This implies that its coupling to photons must be very weak or essentially non-existent. Based on the anisotropies of the CMB, even a small millicharge for dark matter would result in its coupling to the photon-baryon plasma in the early Universe. However, if this were the case, the density perturbations of dark matter would have been washed out due to radiation pressure and photon diffusion during recombination. Therefore, dark matter must have been decoupled at recombination, allowing us to set constraints on ϵ, the ratio of the dark matter to electronic charge, to be less than 10^{-6} and 10^{-4} for dark masses of 1 GeV and 10 TeV, respectively [27, 28].
- **Cold dark matter (CDM):** The observed large-scale structure implies that during the formation of the structure, dark matter must have been non-relativistic; otherwise, the structure would have washed out, resulting in a Universe with a different structure than what we observe now. Cold

dark matter (CDM) is a fundamental assumption in the ΛCDM model, leading to constraints on the masses of thermally produced dark matter being less than or equal to keV [29]. However, non-thermal production of lighter dark matter particles is also feasible. Discrepancies such as the erroneous overestimation of subhalos' proportions [30, 31] have driven the exploration of alternate models like warm dark matter [32].

- **Stable/long-lived:** In order for dark matter to contribute to the formation of the observed large-scale structure in the Universe today, it must have a lifetime comparable to the age of the Universe. Astrophysical experiments such as MAGIC have set limits on the decay lifetime to be longer than approximately 10^{26} seconds using their 400 hours of data [33].

- **Collisionless:** Interactions between dark matter particles, whether among themselves or with ordinary matter, primarily occur through gravity, and potentially, via the weak force. The collisionless nature of dark matter helps explain its role in forming the cosmic web, where dark matter connects massive galaxy clusters without dissipating or losing energy through collisions. Observations of bullet cluster mergers have set upper bounds on dark matter self-interaction cross sections at a 95% confidence level to be $\sigma/m < 0.47$ cm^2/g [34].

- **Non-baryonic:** The precise measurements of the CMB anisotropies and predictions from Big Bang nucleosynthesis models [35] indicate that the density of baryonic matter accounts for only about 5% of the Universe's total energy density. Dark matter must be non-baryonic in nature since its energy density is about five times greater than that of baryonic matter.

Some models incorporate properties such as charge or self-interactions, such as dark matter from the hidden sector that will be discussed later on. However, these models are subject to strong constraints or require other mechanisms to explain their properties.

1.2.2 MACHOs

MACHO, also known as the "Massive Astrophysical Compact Halo Object," was one of the first dark matter candidates to be postulated. This term refers to any astronomical body that floats through space and is not connected to any planet.

Examples of MACHO candidates are white dwarfs, neutron stars, and primordial black holes [36].

In the past twenty years, a variety of observations and ideas have eliminated MACHOs as the primary component of the Milky Way's dark matter halo. Firstly, HST data and Hipparcos parallax data were utilised to demonstrate that brown dwarfs and low mass stars, often known as substellar objects, could not be the main source of dark matter in the Milky Way [37, 38]. Later on, two microlensing experiments (MACHO [39] and EROS [40]) showed that MACHOs less massive than 0.1 $M_\odot$ would contribute insignificantly to the total energy density of the Milky Way. There is a detection of a roughly 15% halo fraction made up of ≈ 0.5 $M_\odot$ stellar remnants such as white dwarfs. This signifies that while white dwarfs, one of the MACHO candidates, could contribute to the dark matter halo, their contribution is significant but not sufficient to account for all the dark matter in our galaxy.

1.2.3 Weakly Interacting Massive Particles

Weakly interacting massive particles (WIMPs) are one of the favourite dark matter candidates within the astro-particle physics community. One of the main reasons is their ability to reproduce the correct relic abundance of dark matter observed today. In the early Universe, dark matter was thought to be in thermal equilibrium with the primordial plasma of particles. As the Universe expanded and cooled, these particles would have "frozen out" of equilibrium when their production rate could no longer compete with the Hubble expansion rate[1]. This freeze-out point constrains the relic density of cold dark matter [41] to have average annihilation cross section of $\langle \sigma v \rangle \propto 3 \times 10^{-26}$ $cm^3 s^{-1}$. Remarkably, for weakly interacting particles with masses in the range of a few GeV/c^2 to several TeV/c^2, this relic density is consistent with the observed dark matter density. This coincidence is often referred to as the "WIMP miracle" [42] and it connects particle physics with cosmological observations.

Additionally, WIMPs also meet the requirements of being stable and weakly interacting, meaning they only interact with Z and W bosons but not photons or gluons. There are many WIMP candidates arising from various theoretical

[1]Also known as the Hubble parameter H, it is the characteristic expansion rate of the Universe and is time-dependent; as such, it is approximately of the order of the inverse of the age of the Universe.

frameworks, such as the neutralino from supersymmetry (SUSY) [43] and the Lightest Kaluza-Klein (LKK) [44] from Universal Extra Dimensions (UED) [45]. Overall, WIMP candidates are well-motivated from the point of view of particle physics and relic density measurements, and the experimental search for WIMPs is still ongoing.

1.2.4 Neutrinos

Neutrinos - fundamental particles that are electrically neutral, extremely light, and weakly interacting - were once considered promising candidates for dark matter. Among the most abundant particles in the Universe, they were produced in vast quantities during the Big Bang and continue to be produced in various astrophysical processes, such as nuclear reactions in stars and supernovae. Their sheer number density suggests that they could contribute significantly to the overall mass-energy of the Universe. Additionally, the existence of a cosmic neutrino background (CνB) [46], analogous to the cosmic microwave background (CMB), implies that neutrinos have been present since the early Universe and have permeated the cosmos ever since.

Although neutrinos satisfy all the requirements, their relativistic speed (hot) implies that the large-scale structures we see today would not exist as primordial fluctuations would have happened. According to the latest KATRIN results [47], the total neutrino relic density is roughly $\Omega_\nu h^2 < 0.026$. However, given the Planck collaboration's measurement of dark matter density, $\Omega_{\mathrm{dm}} h^2 = (0.120 \pm 0.001)$ [22], the total neutrino relic density accounts for only approximately 21.7% of the total dark matter density. This indicates that neutrinos are not abundant enough to constitute a significant portion of dark matter, suggesting they are not the only candidates.

1.2.5 Axions and Axion-like Particles

Axions are pseudo-Nambu-Goldstone bosons motivated by the Peccei-Quinn solution to solve the strong CP problem [48]. Currently, axions are expected to have masses ranging from $\mu\mathrm{eV/c^2}$ to $\mathrm{meV/c^2}$ [49], which places them in the category of cold dark matter candidates. This classification is essential for explaining the Universe's large-scale structure. Moreover, axions interact weakly

with ordinary matter and radiation, aligning with the non-luminous and elusive nature of dark matter.

Axions can be produced through various mechanisms in the early Universe. One prominent method is the misalignment mechanism [50], where axions emerge from the initial conditions of the axion field. This process can yield a relic density consistent with the observed dark matter density. Additionally, axions can form from the decay of topological defects such as cosmic strings and domain walls, which appear during phase transitions in the early Universe. The production mechanisms allow axions to be non-relativistic (cold) when they decouple, making them suitable for forming structures like galaxies and galaxy clusters. These observations necessitate a form of matter that is abundant, non-luminous, and non-relativistic—attributes that axions possess.

Axion-like particles (ALPs) are hypothetical particles similar to axions but not necessarily tied to the solution of the strong CP problem like quantum chromodynamics (QCD) axions. While axions specifically arise from the Peccei-Quinn theory as a solution to the strong CP problem, ALPs are more general in nature and can arise from various extensions of the Standard Model of particle physics. A more in-depth discussion of ALPs and their potential interactions in the LZ detector will be presented in Chapter 5.1.

1.2.6 Hidden Sector

The hidden (or dark) sector refers to a hypothetical collection of yet-unobserved quantum fields and their corresponding hypothetical particles. This sector is termed 'hidden' because its constituents do not interact via electromagnetic, weak, or strong forces, making it challenging to detect them using conventional experimental methods. Particles from this sector can interact with Standard Model particles through gravity and dominant portals: a vector A', a scalar ϕ, a fermion N, and a pseudoscalar a [51]. The interaction terms are described by these following SM gauge singlet operators [51]:

$$\mathcal{L} \supset \begin{cases} -\frac{\epsilon}{2\cos\theta_W} B_{\mu\nu} F'^{\mu\nu}, & \text{vector portal} \\ (\mu\phi + \lambda\phi^2)\, H^\dagger H, & \text{Higgs portal} \\ y_n L H N, & \text{neutrino portal} \\ \frac{a}{f_a} F_{\mu\nu} \widetilde{F}^{\mu\nu}, & \text{axion portal.} \end{cases} \tag{1.5}$$

Here, we have:

- H is the Standard Model Higgs doublet with charge assignment $(1, 2, +\frac{1}{2})$ under $SU(3)_c \times SU(2)_L \times U(1)_Y$.
- L is the lepton doublet for any generation, transforming as $(1, 2, -\frac{1}{2})$.
- $B_{\mu\nu} \equiv \partial_\mu B^\nu - \partial_\nu B^\mu$ is the hypercharge field strength tensor.
- $F_{\mu\nu}$ ($\widetilde{F}^{\mu\nu}$) is the (dual) field strength tensor of the Standard Model photon field.
- θ_W is the weak mixing angle.
- $F'^{\mu\nu} \equiv \partial_\mu A'_\nu - \partial_\nu A'_\mu$ is the field strength tensor of a dark $U(1)_D$ vector boson.

The first three operators are renormalisable (dimension-4), while the axion portal is dimension-5 and suppressed by some high mass scale f_a. These four portals described above [51] are probably the most important ones when discussing dark sectors. At the non-renormalisable level, additional portals can arise from dimension-6 operators which involve a light (or massless) vector mediator and Standard Model fermions [52].

The focus will be on the vector portal as it is the most viable for a thermal model of light dark matter, following the two candidates from the hidden sectors: axion-like particles (ALP) and hidden photons (HPs) in Chapter 5.1. Particles from this sector can contribute to the dark matter density and influence the formation of cosmic structures. Their presence can explain gravitational effects observed in galaxies and clusters, cosmic microwave background measurements, and the large-scale structure of the Universe. These particles are non-relativistic when they decouple, making them suitable for forming structures like galaxies and galaxy clusters, necessitating a form of matter that is abundant, non-luminous, and non-relativistic. Additionally, neutrino masses and baryon asymmetry could involve

additional particles or gauge symmetries in the hidden sector. This category includes axion-like particles [53, 54], dark photons (HPs) [55] and sterile neutrinos [56].

Mirror dark matter

Mirror dark matter (MDM) [57], also discussed in Chapter 5.1, presents a theoretically unique scenario in which the hidden sector is an exact *copy* of the Standard Model sector, making it isomorphic to the Standard Model [57–59]. This means that for each known particle in the SM, there exists a corresponding mirror partner, denoted by a prime ($\prime$). The mirror particles interact among themselves with the same dynamics that govern ordinary-particle interactions. As a result, the full Lagrangian is extended to include the mirror sector term as [57]:

$$\mathcal{L} = \mathcal{L}_{SM}(e, u, d, \gamma, W, Z, \ldots) + \mathcal{L}_{dark}\,(e', u', d', \gamma', W', Z', \ldots) + \mathcal{L}_{mix}, \tag{1.6}$$

where $\mathcal{L}_{SM}$ and $\mathcal{L}_{dark}$ represent the Standard Model and mirror sector Lagrangians, respectively. The mixing term $\mathcal{L}_{mix}$ consists of non-gravitational portal interactions between mirror and SM particles, which is the only place where new parameters are introduced in this model. Since the two sectors are related by a discrete $\mathbb{Z}_2$ symmetry transformation, the allowed vector and scalar portal interactions in this model can be written as:

$$\mathcal{L}_{mix} = \frac{\epsilon}{2} F^{\mu\nu} F'_{\mu\nu} + \lambda H'^2 H^2. \tag{1.7}$$

In this mixing Lagrangian, the first term, $\frac{\epsilon}{2} F^{\mu\nu} F'_{\mu\nu}$, describes the kinetic mixing interaction with coupling constant ϵ. This term represents the mixing of the kinetic terms for $U(1)_Y$ and $U(1)_Y\prime$. The second term is a Higgs–mirror Higgs fields quartic coupling, which forms part of the full Higgs potential. The neutrino portal term is not included by default, as it requires non-degenerate masses for the mirror neutrino and SM neutrino.

In the MDM model, all inferred non-baryonic dark matter consists of various types of mirror matter, including mirror particles and atoms. It is also assumed

that MDM exists as a multi-component plasma halo [60], primarily consisting of e' and He'. More details will be provided in Chapter 5.1 on the model and its expected interactions on Earth, particularly in the LZ detector.

1.3 The search for dark matter

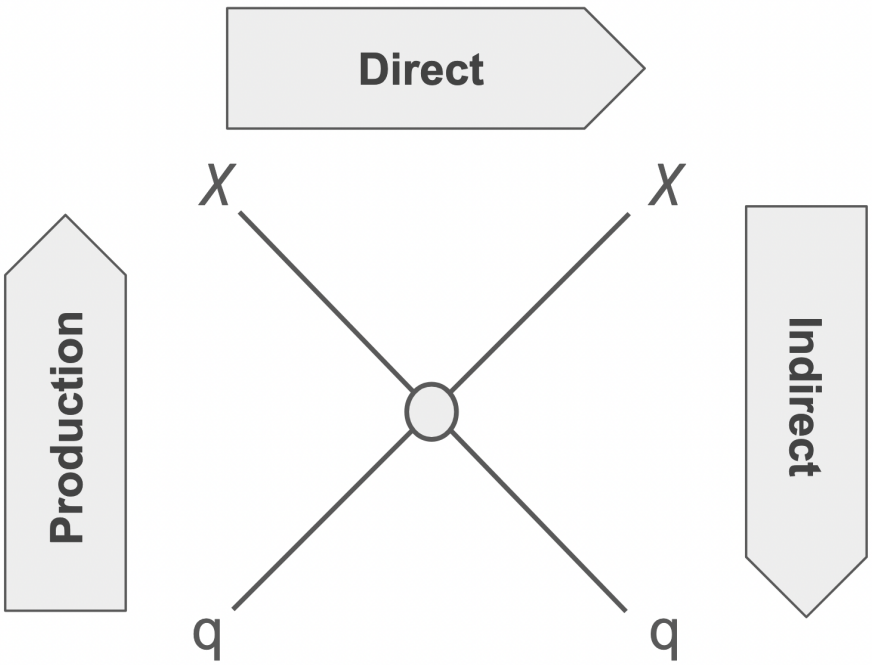

Figure 1.5 *A diagram illustrating the interactions between dark matter and Standard Model particles and their corresponding search strategies. In this diagram, dark matter particles are represented by χ and Standard Model particles are represented by q.*

Fundamentally, dark matter candidates can be divided into two classes: particle-like and wave-like. Focusing on experiments that search for particle-like dark matter, there are three main strategies: "make it, break it or shake it" employed by experiments as shown in Figure 1.5.

- **Production in colliders** - producing dark matter by colliding high-energy particles together.
- **Indirect detection** - observing secondary radiation from pair annihilation of dark matter through astrophysical observations.

- **Direct detection** - detecting dark matter scattering with atomic nuclei in ultra-low background environments.

The first section will delve into the pieces of evidence from the past century that support the existence of dark matter. The section after will provide a brief overview of some popular dark matter candidates and the last section will summary different detection techniques.

1.3.1 Production in colliders

In collider experiments, particles are produced when a target beam is accelerated to nearly the speed of light and then collided at high energies. Usually, the 'invisible' particles produced from these high-energy collisions are neutrinos, but there is potential for the pair production of dark matter. Dark matter particles would not interact directly with the detector, but their presence can be inferred by so-called missing transverse momentum.

For detectors at the LHC [61], researchers add up the momenta of the particles that the detectors can detect, specifically the momenta at right angles to the colliding proton beams, to identify any missing momentum. Before the protons collide, they travel in the direction of the beams, so the overall momentum should be zero. However, if the overall momentum after the collision is not zero, it may have been carried away by an undetected dark matter particle.

A common approach is to look for events with jets, photons, or massive bosons recoiling against missing transverse momentum, known as mono-X signatures. ATLAS [62] and CMS [63] search for reactions such as pp $\rightarrow \chi\overline{\chi}$ + jets. Another approach involves searching for scenarios where the Higgs boson [64] created in LHC collisions decays into a pair of dark matter particles H $\rightarrow \chi\overline{\chi}$.

A main challenge in these searches is identifying potential dark matter events against the vast background of known processes. This requires extensive data collection, as these events are rare, and sophisticated data analysis techniques. Processes such as pp($p\overline{p}$) $\rightarrow v\overline{v}$ + jets or pp($p\overline{p}$) $\rightarrow \ell^{-}\overline{v}(\ell^{+}v)$ + jets also induce a missing energy deposit, mimicking a dark matter signal.

So far, collider searches have not conclusively detected dark matter, but they have scanned over the parameter space of various models and set stringent limits on them.

1.3.2 Indirect detection

By observing the byproduct particles and radiation created when dark matter particles self-annihilate, decay, or interact with regular matter, one can indirectly detect dark matter. Gamma rays, neutrinos, electrons, positrons, and other particles can be produced when dark matter particles annihilate or disintegrate into Standard Model particles. Experiments using indirect detection search for these signals in various astrophysical settings. Due to their predicted high dark matter concentration, some astrophysical objects and areas, including the Sun's core, the galactic center, and spheroidal dwarf galaxies [65], are suitable for indirect dark matter searches. Conventional tools, such as gamma-ray telescopes and neutrino detectors, are used to find the remnants of dark matter decay or annihilation.

Experiments like the Fermi Gamma-ray Space Telescope [66] employ gamma-ray measurements to detect the direct annihilation of dark matter particles into photons ($\chi\chi \rightarrow \gamma\gamma$). The predicted gamma-ray spectrum would exhibit a monoenergetic line proportional to the dark matter mass. This would be a strong indication of dark matter, as no known physical mechanism can create gamma rays larger than the GeV scale. However, because dark matter coupling to photons is either nonexistent or extremely weak, this process can only occur at the loop level and is greatly suppressed. Moreover, the probability of dark matter particles annihilating or decaying into Standard Model particles is higher. These particles would then release photons and generate a continuous, smooth gamma-ray spectrum.

Another possible indirect detection channel is provided by neutrinos from dark matter annihilation. This process occurs when dark matter particles annihilate into Standard Model particles, which subsequently decay into neutrinos. Neutrino experiments like IceCube [67, 68] and ANTARES [69] are designed to detect these neutrinos and set constraints on the annihilation cross section. These neutrino detectors use large volumes of water or ice and operate on the principle of detecting secondary particles created when neutrinos interact with the detector material. These interactions produce Cherenkov radiation, which is measured using detectors equipped with photomultiplier tubes (PMTs) or photo-sensors. By analysing the direction, energy, and timing of the detected Cherenkov light, scientists can determine the characteristics of the incoming neutrinos. An excess of neutrinos from a specific direction, such as the galactic center, may

indicate dark matter decay or annihilation in that astrophysical region. The primary benefit of monitoring neutrinos is their ability to travel great distances with minimal absorption or scattering, providing a clear signal of dark matter interactions. However, the weak interaction of neutrinos makes them difficult to detect, requiring large and sensitive detectors. Additionally, distinguishing potential dark matter signals from background neutrinos produced by other astronomical sources (such as the Sun or cosmic rays) is challenging.

In summary, indirect searches have enabled the dark matter community to impose specific constraints on dark matter theories and provide evidence for certain candidates. For instance, the discovery of an excess of $1 - 3$ GeV energy gamma rays at the galactic core [70] was initially attributed to dark matter annihilation but was eventually linked to unresolved pulsars [71]. Furthermore, an excess of positrons was reported by PAMELA [72] and AMS-02 [73], plus a higher ratio of antiprotons to protons [74], which were most likely due to large uncertainties in the background model. Despite these few anomalies, numerous challenges remain in accurately modelling the background and astrophysical dark matter distribution, making conclusive detection difficult. Therefore, complementary approaches to dark matter searches will be crucial in demonstrating the detection of any dark matter candidate.

1.3.3 Direct detection

Experiments aimed at directly detecting dark matter interactions with Standard Model particles are conducted in laboratories on Earth. Direct detection typically relies on the interaction of a target medium atom with a dark matter particle, χ, to measure the atom's recoiling energy. A dark matter particle incident on a detector can either scatter off the atomic nucleus or electron of the medium, or be absorbed by the atomic electron, depending on its properties. The relevant theories of scattering and absorption, as well as an overview of the various detection technologies and the current status of the area, will be covered in the upcoming sections.

Interaction formalism

The three interactions between incoming dark matter and the target that would produce a signal are shown in Figure 1.6. The expected interaction rate will

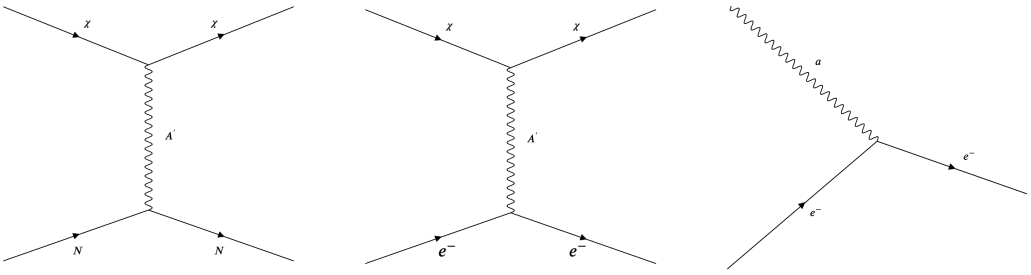

(a) *Dark matter - nucleon scattering* **(b)** *Dark matter - electron scattering* **(c)** *Dark matter - electron absorption*

Figure 1.6 *Feynman diagrams illustrate the types of interaction between dark matter and target medium in a direct dark matter detector that would lead to a signal. Here, χ represents a dark matter particle, N is the interacted medium's nucleon, A' is the propagator and a represents the incoming dark matter that is absorbed by the atomic electron.*

depend on the detector's medium, dark matter properties, and its galactic abundance.

The first step required to formalize any scattering kinematics is to take the Milky Way's local dark matter particle velocity distribution into account. The Milky Way dark matter content is assumed to be distributed as an isothermal sphere with an isotropic Maxwell-Boltzmann velocity distribution for $|\mathbf{v}| < v_{esc}$, given by [75]:

$$f(\mathbf{v}) = Ne^{-(\mathbf{v}+\mathbf{v}_E)^2/\sigma_0^2}. \tag{1.8}$$

Here, $\mathbf{v}$ and $\mathbf{v}_E$ are the dark matter velocity and the Earth's velocity with respect to the dark matter halo, respectively. N is the normalisation factor and σ_0 is the galactic rotational velocity. This equation is truncated at the escape velocity of the Milky Way, $v_{esc} = 544$ km/s [76], the speed above which objects are no longer bound by the gravitational potential of the galactic halo.

Nucleus scattering Focusing on the elastic scattering between a WIMP of mass m_χ and nucleus with mass m_N, the differential rate in the centre of mass frame can be expressed as:

$$\frac{dR}{dE_R} = \frac{M\rho_0}{m_\chi m_N} \int_{v_{min}}^{v_{esc}} v f(\mathbf{v}) \frac{d\sigma}{dE_R} dv, \tag{1.9}$$

where M is the detector target mass, σ is the dark matter cross section, ρ_0 is the local dark matter density and v_{min} is the minimum velocity needed to induce a recoil energy of E_R. The minimum velocity of a WIMP required to induce a nuclear recoil of energy E_R is given by:

$$v_{min} = \sqrt{\frac{E_R m_N}{2\mu^2}}, \tag{1.10}$$

where $\mu = m_\chi m_N/(m_\chi + m_N)$ is the reduced mass of the system.

Electron scattering/ absorption For light dark matter, where $m_\chi << m_N$, the energy transferred [77] in an elastic recoil with the nucleus is:

$$E_R = \frac{q^2}{2m_N} \sim \frac{m_\chi^2 v^2}{2m_N}. \tag{1.11}$$

This means that for sub-Gev scale dark matter, the nuclear recoil energy transfer will be below the detectable energy threshold in some detectors (depending on the medium atom, technology and threshold of the detector). However, the total energy transfer available from the incident dark matter kinetic energy, $\frac{1}{2}m_\chi v^2$, is larger, making it possible for dark matter to scatter atomic electrons and produce signals above energy thresholds. These electron recoil events can occur via ionisation and excitation, which only require $\propto$ eV-scale energy transfer, allowing the detection of dark matter in the MeV/c^2 mass range to be possible for the same incoming dark matter momentum.

An interaction type that is feasible for (pseudo)scalar dark matter candidates, such as axion-like particles or hidden photons, is the absorption of the dark matter particle by the bound electrons in the target. This interaction is analogous to the photoelectric effect, resulting in the emission of an electron from the target atom and producing event in the electron recoil region. The energy deposition by electron absorption would be equal to the mass of the incident particle plus negligible incident kinetic energy, resulting in a mono-energetic peak in the energy spectra.

Detection Technologies

Direct detection experiments aim to measure the energy transfer by dark matter via one or more of the following channels:

- **Ionisation** - Energy transfer in scattering that results in an electron being emitted from the target atom. This is detected by the drifts of electron(s) in semiconductors, noble liquid and low pressure gas detectors.
- **Scintillation** - Emission of a photon occurs when the energy transfer from dark matter to the target atom causes excitation followed by de-excitation. A signal is produced when the photon(s) are measured in scintillators such as noble liquids or crystals, accompanied by photosensors.
- **Heat** - Recoil energy is converted to a collective excitation causing vibrational motion of the lattice. This can be detected using superconductors, superfluids or cryogenic bolometers.

A wide variety of direct detection experiments are available that use one or more energy transfer channels to search for any potential interactions between dark matter and regular matter. A major challenge that all these experiments share is the ability to discriminate between signal and background events, as well as the rarity of these interactions. To address this, most dark matter experiments are built deep underground to shield them from cosmic rays and are constructed using ultra-radiopure materials to limit background noise. Along with background mitigation measures, future experiments are constantly pushing to enhance their detectors' sensitivity by maximizing the detector volume or mass and pushing the detection threshold to the lowest possible energies. The following summarises six types of technologies employed in direct detection of dark matter, also shown in Figure 1.7 along with respective relevant experiments:

- **Inorganic crystal detectors**: When a dark matter particle scatters on the crystal target, energy is transferred to the crystal lattice, causing excitation of the crystal's atoms or electrons. In dark matter experiments using scintillating crystals like NaI (DAMA/LIBRA [79], ANAIS-112 [80], COSINE-100 [81]) or CsI (KIMS [82]), the scintillation lights are measured using photomultiplier tubes, as shown in Figure 1.7 **(a)**. Whereas for semiconductor-based experiments such as silicon (DAMIC-M [83], SENSEI

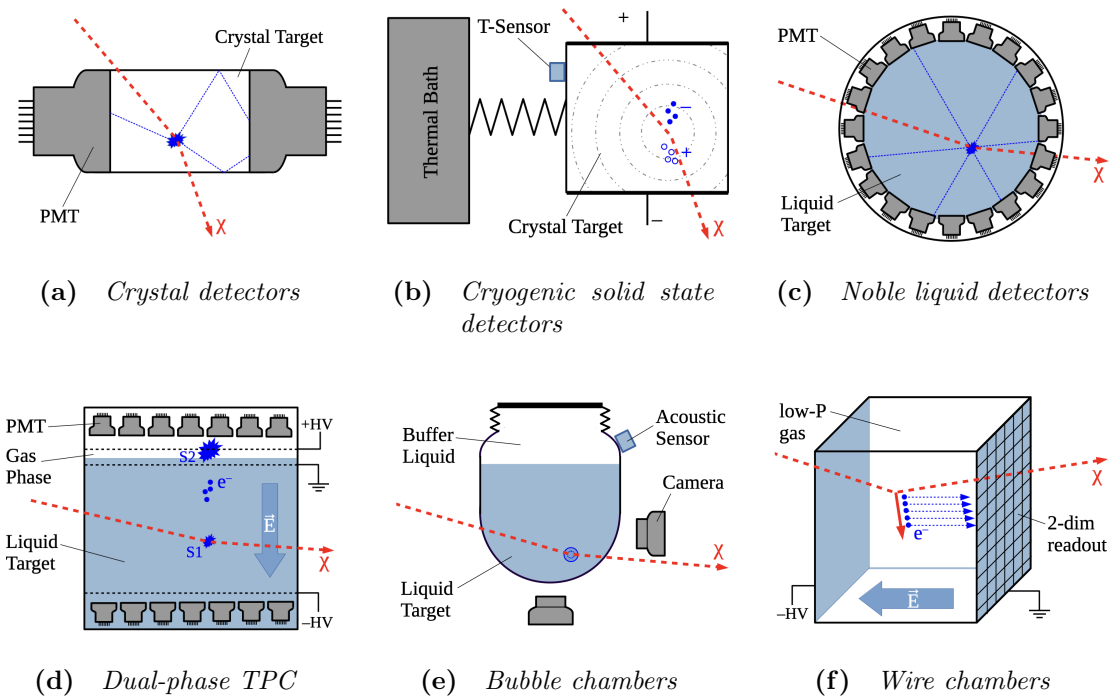

(a) *Crystal detectors* **(b)** *Cryogenic solid state detectors* **(c)** *Noble liquid detectors*

(d) *Dual-phase TPC* **(e)** *Bubble chambers* **(f)** *Wire chambers*

Figure 1.7 *Outline of six types of technologies employed in direct detection of dark matter, taken from reference [78].*

[84]) or high-purity germanium (CDEX-10 [85]), electron-hole pairs are produced and the drifted charges are collected at the electrodes under the effects of the applied electric fields.

The advantages of these detectors are their ability to operate at a very low-energy threshold and their enhanced sensitivity to spin-independent couplings, provided the crystals are composed of elements with a high mass number. On the downside, these detectors are limited to kilogram-scale masses due to increasing levels of electronic noise and signal readout time. Given the crystals' high intrinsic background and inability to discriminate background events, these crystals are more suitable for long-term searches, such as looking for annual modulation, rather than event-by-event dark matter detection.

- **Cryogenic solid-state detectors**: As shown in Figure 1.7 **(b)**, particle interaction with dielectric crystals kept at cryogenic temperatures (mK ranges) generates heat, which is sensed by a change in the resistivity of transition edge sensors (TES). Common crystals employed in direct dark matter searches are high-purity germanium (EDELWEISS [86]) and silicon (SuperCDMS [87], CDMSlite [88]) or $CaWO_4$ (CRESST-II [89]).

At these temperatures, thermal noise is significantly reduced and this allows the detection of very small energy deposition. These detectors also have excellent background veto and energy resolution, allowing them to be sensitive to lower nass dark matter. However, the target mass is limited by the low specific heat capacity requirement and ability to maintain the cryogenic temperatures these devices required to operate.

- **Noble liquid detectors**: A dark matter particle incident in the noble liquid medium generates a scintillation signal as the atom is excited and then de-excited as depicted in Figure 1.7 **(c)**. The prompt scintillation light is then detected by the PMTs covering the target volume. The intensity and timing of the light pulses are recorded, providing information about the energy and location of the interaction. For single-phase noble liquid detectors searching for WIMPs, pulse-shape discrimination (PSD) is utilized to discriminate between signal (nuclear recoil events) and background events (electron recoil events).

  Noble elements, such as liquid argon (DEAP-3600 [90]) and xenon (XMASS [91]), are commonly used in dark matter studies due to their high sensitivity, light yield, and purifiability, which result in a low background. These characteristics make these detectors suitable for detecting rare and weak interactions, although noble liquids are expensive to obtain, and the purification process is challenging to maintain.

- **Dual-phase time projection chamber (TPC)**: Dual-phase TPC is the evolved form of noble liquid detectors where ionised electrons from the interaction are also extracted into the gaseous phase, under the influence of an electric field, to produce secondary scintillation light via electroluminescence [92]. Typically, as shown in Figure 1.7 **(d)**, there are PMT arrays arranged at the top in addition to the PMTs covering the cylindrical chamber to detect the secondary electroluminescence light. This allows event reconstruction using the hit patterns on the PMT arrays and provides a better means of background veto via the analysis of the interaction's position, size, and type. Similar to the above, both argon (DarkSide-50 [93]) and xenon (LUX [94], LUX-ZEPLIN (LZ) [95], XENONnT [96], PandaX-4T [97]) are used in dual-phase detectors. The next chapter will discuss in more depth the technology behind dual-phase TPC, focusing on the LZ experiment.

- **Bubble chambers**: A particle enters the chamber will travel through a

superheated liquid and ionising atoms along its path, depicted in Figure 1.7 **(e)**, leaving a trail of ions behind it. These ions acted as nucleation sites, reducing the local pressure and causing the liquid to undergo a phase change from liquid to vapour to form a trail of bubbles. Cameras or other optical devices capture images of these tracks. The shape and curvature of the track provide information about the charge and momentum of the particle. Experiments use refrigerants such as C_3F_8 (PICO [98]) and C_4F_{10} (PICASSO [99]) as the active target mass.

By adjusting the liquid pressure and temperature, the bubble nucleation energy threshold of these detectors can be tuned, making them suitable for use as threshold detectors. Some advantages of these detectors include the versatility of the liquid medium, high-resolution imaging of particle tracks, and high sensitivity to WIMPs (Weakly Interacting Massive Particles). However, bubble chambers are susceptible to cosmic ray backgrounds, and sophisticated techniques are required to distinguish genuine dark matter interactions from noise-causing events and background radiation.

- **Wire chambers**: When a particle passes through a low-pressure gaseous medium, it ionises gas atoms along its path, creating a trail of ionised gas molecules as shown in Figure 1.7 **(f)**. The charged particles are then drifted under an electric field, where positively charged ions are attracted towards negatively charged wires (cathodes), and free electrons drift towards positively charged wires (anodes). The most commonly used gaseous medium is CF_4, but are often mixed with C_2 (DRIFT [100]) to enhance sensitivity to spin-dependent (SD) and spin-independent (SI) interactions.

  Based on the length of the tracks and ionisation density, the detectors can differentiate between different types of interactions and discriminate signals from backgrounds. The additional directional information from track reconstruction using the ionised tracks provides better background rejection compared to energy deposits in solid and liquid media. Analysis of the events can include the direction of the incident particle and ensure it is consistent with the dark matter wind at that time. This is useful in reducing backgrounds from neutrino scattering events [75].

Above are just some of the technologies employed in direct dark matter searches, but there are more specialised technologies that have not been mentioned.

In recent years, there has been an increase in projects integrating quantum technologies with particle physics to enhance direct detection methodologies. Experiments such as ADMX [101] and CASPEr [102] use quantum-based sensors combined with particle physics infrastructures to search for axions through their interaction with electromagnetic fields. Other interesting approaches have also been presented, such as expanding on current experiments with H_2 doping [103] or crystallisation in dual-phase TPCs, and using superfluid helium [104] as the detector medium.

Chapter 2

The LZ Experiment

The LUX-ZEPLIN (LZ) collaboration is the successor to both the LUX [105] and ZEPLIN-III [106] dark matter experiments, comprising approximately 250 scientists from institutes in the US, UK, Portugal, Switzerland, South Korea, and Australia. The detector is located 4850 feet underground in the Davis Cavern at the Sanford Underground Research Facility (SURF) in South Dakota, USA. LZ features a dual-phase LXe TPC, a well-established technology previously discussed in Section 1.3.3 for the direct detection of dark matter, especially WIMP dark matter with masses greater than a few GeV. This chapter will briefly discuss the physics of xenon detectors/signals produced in the LZ detector, the detector and its subsystems, and how it is designed to optimise sensitivity to the detection of rare dark matter events.

2.1 Xenon microphysics

A particle passing through the LZ detector, which utilises dual-phase xenon TPC technology, can deposit its energy via two types of interactions with the xenon target, as shown in Figure 2.1. These interactions will induce a signal in the detector and are classified into two types:

- **Nuclear Recoils (NRs)** – interactions in which the incident particle scatters off the Xe nucleus in a scattering.
- **Electron Recoils (ERs)** - interactions in which the incident particle

scatters off the Xe electrons or gets absorbed by the Xe electrons.

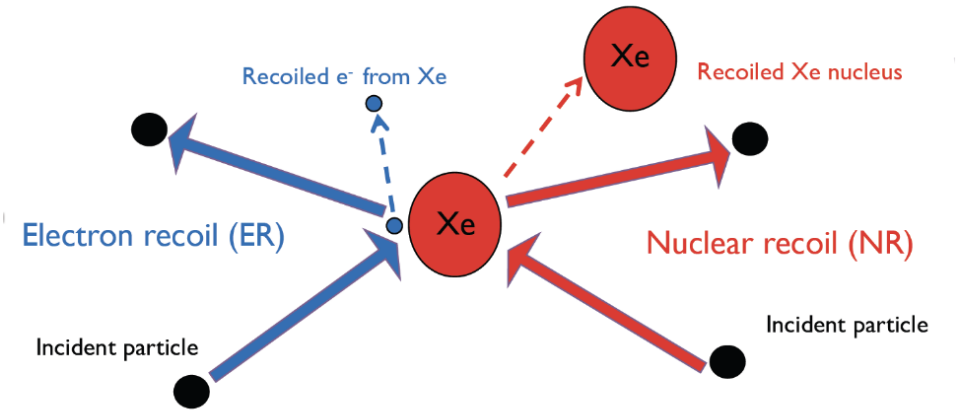

Figure 2.1 *The schematic shows the possible interactions between the incident particle with an Xe atom in the LZ detector: ER (blue) and NR (red). This plot was produced by Harkirat Singh Riyat.*

The types of interaction depend on the properties of the incident particles relative to the properties of the target medium, which is Xe atoms in this case. Given standard WIMPs (weakly interacting massive particles) have very weak coupling with electrons due to them being dark, NRs are considered to be signal-like and primarily ERs are caused by betas and gammas decay from radioactive background. The energy deposited by an incident particle is distributed across three channels: excitation, ionisation and heat. The scintillation light produced by de-excitation is detected as an S1 signal, and the extracted ionised electrons are detected as an S2 signal. The detector is not sensitive to heat so the energy transfer to atomic vibration or below the excitation or ionisation threshold is undetected.

2.1.1 Primary scintillation, S1

Prompt scintillation light is produced by the relaxation of excited diatomic xenon molecules Xe_2^* (excimers), which are produced by two mechanisms [107]. The first, also known as exciton luminescence, occurs as a result of the direct impact of the incoming particle χ:

$$\chi + \mathrm{Xe} \rightarrow \chi + \mathrm{Xe}^* \tag{2.1}$$

$$\mathrm{Xe}^* + \mathrm{Xe} \rightarrow \mathrm{Xe}_2^{*v} \tag{2.2}$$

$$Xe_2^{*v} + Xe \rightarrow Xe_2^* + Xe \tag{2.3}$$

$$Xe_2^* \rightarrow 2Xe + \gamma \tag{2.4}$$

The superscripts (*) indicates electronic excitation and (^{v}) indicates vibrational excitation. Vibrational de-excitation is non-radiative as it occurs via atomic collisions. On the other hand, electronic de-excitation is radiative and involves the emission of a scintillation photon.

The latter, also known as recombination luminescence, occurs via the recombination of electrons with Xe^+ ions:

$$\chi + Xe \rightarrow \chi + Xe^+ + e^- \tag{2.5}$$

$$Xe^+ + 2Xe \rightarrow Xe_2^+ + Xe \tag{2.6}$$

$$Xe_2^+ + e^- \rightarrow Xe^{**} + Xe \tag{2.7}$$

$$Xe^{**} + Xe \rightarrow Xe^* + Xe + \text{heat} \tag{2.8}$$

$$Xe^* + 2Xe \rightarrow Xe_2^* + Xe + \text{heat} \tag{2.9}$$

$$Xe_2^* \rightarrow 2Xe + \gamma \tag{2.10}$$

in which the amount of recombination depends on the applied field and the surrounding ionisation density.

The two mechanisms involve the emission of a vacuum ultraviolet (VUV) photon with a mean wavelength of 175 nm with two possible lifetimes of (3.1 ± 0.7) ns or (24 ± 1) ns is due to respective transitions from the singlet state $^1\Sigma_u^+$ or triplet state $^3\Sigma_u^+$ to the molecular ground state $^1\Sigma_g^+$. The process of recombination is slower than direct excitation as it depends on the thermalisation time of the ionised electrons.

In general, the presence of an electric field reduces the probability of recombination and increases the charge yield, whereas charged particles such as alphas increase the local ionisation density and induce more recombination [108]. Recombination probability is also affected by MeV-scaled interactions. These interactions can introduce additional processes, such as bi-excitonic quenching which can lead to a decreased light yield [109].

2.1.2 Secondary scintillation, S2

Ionised electrons that avoid recombination are drifted upwards to the liquid surface as free charges. At this point, they must overcome a potential barrier to enter the gaseous xenon (GXe) phase, provided by the extraction field. The electrons are then accelerated to sufficient energies to excite the gas atoms, producing secondary scintillation (or electroluminescence) photons and possibly secondary ionisation electrons. The avalanches of secondary electrons result in high amplification gains, with a single extracted electron capable of producing hundreds of photons. The mechanism behind the production of secondary scintillation photons is similar to that of primary scintillation photons: when the excimers (or singly excited atoms) formed by collisions with the electrons de-excite to the ground state. The resulting spectrum is comparable to that of primary scintillation, with only minor differences in peak position and width.

2.1.3 Light and charge yields

Starting with defining the energy deposition E_0 of the incident particle as:

$$E_0 = N_i E_i + N_{ex} E_{ex} + \text{heat}, \tag{2.11}$$

recombination can change the charge and light yields as shown in Figure 2.2, but it does not affect the overall total number of quanta. Thus, this relationship can be described as follows:

$$N_{ex} + N_i = N_\gamma^m + N_e^m, \tag{2.12}$$

where N_{ex}, N_i, N_γ^m, and N_e^m represent the number of excited atoms, electron-ion pairs, measured photons, and measured charge quanta (electrons), respectively.

Despite the effect of the applied electric field, some electrons recombine with xenon ions, and the fraction of recombination changes the measured number of electrons as follows:

$$\text{S2} \propto N_e^m = N_i(1-r), \tag{2.13}$$

$$\text{S1} \propto N_\gamma^m = N_{ex} + rN_i, \tag{2.14}$$

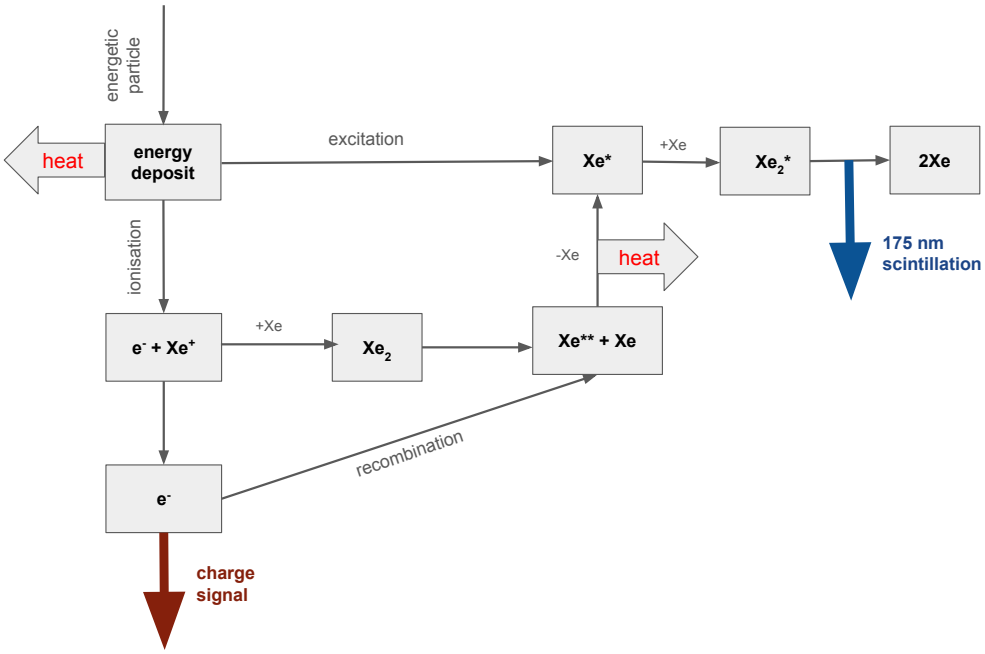

Figure 2.2 *Energy deposition by a particle incident in a liquid xenon target results in the energy being split into three channels: ionisation, excitation, and heat. The LZ detector is only sensitive to ionisation (charge) and excitation (scintillation) signals. Reproduce using materials from a plot made by Eric Dahl.*

where r is the recombination probability. Defining the light and charge yield factors L_y and Q_y as N_γ^m/E_0 and N_e^m/E_0 respectively, the energy deposited can be written as:

$$E_0 = fW(N_\gamma^m + N_e^m), \tag{2.15}$$

where $W = \frac{E_0}{N_{ex}+N_i}$ corresponds to the minimum energy required to generate a single scintillation photon, and f is the inverse of the Lindhard factor L[1] [110]. The commonly adopted value of W is (13.7 ± 0.2) eV [110], but there has been some disagreement in the measured values of W in recent years [111, 112]. Equation 2.15 shows that by taking advantage of the anti-correlation between light and charge quanta to lessen the impact of statistical fluctuations from recombination [113], this can be used to improve the energy resolution.

The light and charge yields of NRs in noble gases, including xenon, differ from those produced by ERs of the same energy. For NRs, interactions result in denser tracks, leading to a higher probability of electron-ion recombination compared to ERs, making electron collection more challenging for NRs. LUX measured the charge Q_y and light L_y yields using mono-energetic 2.45 MeV neutrons (from a

[1] L is taken to be 1 for ERs and a function of recoil energy for NRs.

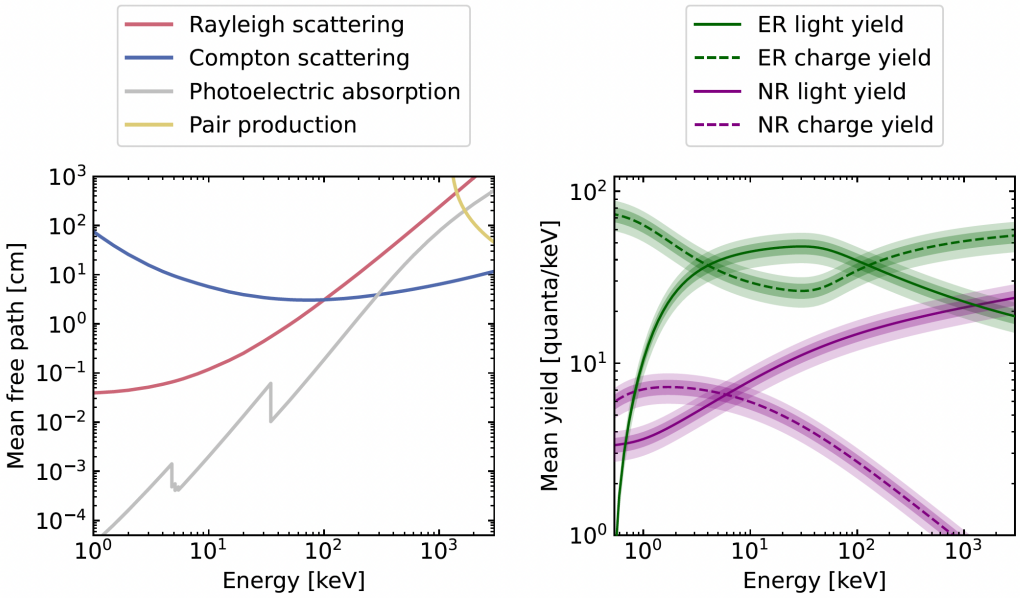

Figure 2.3 *The mean free path of photons travelling through LXe as a function of energy, broken down by different electromagnetic processes, with data referenced from [115] (left); and the light and charge yields of ERs and NRs in LXe at a nominal drift field of 310 V/cm, as modelled semi-empirically by NEST [116, 117] (right). The error bands represent $\pm 1\sigma$ and $\pm 2\sigma$ systematic uncertainties. This plot was produced by Aiham K. Al Musalhi and taken from his thesis [118].*

deuterium-deuterium (D-D) neutron generator) for NR energies spanning 0.7 to 74 keV and 1.1 to 74 keV, respectively [114]. The difference in signals leads to two different energy scales: keV_{ee} and keV_{nr}, depending on the treatment of f applied. Nuclear and electronic recoils have different values of L_y, Q_y, and r, along with other physical processes, which are modelled by NEST, as illustrated in Figure 2.3 (right).

S1 and S2 pulse areas are measured in photons detected (phd), where each PMT's single photoelectron response is calibrated individually. By using corrected S1 (S1c) and corrected S2 (S2c) signals, the signals are adjusted for position-dependent effects to maintain spatial uniformity in the detector response as:

$$\text{S1c} = C_1(x, y, z)\text{S1}, \tag{2.16}$$

$$\text{S2c} = C_2(x, y)(e^{t_d/\tau_e})\text{S2}. \tag{2.17}$$

C_1 is a three-dimensional correction map that normalises the light collection

efficiency to the centre of the detector, whereas C_2 is a two-dimensional correction map that adjusts for radial fluctuations in the extraction field caused by the gate and anode grid deflection. The factor e^{t_d/τ_e} accounts for the loss of drifting charge to impurities in the LXe, where τ_e is the electron lifetime and t_d is the drift time. The corrected signals S1c and S2c can be written in terms of measured quanta as follows:

$$\mathrm{S1c} = g_1 N_\gamma^m, \tag{2.18}$$

$$\mathrm{S2c} = (\epsilon_e N_{EL} g_1^{gas}) N_e^m = g_2 N_e^m, \tag{2.19}$$

where g_1 and g_2 are the photon detection efficiency and effective charge gain, respectively. The parameter g_2 is the product of the electron extraction efficiency ϵ_e, the electroluminescence yield N_{EL}, and the photon detection efficiency in the GXe phase g_1^{gas}. Combining these definitions, the reconstructed energy for ER and NR can be computed as:

$$E_0^{ER} = W \left(\frac{\mathrm{S1c}}{g_1} + \frac{\mathrm{S2c}}{g_2} \right), \tag{2.20}$$

$$E_0^{NR} = \frac{W}{L} \left(\frac{\mathrm{S1c}}{g_1} + \frac{\mathrm{S2c}}{g_2} \right). \tag{2.21}$$

The undetected energy transferred to heat is taken into account in Equation 2.21 by using the nuclear quenching factor L, which is modelled using the Lindhard factor for NRs.

Discrimination of ER versus NR events

The dependency of the excitation-to-ionisation ratio $\mathrm{N}_{ex}/\mathrm{N}_i$, as shown in Figure 2.2, allows for the discrimination between NRs and ERs, thereby facilitating efficient background rejection. This ratio is approximately 0.06-0.3 for ERs [119], while it is around $\sim$1 for NRs [120]. The complete mechanism responsible for this effect is not fully understood, though several hypotheses are discussed in [121, 122].

When a particle incident on the bound electrons of an Xe atom (ER event), most of the energy deposited by the particle will be transferred to the Xe atom mostly via ionisation and excitation with a small amount of energy loss as heat. A greater ratio of ionisation indicates a higher number of electrons that can be extracted in the gas phase so there will be a larger S2 to S1 ratio. On the other hand,

when a dark matter particle is incident on the Xe atomic nucleus (NR event), the majority of the energy deposited by the particle will be lost as heat while the remaining energy is split mostly into excitation and then ionisation. Xenon is chosen as a target medium due to its large light and charge yields as displayed in Figure 2.3 [2].

To understand the LZ detector and reproduce the TPC response to ER and NR events, Noble Element Simulation Technique (NEST) [116, 117] models are used to match the calibration data in {S1c, $\log_{10}$S2c} space. In the LUX-ZEPLIN (LZ) experiment, various calibration sources (discussed in more depth in Section 2.4) are utilised to accurately characterise and calibrate the detector's response to different types of interactions. Along with other calibration sources that LZ employed, tritium is used to calibrate the LZ detector response for ERs, and DD neutron sources are used for NR calibration, as shown in Figure 2.4. In {S1c, $\log_{10}$S2c} space, the events will appear in different bands depending on their interactions in the LZ detector with the Xe target and specific to the detector parameters. Most backgrounds are in the ER band, and NRs in xenon would mostly be from WIMPs, although neutrons and other events such as coherent elastic neutrino-nucleus scattering (CEνNS) events or leakage of ER events can produce WIMP-like NR events. Measures are taken to distinguish NR background events, predominantly from neutrons, from WIMP signals using the LZ veto system, which will be discussed in Section 2.2.2.

[2]There are additional reasons for choosing xenon, such as its relatively easy purification, high atomic mass A (the canonical WIMP cross section scales as A^2), the presence of odd-A isotopes, and more.

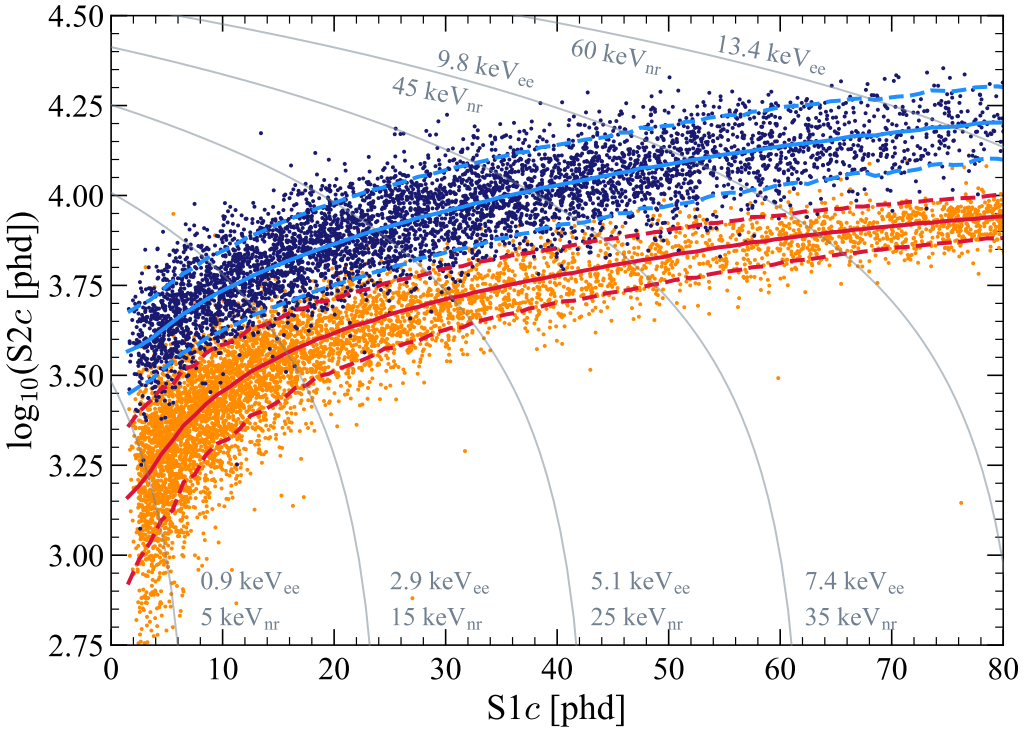

Figure 2.4 *Calibration events in {S1c, $\log_{10}$S2c} space for ER events using tritium source (dark blue points, 5343 events) and NR events using a DD neutron source (orange points, 6324 events) taken from [123]. Solid blue and red lines indicate the median of ER and NR simulated distributions respectively. The dotted lines indicate the* 10% *and* 90% *quantiles. Thin gray lines show contours of constant electron-equivalent energy (*keV_{ee}*) and nuclear recoil energy (*keV_{nr}*).*

2.2 The LZ detector

The focal of the LZ experiment is a dual-phase xenon TPC with its schematic depicted in Figure 2.5. The following will outline the major components of the LZ detector and its subsystems.

2.2.1 The TPC

The xenon detector, as shown in Figure 2.5 (1), consists of the TPC and its LXe skin, which acts as the veto companion to the detector. The TPC is a cylinder containing approximately 7.7 tonnes of active LXe, which constitutes the target for dark matter. The TPC is approximately 1.5 metres in height and diameter, surrounded by two arrays of PMTs embedded on the top and bottom

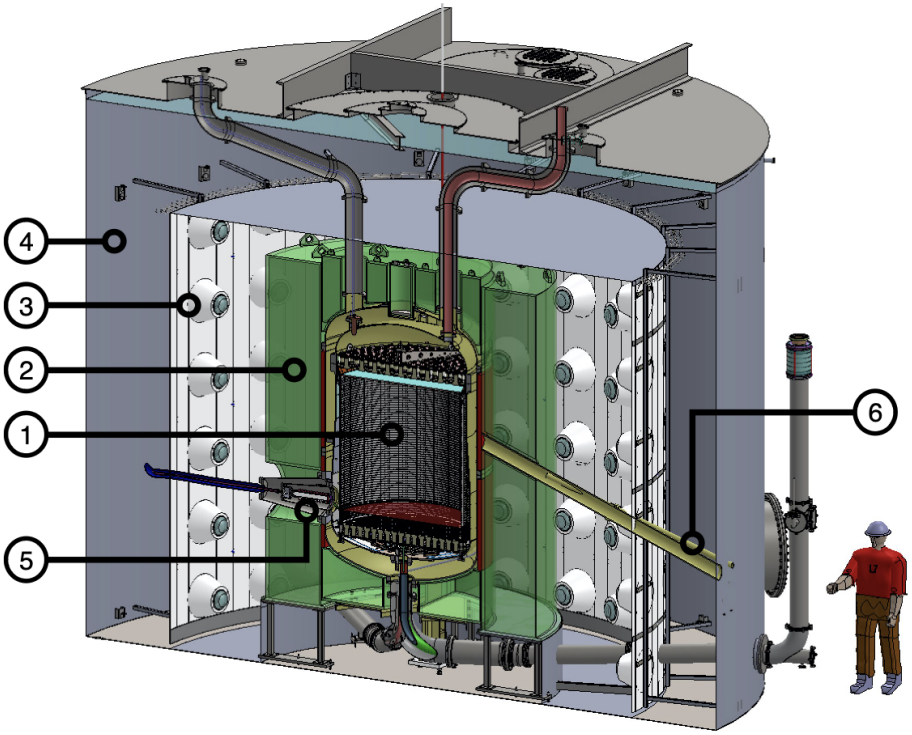

Figure 2.5 *A cross-section view of the LZ detector taken from [95]. The liquid xenon (LXe) TPC (1) is embedded between two arrays of PMTs and serviced by various cable and fluid conduits contained inside a double-walled vacuum insulated titanium cryostat and surrounded by a GdLS acrylic tanks (2). A suite of 8 inches PMTs (3) are placed around the GdLS outer detector (OD) in the ultra-pure water tank (4) to provides additional shielding for the detector. (5) shows the cathode high-voltage connection that is horizontal the ground. The pitched conduit on the right (6) allows for neutrons calibration sources to be fired into the detector.*

of the cylinder. Within the TPC, the Xe is split into the LXe, where prompt S1 scintillation light is produced, and it is topped by an 8 mm thick layer of GXe vapour, where delayed S2 electroluminescence light is produced.

TPC PMTs

The TPC PMTs are 3-inch Hamamatsu R11410-22, developed for operation in cold LXe and detection of VUV luminescence [125]. These particular variants of PMTs were adapted for LZ to be both ultra-low in radioactivity and resilient against spurious light emission observed at low temperatures. The TPC PMTs are arranged in arrays at the top and bottom of the detector as shown in Figure 2.6 [95]. The top array consists of 253 PMTs in gaseous xenon, whereas the bottom array consists of 241 PMTs submerged in LXe. The key parameters of these PMTs—pressure, bias voltage resilience, gain and single photoelectron response quality, afterpulsing, and dark counts—were tested in various radio-assay and performance campaigns over three years. More details about the performance and test campaigns I participated in will be discussed later in this chapter.

Both the S1 and S2 signals generate VUV photons, so it is vital that the detector is optimised to detect VUV photons. For the S1 response, the primary goal is to enhance photon detection efficiency, mainly achieved through the use of high quantum efficiency (QE) PMTs that are better at detecting VUV photons in this wavelength range (approximately 177 nm). Regarding the S2 signal, it is more important to improve the spatial resolution during photon collection, since the electroluminescence process and extraction mechanism increase the gain, making it easier to collect enough photons. The hexagonal packing in the inner array and the transition to a circular pattern around the edge of the top PMTs optimise position reconstruction of small S2 signals near the walls as shown in Figure 2.6. The chamber is also covered with low-radioactive PTFE, which exhibits >97% reflectivity for xenon scintillation light [126], thus maximising light collection efficiency.

TPC Electrostastic field

To ensure that the S2 pulses are efficiently collected with a low probability of spurious responses, the electric field regions in the detector must be carefully designed. The detector is equipped with four electrode grids that create vertical

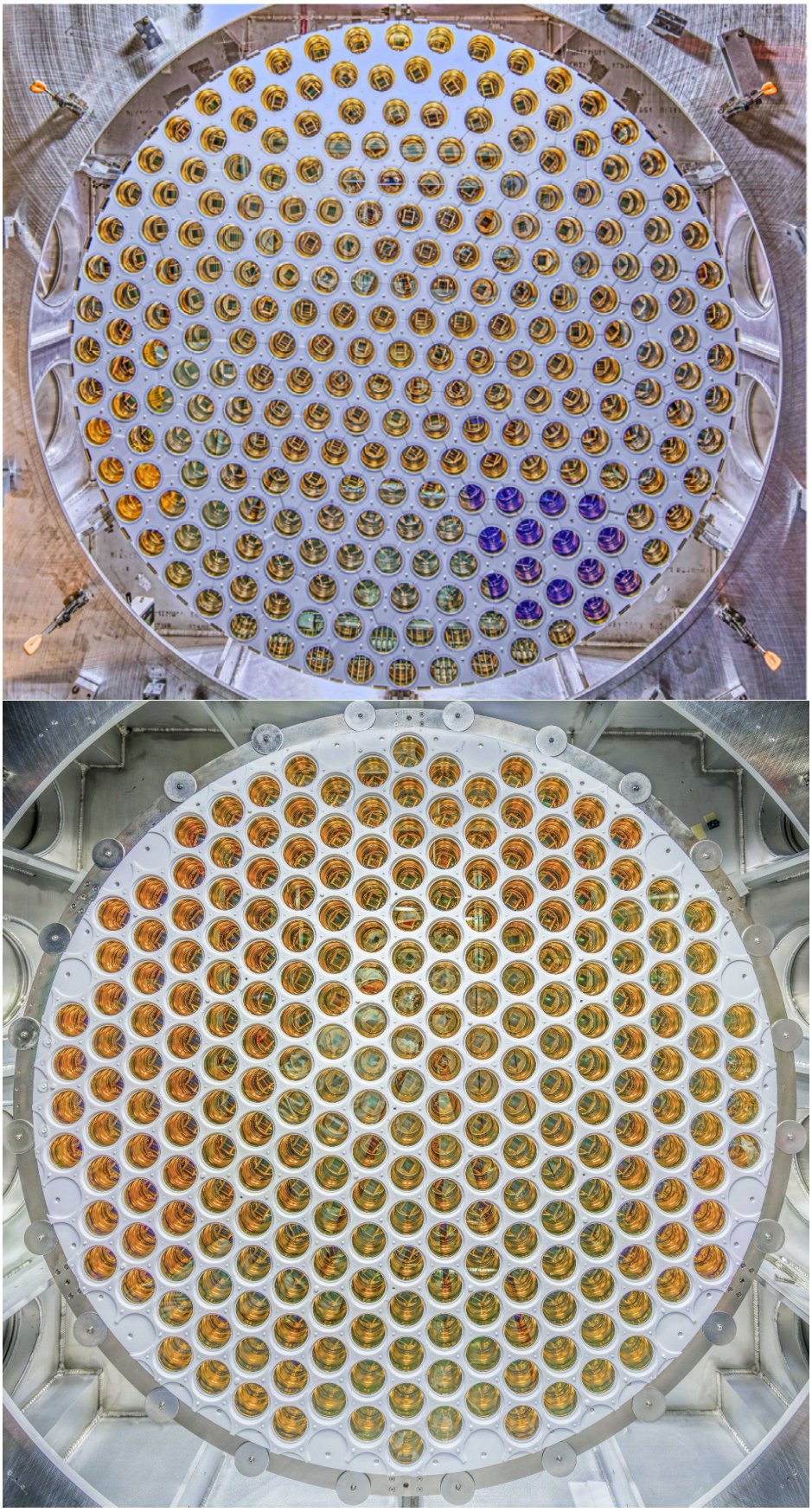

Figure 2.6 *The top and bottom TPC PMTs arrays respectively, taken from [124].*

electric fields within the TPC, dividing it into three field regions as shown in Figure 2.7: the extraction field, drift field, and reverse field regions. Each grid is made from a fine mesh woven from stainless steel wires [127].

The extraction field is generated between the anode and gate grids, which are separated by 1.3 cm and located in the gaseous xenon (GXe) and liquid xenon (LXe) phases, respectively. To achieve optimal performance, the TPC requires electric fields strong enough to remove free electrons from an interaction site, drift them across the LXe (drift field), and finally extract them into the gaseous phase, where they produce electroluminescence signals (extraction field). The extraction field strength is 5 kV/cm in the liquid phase and approximately 10 kV/cm in the xenon gas at 1.8 bar(a) [127]. Beneath the extraction region lies the drift region, or active xenon volume, which is 145.6 cm long and located between the gate and cathode grids, with a nominal field strength of 0.3 kV/cm. Finally, the reverse field region is bounded by the cathode and bottom grids.

The bottom grid is positioned just 1 cm above the bottom PMT array to step down the electric field, as the PMTs, located 14.7 cm below the cathode, cannot function properly in the presence of a high potential due to the risk of false emissions. To prevent electrons from the sub-cathode region from drifting into the gas phase and being extracted, the electric field direction is reversed in the Reverse Field Region (RFR). No S2 signals are produced in this region, which contains approximately 650 kg of xenon.

2.2.2 The Veto System

A crucial goal in the design of the LZ detector is to maximise its ability to detect dark matter interactions in LXe and to distinguish dark matter signals from background events. Most backgrounds are ER events, but there are processes through which natural radioactivity in the detector components produces neutrons, which can result in WIMP-like NR events. The LZ veto system comprises the Skin and the Outer Detector (OD), which together trace the signature of neutron events. The Skin is a 2-tonne LXe region between the TPC outer walls and the inner cryostat vessel, monitored by 93 PMTs at the top and 38 PMTs at the bottom.

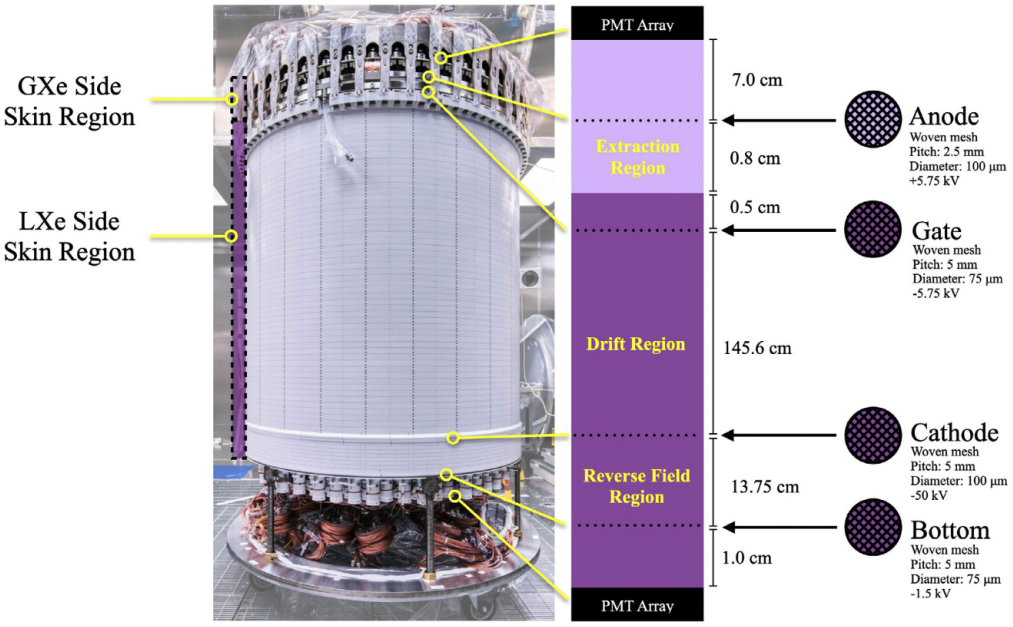

Figure 2.7 *The high voltage electrode configuration for the LZ TPC shown next to a photograph of the assembled TPC. The light purple indicates gaseous xenon and dark purple indicates liquid xenon. The location and sizes of the wires in the diagram is not to scale. The figure is taken from [127].*

The LXe Skin

Around and underneath the TPC, the skin consists of approximately 2 tonnes of LXe with a thickness of 4 cm at the top that gradually widens to 8 cm at the bottom, and it is also instrumented with PMTs. The skin serves as an independent anti-coincidence scintillation detector in addition to being necessary for the dielectric insulation of the TPC. It provides dielectric insulation between the field cage and the inner cryostat vessel, and it functions as a scintillation-only (S1) veto-detector. This is particularly useful for vetoing Compton scattering from MeV gamma-rays and is also complementary to the Outer Detector (OD) as part of the LZ neutron veto system. These particular goals were considered in the design of the TPC and Skin.

The Skin is viewed from above by the 93 1-inch Hamamatsu R8520-406 PMTs that are retained within the PTFE structure attached to the external side of the field cage. At the bottom of the detector, on the dome region of the skin is instrumented with 18 2-inch R8778 PMTs.

Outer Detector

The OD consists of 10 UV-transparent acrylic tanks surrounding the OCV, filled with 17.3 tonnes of gadolinium-doped liquid scintillator to enhance neutron-capture efficiency.

Neutrons undergo single or multiple scatters in the TPC and, once out, they thermalise via collisions with hydrogen in the liquid scintillator or the acrylic tank, producing prompt pulses in the OD. Either the neutron is captured by the hydrogen in the liquid scintillator or acrylic tank, producing single 2.2 MeV gamma-rays, or it is captured by the gadolinium, releasing a cascade of gamma-rays that add up to 7.9 or 8.5 MeV. The timing of these bursts typically falls within the 500 µs window of the S1 signal, ensuring neutron tagging efficiency greater than 95% [128].

Providing a veto efficiency greater than 95% for neutrons scattered in the TPC with less than 5% dead time at the effective threshold of 200 keV is the primary criterion for the OD. Understanding the OD optical model and PMT stability at the 1% level is necessary for this. To verify and track the optical characteristics of the OD and calibrate the OD PMTs to the necessary level, an Optical Calibration System (OCS) has been developed and constructed [129].

2.2.3 Circulation and Cryogenic systems

Detector materials can introduce contamination into the liquid xenon from the outgassing of radon/krypton progeny or electronegative elements such as oxygen and nitrogen. This can affect the efficiency of the TPC in collecting charges and introduce backgrounds. To maintain a high level of purity in the xenon and ensure the temperature of the liquid xenon is controlled, circulation and purification systems are in place, as shown in the schematic in Figure 2.8.

Xenon gas is pumped through a hot zirconium getter at a flow rate of 500 standard litres per minute (SLPM), which takes 2.4 days to purify the entire 10-tonne inventory of xenon in a single pass. To be thermally efficient, the getter, which operates at 400°C, has a heat exchanger to couple the xenon gas streams. The getter bed also serves as a permanent repository for the tritium and ^{14}C radio-labelled methane species that calibrate the beta decay responses of the TPC [130]. The circulation flow is established by the two gas compressors that operate

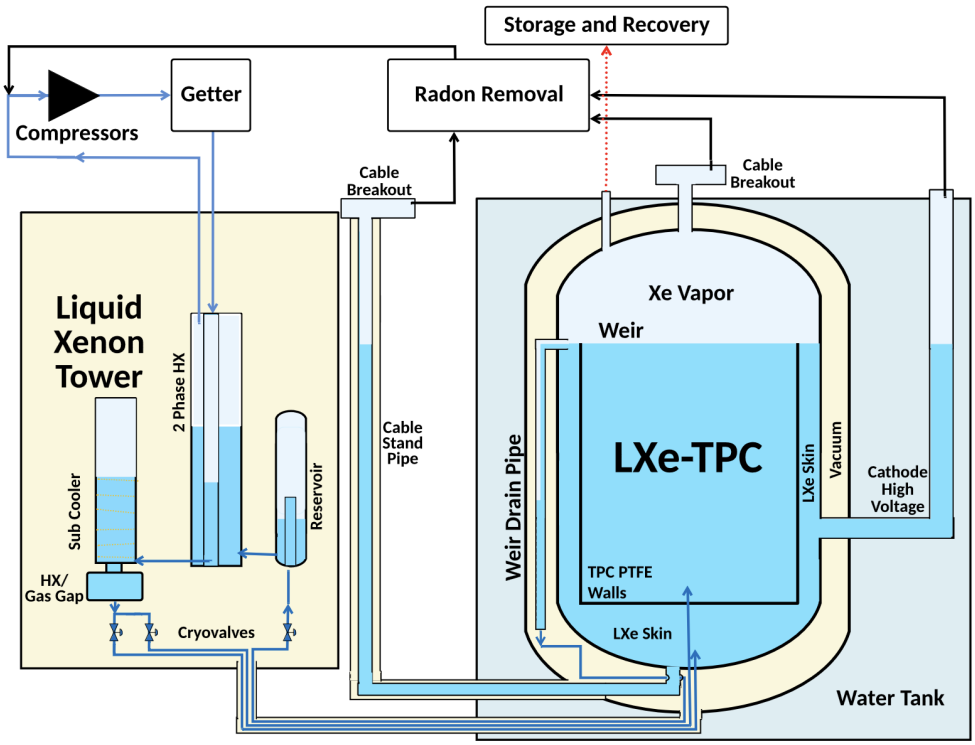

Figure 2.8 *Overview of the online Xe purifying system: After overflowing a weir drain and flowing horizontally to the Liquid Xenon tower, which is located outside the water tank, LXe from the Xenon Detector (right) continues its journey. It is then pumped through a hot zirconium getter after being vaporised in a two-phase heat exchanger and condensed before being recycled back to the detector. The LXe flow between the LXe tower and the Xenon Detector is regulated by cryovalves. Before the compressed gas is sent to the compressor intake, it is treated by a radon removal system in the breakout feed-throughs and cable conduits. This is taken from [95]*

.

in parallel, each able to operate at 300 SLPM at 16 PSIA inlet pressure. During maintenance, the system operates with one compressor at a reduced flow rate.

The LXe tower is a cryogenic device that contains four vessels: the reservoir, the two-phase heat exchanger (HEX), the subcooler vessel, and the subcooler HEX. The reservoir collects LXe after it departs the TPC via the weir system. LXe then flows from the bottom of the reservoir into the two-phase HEX, where it vaporises after exchanging heat with the purified GXe returning from the getter. The condensing LXe from the other side flows into the subcooler vessel and subcooler HEX, where the vessel separates any remaining GXe from the LXe, and the HEX cools the liquid xenon to below its saturation temperature. The He/N_2 gas mixture in the gap is used to vary the power delivered to the LXe from 90 W to 480 W, controlling the condensing of Xe before it is redelivered to the detector via the vacuum-insulated transfer line.

Impurities in the GXe are treated by an in-line radon reduction system (iRRS) as part of the circulation loop. This system uses gas chromatography, a technique where cold synthetic charcoal is used to trap the ^{222}Rn that are continuously emanated from the trace amounts of uranium and thorium in the detector materials [131]. LZ uses Saratech charcoal treated with ultra-pure HNO_3 acid [132], which allows it to reduce the total radon concentration in the LXe detector to meet the ultimate goal in the search for dark matter.

2.3 Reconstruction

The data acquisition (DAQ) system records events using a triggered filter sensitive to S2 signals. Each event is recorded within a time window of 2 ms before and 2.5 ms after each trigger. Non-zeroed waveforms from all the PMT channels for TPC and OD PMTs are recorded for every trigger, with single photoelectron efficiencies averaging 94%, 86%, and greater than 95% for the TPC, skin, and OD PMTs, respectively.

Event properties are reconstructed through analysis of the PMT waveform shapes, timings and distributions. The input raw waveforms (either from DAQ or the full simulation chain) are processed into analysis-ready quantities using LZap, the event reconstruction package. A brief summary describing the reconstruction processes from raw waveforms to quantities used by LZ follows:

1. Normalisation - raw waveform amplitudes are normalised by the PMT and amplifier gains then summed separately within the TPC, skin and OD. The integrated waveform area is recorded in unit of photons detected (phd) at each PMT.

2. Pulse identification, classification and area correction - Algorithm (filters) is tuned to identify pulse boundaries for prototypical pulse shapes in each detector. TPC pulses are classified as S1 or S2 based on their hit patterns and pulse shapes. A requirement for S1 pulses are to have signals above the electronic noise threshold in at least three PMTs.

3. Categorisation - Employing an interaction finder, events are categorised by the event topologies as shown in Table 2.1. The majority of the events are either single scatter (SS) or multiple scatters (MS) based on the number of S2s, representative of the number of scatters.

4. Position reconstruction - Using the Mercury algorithm, the transverse (x, y) position is calculated from the PMT hit patterns of S2 light [133, 134]. The Mercury algorithm was tuned using uniformly distributed radioactive sources in the TPC, which offers a 1σ resolution of 4 mm for S2 signals of 3000 phd. The resolution decreases by half close to the TPC walls due to asymmetric light collecting at the edge. The longitudinal (z) position is inferred from drift time with a resolution of 1σ of 0.7 mm near the cathode.

S1 is normalised to the geometric centre of the detector using dispersed sources (Section 2.4), and this normalised value, known as S1c, is adjusted for drift time, x, and y. Similarly, the S2 signal is normalised into a value known as S2c using a signal located at the top and radial centre of the detector (shortest drift time). The majority of the 9% correction for S1 comes from changes in PMT quantum efficiency and light collection efficiency. The non-uniformity of the extraction field and non-operational PMTs cause the correction size of around 11% in the (x, y) plane for S2, while the typical z correction is roughly 7% due to electron attachment to contaminants. Overall, the corrected parameters across the TPC are within 3% in total.

Table 2.1 *Different types of classified events and their topologies in LZ.*

Name	Requirement	Interactions
Single Scatter (SS)	One S1 followed by a S2	WIMPs, neutrinos, neutrons, low-energy betas or single Compton scattering of gamma rays.
Multiple Scatter (MS)	One S1 followed by multiple S2s	Neutron scattering or multiple Compton scattering of gamma rays.
Pileup Scatter (PU)	Multiple S1-S2 pairs	Coincident or two-level decays such as ^{214}Bi decays.
Other	Other event that doesn't fall into any of the categories above.	Subcathode scatters (S1-only) and S2-only events.

2.4 Calibration

A comprehensive calibration strategy was employed to gain a detailed understanding of the LZ detector. This involved characterising the detector response to both electron recoils (ERs) and nuclear recoils (NRs) within the relevant parameter space, namely the S1c and $\log_{10}$S2c space. The calibration process also included fine-tuning event reconstruction algorithms and optimising detector parameters. Accurate simulations—essential for the statistical analyses involved in searches for new physics—are generated using this calibration data. As previously mentioned, in the context of WIMP searches, NRs may originate from WIMP interactions, while ERs typically constitute background. It is therefore crucial to measure the detector's response to ERs and NRs, as illustrated in Figure 2.4, to understand how events populate the signal space and to enable the calculation of relevant statistics (e.g., medians, quantiles). This information is also used to retrain models for more accurate simulation of detector responses. The calibration sources used by the LZ experiment are listed in Table 2.2, where they are categorised by deployment method, as described in the following sections.

Table 2.2 *The calibration sources used by LZ and their corresponding uses, along with the deployment method, were obtained from [135]. The deployment method is used to classify the sources as follows: A: Gaseous sources injected into GXe circulation. B: Sealed sources are lowered down through the conduits to either the cryostat side vacuum or the cryostat top. C: DD generator fires neutrons into conduits that travel through the water tank and the OD.*

	Source	**Type**	**Energy**	**Half-life**	**Purpose**
A	^{83m}Kr	γ	[32.1, 9.4] keV	1.83 h	TPC (x, y, z)
	^{131m}Xe	γ	163.9 keV	11.8 d	TPC (x, y, z)
	^{220}Rn	α, β, γ	Various	55.6 s	ER band
	^{3}H (tritium)	β	$\leq$18.6 keV	12.3 y	ER band
	^{14}C	β	$\leq$156.4 keV	5730 y	ER band
B	^{88}YBe	(γ, n)	[152, 1836] keV	107 d	Low-energy NRs
	^{88}YMg	γ	1836 keV	107 d	Study ^{88}YBe
	^{241}AmLi	(α, n)	[$\leq$1.5, 5.6] MeV	433 y	NR band
	^{241}AmBe	(α, n)	[$\leq$11, 5.6] MeV	433 y	NR band
	^{252}Cf	n	Watt spectrum	2.65 y	NR efficiency
	^{57}Co	γ	122 keV	272 d	Skin, OD threshold
	^{22}Na	γ	[511, 1275] keV	2.61 y	ER band & inter-detector timing
	^{228}Th	γ	2615 keV	1.91 y	ER band
	^{54}Mn	γ	835 keV	312 d	ER band
	^{241}Am	α	5638 keV	433 y	OD OCS PMTs
C	DD (direct)	n	2450 keV	-	NR yields
	DD (D-reflector)	n	272 $\rightarrow$ 400 keV	-	NR yields
	DD (H-reflector)	n	$\leq$100 keV	-	NR yields

2.4.1 Internal sources

Gaseous internal sources can be incorporated into the TPC by injecting them via the LXe, using a xenon carrier gas as an injectant. In low-energy ER calibrations, where external sources are less effective, this method allows the sources to scatter evenly throughout the TPC, overcoming the self-shielding property of xenon. Calibration for spatially-dependent detector efficiencies, such as light collection and electron extraction, is achieved using monoenergetic metastable sources like ^{131m}Xe and ^{83m}Kr.

Regarding ^{220}Rn, it serves as a suitable source for producing large S1 signals

from the NRs caused by alpha decays, as it does not have any long-lived progeny. This characteristic is beneficial for studies involving the tagging of time-coincident parent and daughter pairs, studying flow mapping in the LXe TPC, and calibrating the LXe skin [136].

Lastly, tritium is introduced in the form of tritiated methane or CH_4-based sealed sources, which generate a beta spectrum with an endpoint energy of 18.6 keV (^{3}H) or 156.4 keV (^{14}C). These sources are used to study detector responses to ERs down to the threshold. To address the challenge posed by their relatively long half-lives, tritium sources must be actively removed from circulation using the zirconium getter, assisted by the CH_4 purifier.

2.4.2 External sources

In general, external neutron or alphas rod sources are deployed using the LZ Calibration Source Deployment (CSD) system. This system lowers external sources through one of three vertical stainless steel tubes with precise positioning along the height of the TPC. Each conduit is capped by a source deployment system, allowing sources to be raised and lowered with a positional accuracy of 5 mm. (α, n) sources such as ^{241}AmLi and ^{241}AmBe are also used to calibrate the NR response of the TPC plus study the neutron tagging efficiency of the OD.

Photoneutron sources (γ, n), such as ^{88}YBe, are used to calibrate the low-energy NR responses for regions from 1 keV$_{nr}$ up to about 4.6 keV$_{nr}$ [137]. Additionally, coherent neutrinos scatters from ^{8}B sources are expected to deposit their energies (<2 keV$_{nr}$) within this energy range. Utilising the (γ, n) reaction of ^{88}YBe, the photoneutron source produces approximately one neutron for every 10^4 γ-rays emitted. To increase the ratio of neutrons to γ-rays entering the TPC, a tungsten shield is used to seal the ^{88}YBe source. During calibration, a crane is used to transport the assembled ^{88}YBe source to the top of the outer cryostat vessel. The source then passes through a cutout in the centre of the top of the OD vessel to the top of the outer cryostat vessel. This positioning ensures that the OD's background neutron tracking capability is preserved while also placing the photoneutron source as close to the TPC as possible during calibration.

2.5 Deuterium-deuterium neutron sources

Deuterium-deuterium (DD) neutron sources, first created and employed in LUX [114], give *in situ* calibrations for NR responses over a range of energies. The DD source produces mono-energetic 2450 keV neutrons at a high rate which are fired into the TPC via two conduits that penetrated through the water tank and OD. Apart from the "direct" mode of operation, there exists a "reflector" mode in which the 2450 keV neutrons are reflected using a target made of either deuterium-based (D-reflector) or hydrogen-based (H-reflector) to decrease the energy of the neutron [105]. This enables the calibration of the lowest nuclear recoil energies with less uncertainty.

2.6 Backgrounds

To differentiate potential signal events from background events, any rare-event search experiment must comprehend and minimise the sources of background. This is heavily influenced by design choices, construction process and the detector material selections. The following sections will highlight the main expected backgrounds in LZ.

2.6.1 Naturally occurring radioactive isotopes

The radioisotopes of ^{60}Co, ^{40}K, ^{238}U, ^{232}Th, and their progeny are generally found naturally within the detector and the surrounding Davis cavern. All these radioisotopes and their progeny can produce both nuclear and electronic recoil events by introducing gamma-rays and beta backgrounds, along with neutrons from (α, n) reactions and spontaneous fission. LZ is particularly concerned about the ^{238}U and ^{232}Th chains because they can generate ER and NR signals within the WIMP region of interest.

Nonetheless, the effects of these sources are well understood thanks to a comprehensive radio-assay and material selection campaign conducted over six years [138]. Various screening techniques have been developed and utilised to study different segments of these radioactive decay chains to determine the complete activities through the ^{238}U and ^{232}Th chains. These techniques include

gamma-ray spectroscopy (HPGe detectors) to assay early and late chain activities; ICP-MS and neutron activation analysis to directly measure the concentration of U and Th in small samples; use of low-background alpha counters such as the XIA detectors (in Chapter 6.2) to measure radon plate-out on material surfaces; and various techniques to screen for radon emanation [139]. The campaign's results and other studies are incorporated into the experimental background model, enabling differentiation of background events from any potential signal excess.

2.6.2 Surface contaminants

The accumulation of dust and the materials' exposure to radon-filled air were major concerns during the construction of the LZ detector. ^{222}Rn progeny can plate-out on surfaces, allowing these radioisotopes to subsequently decay while embedded on the surfaces of the detector materials and diffuse throughout the LXe. Radon daughters, such as ^{214}Po and ^{218}Po, decay by emitting α particles that can lead to the emission of neutrons through (α, n) reactions in detector materials such as PTFE [140]. Although the majority of neutrons will multiple scatter and leave signals in the Outer Detector, a single unvetoed NR by a neutron is indistinguishable from that of a WIMP scatter, making this an important background threat.

An especially problematic background is naked beta decays, predominantly due to the decays of ^{214}Pb or ^{212}Pb daughters in the radon chains. "Naked beta" emission occurs when a beta particle is emitted without any accompanying gamma rays, making it difficult to tag and it can be detected as a single scatter (SS) event. Due to the 99.5% ER/NR discrimination, a small fraction of ERs can appear NR-like, potentially producing a WIMP background where a single scatter ER event is mistaken for an NR WIMP signal-like event. Additionally, trace levels of ^{85}Kr and ^{39}Ar present in the xenon mixtures can also lead to a flat ER background in the WIMP signal region. The concentration of these isotopes was reduced by purifying the xenon inventory using charcoal chromatography [105].

To tackle this issue, LZ has taken measures to construct and assemble the TPC and any component that will be in contact with the active xenon inside a cleanroom to limit the probability of radon progeny plate-out onto the material surface. Additionally, to minimise the accumulation of dust from outside, scientists had to wear full-body cleanroom suits, and deionising fans were used

to prevent the build of charges in the PTFE linings.

2.6.3 Cosmogenic and laboratory backgrounds

The Davis cavern, the home of the LZ experiment, is located 4850 feet (4300 meters of water-equivalent [141]) underground. At this depth, the muon flux is reduced by a factor of 10^6 compared with that at sea level [142, 143]. However, muon-induced showers from the surrounding rock can produce neutrons, though they are moderately attenuated by the water tank covering the detector [95]. There are also gamma-ray backgrounds from the decays of radioisotopes in the cavern walls, but these are well studied and characterised by *in situ* measurements using a sodium iodide detector [144].

During the transportation and storage processes, background sources such as ^{127}Xe and ^{37}Ar were introduced by the cosmogenic activation of xenon through spallation. With a half-life of 35 days, decays of cosmogenic ^{37}Ar introduce noticeable background that peak at 2.7 keV in the early science data. This is problematic as the events will overlap in the ROI for many low-energy ER signals, which will be discussed later in Section 5.1. To account for this background, a detailed model of the expected rate of the activation product concentration was developed [145] and taken into account in the analysis.

2.6.4 Other physics backgrounds

There are various neutrino sources that present background to LZ. The ER background from solar neutrinos is predominantly from *pp* neutrinos, with smaller proportions from the ^{7}Be and CNO chains. Neutrinos can also produce low-energy NRs via the coherent elastic scattering between ^{8}Be or *hep* neutrinos with xenon nuclei, while atmospheric and diffuse supernovae neutrinos can lead to high-energy NRs [146].

Due to LZ's exceptional sensitivity, rare physics processes predicted in the Standard Model, such as the two-neutrino double beta decay ($2\nu\beta\beta$) of ^{136}Xe, can appear as backgrounds. This decay mode ($2\nu\beta\beta$) of ^{136}Xe has been reported by other experiments [147, 148] and declared to have a half-life of 2.17 ± 10^{21} years by EXO-200 [149]. The ($2\nu\beta\beta$) decay can deposit energy up to its 2457.8 keV endpoint.

Another problematic background arises from the two-neutrino double electron capture (2νECEC) of ^{124}Xe, which produces low-energy signatures that can contribute to backgrounds in searches for both low-mass dark matter candidates and WIMPs. The two decay modes, LL and MM — where the letters indicate the atomic shells from which the electrons are captured (L corresponds to the $n = 2$ shell, M to the $n = 3$ shell) — lie within the WIMP region of interest (ROI), with total energies of 10 keV and 5.98 keV, respectively. The XENON1T experiment reported the first observation of this decay mode and measured the half-life to be $(1.1 \pm 0.5_{statistical} \pm 0.1_{systematic}) \times 10^{22}$ years [150]. With a natural abundance of 9.52×10^{-4} [151], the activity of ^{124}Xe in the LZ TPC is estimated to be 8.72 ± 2.44 nBq/kg.

Gamma rays with several interaction sites in the TPC may cause some charges to be lost to the RFT at vertices below the cathode, thereby reducing the amount of S2 collected. These interactions resemble nuclear recoils (NRs).

2.6.5 Accidental coincidence

Additionally, the coupling of uncorrelated S1s and S2s can result in accidental coincidence backgrounds. Isolated S2s can originate from electron emissions from the cathode or gate, from events where S1 is below the detection threshold, or from areas with inadequate light collection. Equivalently sole S2s can occur for interactions towards the top of the detector, where the short drift time means the S1 is included or cannot be separated from the S2s. LZ addresses these backgrounds through fiducialisation and sophisticated data quality cuts.

Chapter 3

Detector stability and data quality

The LZ collaboration invested significant time and effort in regularly monitoring the detector and inspecting the data collection process to ensure stable performance and high-quality data suitable for scientific research. This involved developing online monitoring tools and software to verify data quality, scheduling routine inspections and calibration tasks, and training personnel to efficiently distribute the workload across the collaboration. As soon as the detector was completed and operational, various institutes were assigned daily shifts to verify the detector's stability and if it was collecting data, thereby guaranteeing high-quality data.

The author's involvement with photomultiplier tube (PMT) operations commenced during the initial quality assurance (QA) campaigns, preceding data collection in cold and later gaseous xenon environments. After fulfilling assignments from their home institute and volunteering for additional PMT-related tasks, the author gained substantial experience through various PMT shifts, including LED calibrations. This expertise led to an invitation to join the PMT supervision team as an experienced operator, contributing to the oversight of PMT operations. Following the conclusion of the first science run, which spanned approximately three months, the author participated in the grid testing campaign as the PMT representative.

3.1 PMT calibrations

Periodic LED calibrations are used to check the performance and responses of the PMTs, which is as crucial as calibrating the detector responses using radioactive sources. For the TPC PMTs, the top and bottom PMT arrays are each equipped with twenty-four 470 nm LEDs that can either generate flashes of around 100 photons to measure afterpulses or pulse at low voltage to track single photo-electron gains over time. Afterpulses are spurious pulses that may appear following the output pulse corresponding to the input signal. Typically, afterpulses with long delays are caused by the positive ions produced from the ionisation of residual gases in the detector, in this case, the PMTs, and hence serve as a measure of their vacuum integrity. As for the skin PMTs, the top and bottom of the side LXe skin are equipped with 12 and 18 LEDs, respectively.

A dedicated Optical Calibration System (OCS) has been designed and built to calibrate and monitor the OD PMTs, ensuring the veto system reaches its required efficiency and thus ensuring that LZ meets its target sensitivity. The OCS uses duplex optical fibres to inject photons produced by LEDs into the OD at 35 locations, where 30 of these locations are distributed evenly around the water tank and 5 are below the acrylic vessels [129].

LZ conducted several PMT operations months before the science run began to guarantee that the PMTs passed quality assurance (QA). Many of these procedures required ensuring that, under different relevant Xe conditions, more than 96% of the Xe PMTs sense single photoelectrons (sphe) from LEDs. These quality assurance tests usually comprised biasing PMTs to 1500V, or their nominal voltages, and then measuring and tracking the devices' gain, afterpulsing, and pulse-overlap-discrimination (POD) rates. As for GXe PMT tests, the water tank was empty, and thus there was no protection from background events, and this data was used to compare to the simulated rate.

To assist with the monitoring, there are real-time and delayed monitoring software that are used to check the rates and data collected. DAQScope is used to directly monitor multiple DAQ channels simultaneously as a sum of all the signals from the selected PMT channels, whereas UPM is used as a monitoring tool for specific segments of the acquisition process, such as biasing, gain measurements, and only when the data is being acquired.

3.2 PMT and online monitoring systems

After the LZ detector is fully assembled and ready to search for new physics, a crucial task is ensuring that data is collected accurately, spotting abnormalities in the data collection process, and determining if the data is suitable for analysis. LZ has implemented an infrastructure of online monitoring systems [152] to guarantee the stability and correct operation of the electrical, DAQ, PMT, cryogenic, and circulation systems. Software such as Ignition, Grafana, UPM, and Run Control/DAQ are used to monitor detector conditions and ensure that anomalies such as "hot spots" or "electronic changes" do not affect the data used in scientific research.

This process involves daily checks of the detection systems and assisting with the operations that are scheduled, with tasks allocated to a different institution each week. Prior to starting shifts, each operator must receive training on how to navigate and use the online systems. A supervisor is assigned each week, and their job is to oversee the operators and set up the operation. The shifts are divided into morning and night for US-based institutes and UK-based institutes, respectively, because the monitoring systems are online.

3.3 Shifting duties

Generally speaking, the main responsibilities of an operator are ensuring the system is managed to the extent required to support any onsite or remote operations and to check the stability of the detector. This primarily involves participating in PMT QA tests and calibration efforts before the science runs. The primary responsibilities of the PMT operator during this time are to bias the selection of PMTs and monitor the PMTs and trigger rates in real time while the detector's parameters are being modified to collect data.

Whereas during the science run, an operator's main job is to monitor the stability of the detector while data is being collected, and also to ensure that data collection is optimised and valid for analysis. Occasionally, there are incidents such as one or multiple PMTs tripping, sustained hotspots or high PMT rates, the DAQ or any of the online systems crashing, and the detector being in an unstable condition. An operator's responsibility at times like these is to identify what action should be

taken, which can involve: notifying and contacting the supervisor or appropriate experts, documenting the issues, and marking these in the database to ensure that analysts know whether the data is valid for scientific searches.

3.4 Supervisory role

A supervisor is a more experienced operator who has a comprehensive understanding of the online systems. Thus, the jobs of an supervisor usually comprise of:

1. **Plan:** Conduct a brief discussion with the Operations Manager to align daily tasks, schedule, and potential challenges that are relevant to the day's operations. Compile the information into a clear shift report, provide updates and make adjustments to the plan as necessary. Then, release the document in a shared collaboration drive and notify the allocated operator or people involved.

2. **Monitor:** After allocating the tasks to the operator, regularly check the operation throughout the shift to monitor progress and be available to assist with any issues or challenges that arise. This can involve helping the operator reset the DAQ after it crashes or assisting with biasing the PMTs during times of unstable detector conditions.

3. **Data quality checks:** Data must meet certain requirements for accuracy, dependability, and relevance to the physics search at the end of the shift. The goal of the data collected and whether it is used for WIMP-search, calibration research, or analysing detector performance in various detector parameters is a pertinent inquiry to consider after each operation. To ensure that the data obtained is valid for its intended use, the supervisor must cross-check with the shift reports and note any potential errors that could compromise the authenticity of the data for the analysts.

4. **Training:** Training new operators is one of the main roles of a supervisor. On the job (OTJ) practiced to demonstrate to new operators how to perform shifting duties. Additionally, it is important to provide help for new operators with technical issue they might encounters such as connecting to VPN, access to software or resolve software-related issues.

Along with the jobs listed above, As one of the three PMT supervisors based in Europe, I am often responsible for providing on-the-job training to first-time operators in the European timezone. This has proven to be helpful, as my availability throughout the day allows me to assist with issues new operators encounter.

3.4.1 PMT Anomaly Tracking

A significant part of the responsibilities of PMT supervisors and online systems specialists involve monitoring abnormalities and formally documenting them for future references. Thus, this requires us to classify as what count as anomalous behaviours in the PMTs and usually included, but not limited to:

1. Light emission from detector components observed by the TPC, Skin or OD.
2. Any PMT channel that trip regularly or with increasing frequency.
3. High voltage crate lock up.
4. Events in which large number of PMTs trip simultaneously.
5. PMTs developing a voltage read which is offset from the set voltage by $\pm$ 30V.

The frequency of the so-called anomalous behaviours described above depended on the stage of the experiment. Anomalies 1, 2, 3, and 4 occurred fairly often during periods when the detector was undergoing calibrations and grid testing. These operations typically involved turning on multiple LEDs, varying the strengths of the electrodes, which altered the electric field, and exposing the PMTs to calibration sources. These actions often led to spikes in PMT rates, which could cause multiple PMTs to trip or result in light leakage within the PMTs.

On the other hand, anomaly 5 is a rarer event compare to the other anomalies, and the PMT offset is spotted during a PMT calibration. This is expected, and hence, calibrations are scheduled for at least once every few months, even during the data-taking period, as the PMT's offset is expected to happen over a period of time.

Chapter 4

WIMP search results

This chapter provides a summary of the results from LUX-ZEPLIN's first search for WIMPs, conducted with a fiducial mass of 5.5 tonnes and an exposure of 60 live days.

4.1 WIMP sensitivity

In 2018, LZ released its projected sensitivity for an exposure of 5.6 tonnes fiducial mass and 1000 live days [146]. This projected sensitivity, shown in Figure 4.1, also includes the best WIMP search limit from XENON1T, which was published in 2018. For a WIMP mass of 40 GeV/c^2, the peak sensitivity was expected to be 1.6×10^{-48} cm^2. However, this sensitivity is constrained by several factors. At smaller WIMP masses, the three-fold PMT coincidence cut, required to eliminate dark count coincidences, limits the sensitivity by raising the detection threshold. Conversely, at larger WIMP masses, the sensitivity is constrained by the inverse relationship with the signal rate. As a result, the limits are higher for both smaller and larger masses, with the sensitivity peaking around 30 GeV/c^2, producing the characteristic limit curve shown.

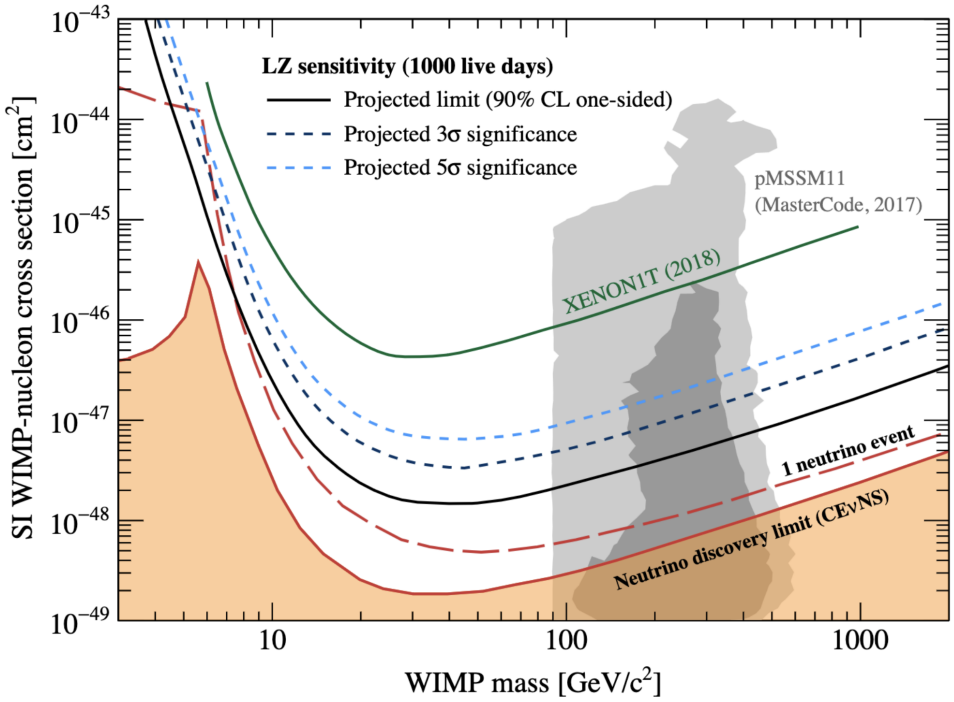

Figure 4.1 *LZ WIMP projected sensitivity for an exposure of 1000 live days using 5.6-tonne fiducial mass taken from [146]. For 40 GeV/c^{2s} WIMPs, the best 3(5)σ significance is obtained at 3.4(6.5) ×10^{-48} cm^2. For comparison, the most recent best limit from XENON1T is displayed. The envelope of 90% C.L. exclusion limits seeing one expected neutrino event is shown as a dotted line. The neutrino discovery limit/ neutrino floor is defined to be the boundary of the neutrino fog, i.e., the cross section at which any experiment sensitive to a given value of WIMP mass leaves the standard Poissonian regime and begins to be saturated by the background.*

4.2 Science Run 1

Science Run 1 (SR1) is LZ's first official run, spanning from 23rd December 2021 to 11th May 2022, totalling 139 calendar days. After excluding the calibration runs, irregular periods, and accounting for 3% lost to DAQ deadtime, the total live days from SR1 consisted of 89.6 days. During the analysis, livetime cuts were applied to exclude periods where the detector was under maintenance, active calibration periods, and times when the data acquistion system was not working or subject to anomalous trigger rates, this will be covered in greater detail in the next section. The final data was reduced to 60 ± 1 live days with the active volume used in the analysis to be 5.5 ± 0.2 tonnes of LXe. This results in a total exposure of 60 live days using a fiducial mass of 5.5 tonnes.

4.2.1 Data Selection

During the 89.6 live days, a total of 1.1×10^8 events were recorded in the SR1 dataset. A series of vetoes and cuts were applied to these events to isolate potential WIMP signals, including fiducialisation and veto cuts to reject multiple scatter (MS) events, S1 and S2 pulse shape-based cuts to filter out accidental backgrounds and misreconstructed events, and exclusion cuts to remove periods of elevated detector activity, mostly induced by large S2s and muons.

Events identified as multiple scatters were removed, as were those with poor reconstruction due to noise, spurious pulses, or other anomalies. For single scatter events to be considered within the WIMP search region of interest (ROI) [123], they were required to have an S1c in the range of 3–80 number of photons detected (phd), an S2 greater than 600 phd, and an S2c less than 10^5 phd. These ROI criteria ensure that signal efficiencies are well understood and that background ER sources are accurately calibrated using tritium data.

A series of accidental coincidence cuts were applied to remove events where isolated S1 and isolated S2 signals were accidentally paired, mimicking single scatter interactions. Isolated S1s can be generated by particle interactions in charge-insensitive regions of the TPC, Cherenkov and fluorescent light in detector materials, or dark-noise pileup. Isolated S2s, on the other hand, can arise from sources such as radioactivity or electron emission from the cathode or gate electrodes, particle interactions in the region above the gate electrode, or drifting

electrons trapped by impurities and released with an $\mathcal{O}$(100 ms) time delay [153]. By conducting comprehensive studies of the expected patterns of S1 and S2 pulses relative to detector parameters such as drift time, pulse width, pulse timing, top-bottom light asymmetry, and PMT hit patterns/timings, these cuts were able to remove more than 99.5% of accidental coincidences.

To mitigate backgrounds associated with γ rays and neutrons, events with a prompt signal in the OD or Skin within ± 0.3 μs (± 0.5 μs) of the TPC S1 pulse are removed. As neutrons can thermalise in detector materials and may be captured on hydrogen or gadolinium in the OD, these events are tagged by OD pulses occurring within 1200 μs after the TPC S1, with energies greater than 200 keV. To tag γ rays returning to the xenon from an OD capture process, a series of large pulses within the same time window is used as an indicator. The neutron tagging efficiency of 89 $\pm$ 3% is determined using AmLi calibration for the NR band.

The efficiency curves for events to pass the S2 trigger, S1 threshold, single scatter (SS) criteria, and data analysis cuts are shown in Figure 4.2. The uncertainty in the total event selection efficiency was estimated using AmLi and tritium calibration data.

Finally, the central fiducial volume (FV) cut was defined by vetoing events less than 4 cm from the detectors walls, with additional cutouts at the top and bottom corners. This cut rejects external and other backgrounds that concentrate near the TPC boundaries along with events with poor reconstruction resolution due to reduced S2 light collection and charge loss near the PTFE wall. By selecting events with drift time 936.5 μs $<$ t $<$ 86 μs, this is also used to filter out events near the gate and cathode grids. The FV and the events that pass the analysis cuts up to this point is shown in Figure 4.3

These processes resulted in a clean sample of 335 single scatter (SS) events that passed all selections, shown as black data points distributed in {S1c, $\log_{10}$S2c} space in Figure 4.4.

4.3 WIMP search backgrounds

As previously introduced in Section 2.6, this section will provide more details on the extensive work that went into generating the nine predicted background

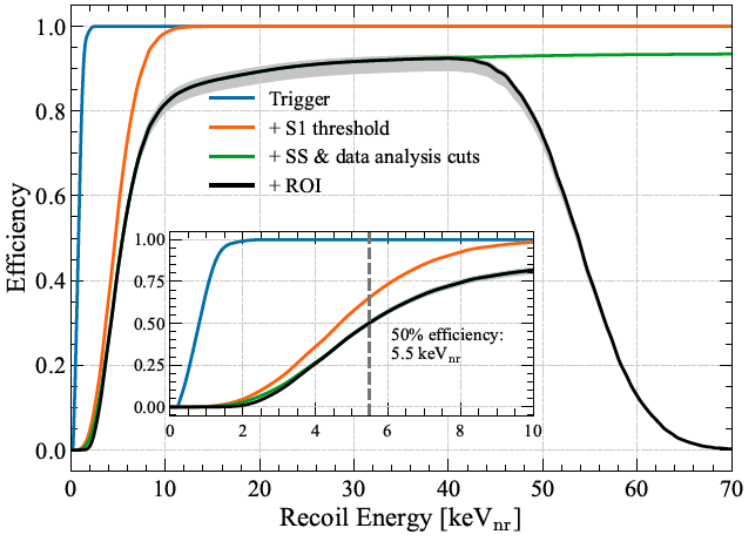

Figure 4.2 *The efficiency for detecting events as a function of nuclear recoil energy is shown. The blue curve represents the efficiency of the S2 trigger in recording events. The application of the three-fold S1 threshold during data processing reduces this efficiency to the orange curve. Data selection cuts, including the identification of single scatter events, result in the green efficiency curve. Finally, the application of the region of interest yields the black curve, with uncertainties for all steps presented in grey. Plot taken from [123].*

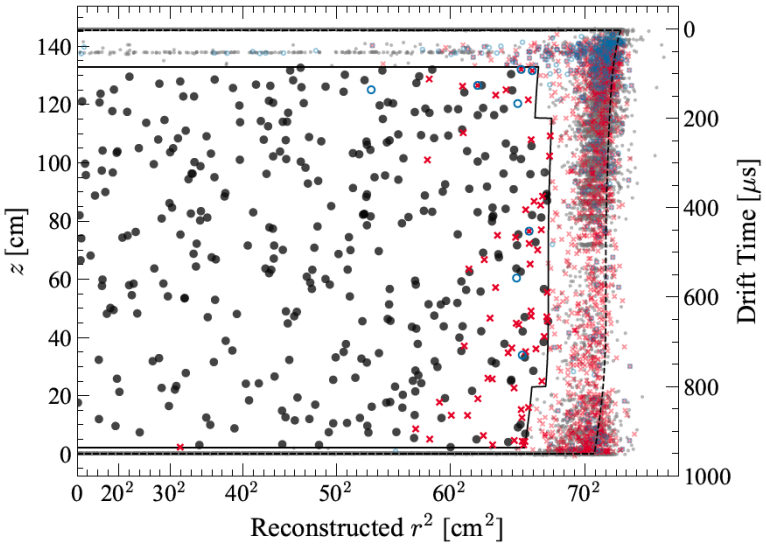

Figure 4.3 *The reconstructed r^2 versus z distribution of events in the final WIMP search data is shown as black points. Grey points represent events outside the fiducial volume, indicated by the solid black line. Red crosses denote events vetoed by the liquid xenon skin detector, while blue squares represent those vetoed by the liquid scintillator outer detector. The physical extent of the detector volume is shown as a dashed black line. Plot created by A. Fan and taken from [123].*

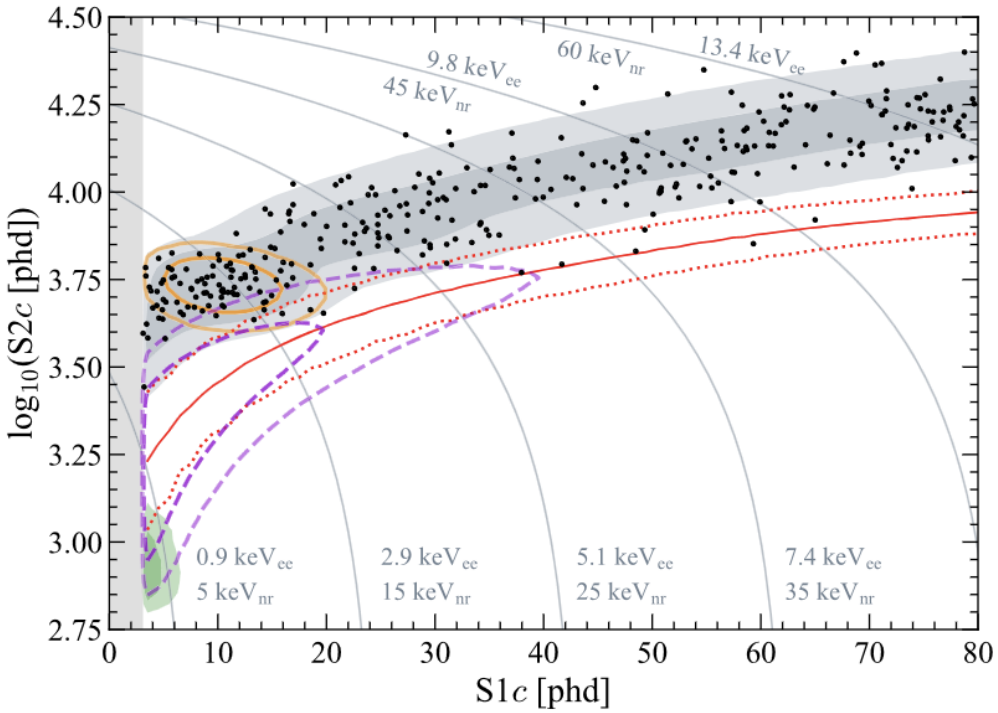

Figure 4.4 *Science run 1 data (black points) after all the cuts applied in {S1c, $\log_{10}$S2c} space taken from [123]. 1σ and 2σ of the following models are enclosed by contours: the ^{37}Ar component (orange ellipses), a 30 GeV/c^2 WIMP (purple dashed lines), ^{8}B solar neutrinos (shaded green regions), and the best-fit background model (shaded grey regions). The 10% and 9% quantiles are shown by the red dotted lines, while the NR median is shown by the red solid line. All of the analysis's efficiencies are included in the model contours. Energy-constant contours are shown by thin grey lines.*

component and their constraints listed in Table 4.1 for the SR1 WIMP search.

Component	Source	Expected Events	Fit Result
1	β decays + Det. ER	215 ± 36	222 ± 16
2	ν ER	27.1 ± 1.6	27.2 ± 1.6
3	^{127}Xe	9.2 ± 0.8	9.3 ± 0.8
4	^{124}Xe	5.0 ± 1.4	5.2 ± 1.4
5	^{136}Xe	15.1 ± 2.4	15.2 ± 2.4
6	^{8}B CEνNS	0.14 ± 0.01	0.14 ± 0.01
7	Accidentals	1.2 ± 0.3	1.2 ± 0.3
	Subtotal	273 ± 36	280 ± 16
8	^{37}Ar	$[0, 288]$	$52.5^{+9.6}_{-8.9}$
9	Detector neutrons	$0.0^{+0.2}$	$0.0^{+0.2}$
Signal	30 GeV/c^2 WIMP	-	$0.0^{+0.6}$
	Total	-	333 ± 17

Table 4.1 *Number of events in the SR1 dataset from different sources [154]. The expected number of events for each background component with uncertainties is determined using data outside of the WIMP-search ROI, and the results of a combined fit of the background model plus a 30 GeV/c^2 WIMP signal to the chosen data are displayed in the right column. The uncertainties are calculated in [154] and employed as constraint terms in this process. Since non-Gaussian constraints were used for ^{37}Ar and detector neutrons, the were excluded from the subtotal. The table is reproduced using data from [123].*

The first component, beta decays of various radioisotopes, including ^{214}Pb from the ^{222}Rn decay chain, ^{212}Pb from the ^{220}Rn decay chain, and naturally occurring ^{85}Kr isotopes dispersed in the xenon, are the primary source of background in SR1. The ^{214}Pb and ^{212}Pb rates were determined by fitting peaks to the energy spectra of the ^{222}Rn and ^{220}Rn decay chains, respectively, outside of the ROI. The concentration of ^{85}Kr was measured at SLAC and SURF using a liquid nitrogen cold trap, with the results confirmed by sampling the LZ xenon and performing *in situ* mass spectroscopy studies. The total β background rate in component 1 includes a flat ER spectrum that represents recoils from γ-rays originating from detector components [138] and cavern walls [144], as these recoil spectra are flat across the ROI.

Solar neutrino fluxes are included as the second component of the estimated background. When solar neutrinos undergo electroweak interactions with the active liquid xenon medium, they induce low-energy ER events. The ER background from solar neutrinos is dominated by *pp* neutrinos, with smaller contributions from the ^{7}Be and CNO chains; therefore, only these are considered.

The solar neutrino rate is calculated using predictions from standard solar models (SSM) [155], as well as measurements from collaborations such as SNO [156] and Borexino [157]. In the region of interest (ROI) for WIMP searches, solar neutrinos produce an approximately flat ER spectrum based on previous studies [158, 159], similar to that from beta decay. However, this contribution is treated separately in the statistical fit due to the precise knowledge of its rate. Additionally, ^{8}B solar neutrinos can induce nuclear recoils (NRs) via coherent elastic neutrino–nucleus scattering (CEνNS), which is incorporated as the sixth component of the total background.

The other NR background arises from radiogenic neutrons (ninth component) originating from detector components and cavern walls. The rate of neutron scatters in the WIMP search data was constrained using a distribution of single scatters in the FV, tagged by the OD, and by applying the measured neutron tagging efficiency of 89%, determined from the AmLi calibration sources. A likelihood fit to the OD-tagged data that passed the other selection cuts is consistent with observing zero neutron single scatter events. This result aligns with the simulation predictions based on detector material radioassay [138].

ER backgrounds in the ROI arise from a variety of decay processes involving distinct xenon isotopes. Naturally occurring xenon isotopes such as ^{124}Xe can undergo a rare process called two-neutrino double electron capture (2νECEC), recently observed by the XENON collaboration [150], while ^{136}Xe can undergo double beta decay (2$\nu\beta\beta$) [149]. The expected rates from these two processes are estimated using the isotopic abundances and lifetimes [151], and are shown as components 4 and 5 in Table 4.1.

Meanwhile, two short-lived isotopes contributing to the third and eighth components in the SR1 background, ^{37}Ar ($T_{1/2}$ = 35 days) and ^{127}Xe ($T_{1/2}$ = 36.5 days), respectively [145, 160], are produced in the LZ xenon prior to its deployment underground by cosmic-ray-induced spallation. Within the WIMP ROI, ^{127}Xe can decay via L- and M-shell electron capture; however, its rates are constrained by K-shell atomic de-excitation outside of the ROI. The skin can reduce this background by effectively identifying the gamma-rays generated during ^{127}I nuclear de-excitation. The duration of xenon's exposure to cosmic rays is used to estimate the number of ^{37}Ar events [145] in SR1.

The last background (seventh component) relevant to the WIMP search ROI comes from accidental events formed by pairing isolated S1 and S2 pulses, as

previously introduced in Section 2.6. To determine the expected distribution of accidental events, single scatter waveforms from isolated S1 and S2 events are generated, and data selection cuts are applied to these events. The selection efficiency is then applied to single scatter events with unphysical drift time, greater than 951 μs, to constrain the rate.

4.4 Statistical test

A commonly used statistical framework in rare event searches is the frequentist hypothesis test, which employs the two-sided profile likelihood ratio (PLR) test statistic to determine the sensitivity or upper limit of a search. LZ uses the PLR test to evaluate WIMP signal in {S1c, $\log_{10}$S2c} space to take advantage of xenon's ER-NR discrimination properties, using probability distribution functions (PDFs) for both signal and background models. These PDFs are generated from simulations, normalised to the expected rates for a given data collection period, and subjected to the same analysis cuts as the data. The number of signal events is then calculated across a range of WIMP masses by scanning over cross-sectional values and performing the PLR tests to obtain upper and median limits at the 90% confidence level (CL).

The background model, as shown in Figure 4.4, were fitted to the data, consisting of 335 events, using a maximum likelihood method. The extended unbinned likelihood function [1] is given by:

$$\begin{aligned}\mathcal{L}\left(\mu, \boldsymbol{\theta}\right) &= \text{Poiss}\left(N_0 \mid \mu_{\text{tot}}\right) \\ &\times \frac{1}{\mu_{\text{tot}}} \prod_{i=1}^{N_0} \left(\mu f_s\left(\text{ S1}c_i, \log_{10}\text{ S2}c_i\right) + \sum_{b=1}^{9} \mu_b f_b\left(\text{ S1}c_i, \log_{10}\text{ S2}c_i\right) \right) \\ &\times \prod_{b=1}^{9} g_b\left(\mu_b \mid \nu_b\right),\end{aligned} \tag{4.1}$$

where μ is the number of signal events, $\boldsymbol{\theta} = \mu_{b=1}$, ..., $\mu_{b=9}$ represents a vector of the expected counts for each of the nine background components, and N_0 is the observed number of events (335 events in this case). The first term in this likelihood is $\text{Poiss}(N_0|\mu_{tot}) = \frac{(\mu_{tot})^{N_0} e^{-\mu_{tot}}}{N_0!}$, where the mean of this Poisson distribution is μ_{tot}, the total number of expected signal and background events

[1] The "extended" part in the likelihood accounts for Poisson fluctuations in the number of events in the dataset or the first term of the likelihood in equation 4.1.

according to the model. The signal and background PDFs in the $\{\mathrm{S1c}, \log_{10}\mathrm{S2c}\}$ signal space are defined as f_s and f_b, respectively. The constraint functions for each background component are $g_b(\mu_b|\nu_b)$, defined according to the constraints ν_b listed in Table 4.1. With the exception of ^{37}Ar and detector neutrons, all the constraint functions are treated as Gaussian and are therefore they were not included in the subtotal in Table 4.1.

Limits on the number of dark matter (signal) events were calculated using the profile likelihood ratio (PLR) method. This statistical approach is fairly widespread in the direct dark matter detection community and there is a set of recommendations for how to construct the analysis in a standardised way [161]. The following will summarise the PLR method but more details are available [162–164] but more details will be included in Section 5.4.

The PLR is defined as:

$$\lambda\left(\mu\right) \equiv \frac{\mathcal{L}\left(\mu, \hat{\hat{\boldsymbol{\theta}}}\right)}{\mathcal{L}\left(\hat{\mu}, \hat{\boldsymbol{\theta}}\right)}, \tag{4.2}$$

where numerator $\mathcal{L}(\mu, \hat{\hat{\boldsymbol{\theta}}})$ is the conditional maximum likelihood for a given value of μ ($\hat{\hat{\boldsymbol{\theta}}}$ maximised the likelihood for a fixed value of μ) and the denominator $\mathcal{L}\left(\mu, \hat{\boldsymbol{\theta}}\right)$ is the maximum value of the likelihood for the dataset. $\lambda(\mu)$ can takes values between 0 to 1 where values close to one indicating good agreement between the data and the hypothesis for a given value of μ.

It is more convenient to use the test statistic (TS):

$$t_\mu \equiv -2\log\lambda(\mu), \tag{4.3}$$

where $0 \leq \mathrm{t}_\mu \leq \infty$. Smaller values indicate good agreement between the data and the hypothesized value of μ. Since dark matter signals cannot be negative, the recommended modification becomes [161]:

$$\tilde{t}_\mu = \begin{cases} -2\log\frac{\mathcal{L}\left(\mu,\hat{\hat{\boldsymbol{\theta}}}\right)}{\mathcal{L}\left(\hat{\mu},\hat{\boldsymbol{\theta}}\right)} & \hat{\mu} \geq 0 \\ -2\log\frac{\mathcal{L}\left(\mu,\hat{\boldsymbol{\theta}}\right)}{\mathcal{L}(0,\hat{\boldsymbol{\theta}}(0))} & \hat{\mu} < 0 \end{cases}. \tag{4.4}$$

Generally, a frequentist hypothesis test is used to compare the model to the observed data by first defining a null hypothesis H_0, which is assumed to be true until proven otherwise, versus an alternative hypothesis H_1. The interpretation

of H_0 and H_1 depend on the context. To evaluate a discovery, H_0 is taken as the background-only scenario ($\mu = 0$) and it is tested against the signal plus background hypothesis H_1. On the other hand, for limit-setting, these are reverse and the H_0 is signal plus background whereas the alternative H_1 is background only ($\mu = 0$).

For the LZ WIMP search, the null hypothesis H_0 is defined to be the combined signal and background model ($\mu \geq 0$) for a given signal count parameter μ whereas H_1 is the background only model ($\mu = 0$). The p-value, used to quantify the level of disagreement between the hypothesis and data, is defined as:

$$p = P\left(\tilde{t}_\mu \geq \tilde{t}_{\mu,\,\mathrm{obs}} \mid \mu\right) = \int_{\tilde{t}_{\mu,\mathrm{obs}}}^{\infty} f\left(\tilde{t}_\mu \mid \mu\right) \mathrm{d}\tilde{t}_\mu, \tag{4.5}$$

where $f(\tilde{t}_\mu|\mu)$ is the distribution of the test statistic for some value of μ specified by the hypothesis, and the p-value is the probability that the test statistic $\tilde{t}_\mu$ for a given value of μ (computed from a dataset produced by the model) is greater than or equal to the one from the observed data. By creating Monte Carlo toys of the datasets under a given hypothesis and fitting the likelihood from Equation 4.1 for each toy, as seen in Figure 4.5, the distributions of the test statistic values are generated.

For a given WIMP mass (signal model), a set of N toys datasets is generated with an amount of signal simulated according to a Poisson distribution with a mean of μ. The toy datasets take on the role of the data in our likelihood terms in the ratio $\lambda(\mu)$ from Equation 4.2, such that the denominator (best fit for each toy) stays the same between the H_0 and the H_1 hypotheses. For the numerator (conditional likelihood), the signal has fixed at the considered value of μ and floats everything else, whereas for the background-only hypothesis, μ is fixed at 0.

For the observed TS, there is only one dataset, so there is only one value. Figure 4.5 is an example which shows some t_μ distributions for a 30 GeV/c^2 WIMP signal. If we have a very large μ, then toy dataset has a lot of signal, setting μ = 0 for the background only hypothesis means that the likelihood will be very small so the ratio will be small, thus the negative log of the ratio will be large, therefore the TS distribution shifts to high values for high μ as shown in Figure 4.5.

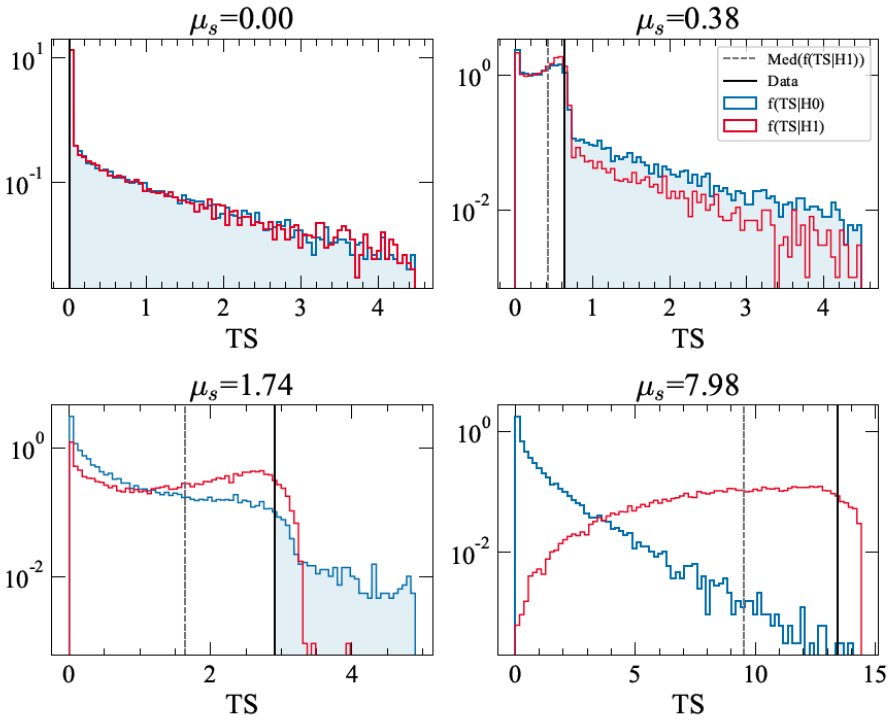

Figure 4.5 *The test statistic distributions for different values of μ_s (number of signal events) = 0.00, 0.38, 1.74, and 7.98, corresponding to a 30 GeV/c^2 WIMP signal model, are shown. The null hypothesis H_0 distribution (blue) represents the combined signal and background model, while the alternative hypothesis H_1 distribution (red) represents the background-only model. The value computed from the data is indicated by the vertical black line, and the median of the H_1 distribution is represented by the dashed grey line. The TS axis labels stand for "test statistic". Figure taken from [165].*

The upper limit on the number of WIMP events in the observed data at the 90% confidence level (CL), is determined by taking a critical p-value $\alpha = 0.1$ for H_0, such that CL $= (1 - \alpha)$. Similarly, this procedure for a background-only dataset can also be computed via the H_1 distribution, where we typically report the median as well as the 1σ and 2σ expected sensitivities. As shown in Figure 4.6, these are obtained for a given WIMP mass by the intersection of each contour with where the p-value $= \alpha$. Once the upper limits at 90% confidence on the number of signal events μ are calculated for a range of WIMP masses, they are converted into physical parameters relevant to the signal model, which is WIMP-nucleon cross-section in this case.

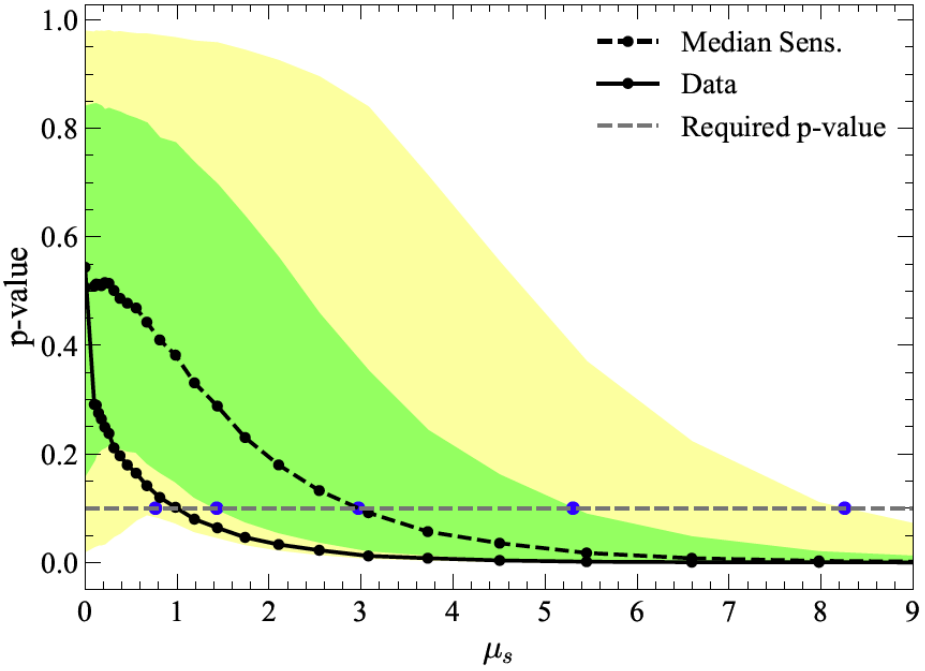

Figure 4.6 *The calculated p-value as a function of the model parameter μ (number of signal events) for a 30 GeV/c^2 WIMP signal model is shown. The black dashed line represents the median p-value from background-only toys, with the green and yellow bands corresponding to the $\pm 1/2\sigma$ p-values from background-only toys. The dashed grey line marks the critical p-value of 0.1, which defines the 90% confidence upper limits. The blue points of intersection indicate the expected sensitivity. Figure taken from [165].*

.

4.5 Results for WIMP Search

A power constraint (PCL) [166] was applied to the 19-26 GeV/c^2 mass range to counteract the under-fluctuation in the background rate [161]. The PCL procedure is used to adjust confidence limits for parameter values with little or no sensitivity, enabling their inclusion. Even after the PCL procedure was applied, LZ was still able to achieve a world-leading limit on spin-independent WIMP nucleon scattering cross section as shown in Figure 4.7.

There is also the possibility that WIMP-nucleon interactions are spin-dependent, and to set limits for this within the direct dark matter community, two cases are considered: WIMP interactions that couple exclusively to neutrons or protons. For LZ, this search depends on the natural abundance of two xenon isotopes with non-zero nuclear spin: ^{129}Xe (26.4%) and ^{131}Xe [151]. Both of these xenon

isotopes have an unpaired neutron, making this search most sensitive to WIMP-neutron scattering. Sensitivity to WIMP-proton interactions arises from the mixing between proton and neutron spin states in isotopes with an unpaired neutron, although this carries higher uncertainty in the predicted rates.

The signal models used in this study are constructed using nuclear structure factors, with uncertainties taken from [167–169]. For each WIMP mass, an uncertainty is calculated by determining the limits corresponding to the minimum and maximum interaction rates at each energy across the models. The data selection, background modelling, and statistical inference procedures are the same as those used in the spin-independent WIMP-nucleon scattering search. The limits for spin-dependent WIMP-nucleon scattering using Science Run 1 data are shown in Figures 4.8 and 4.9.

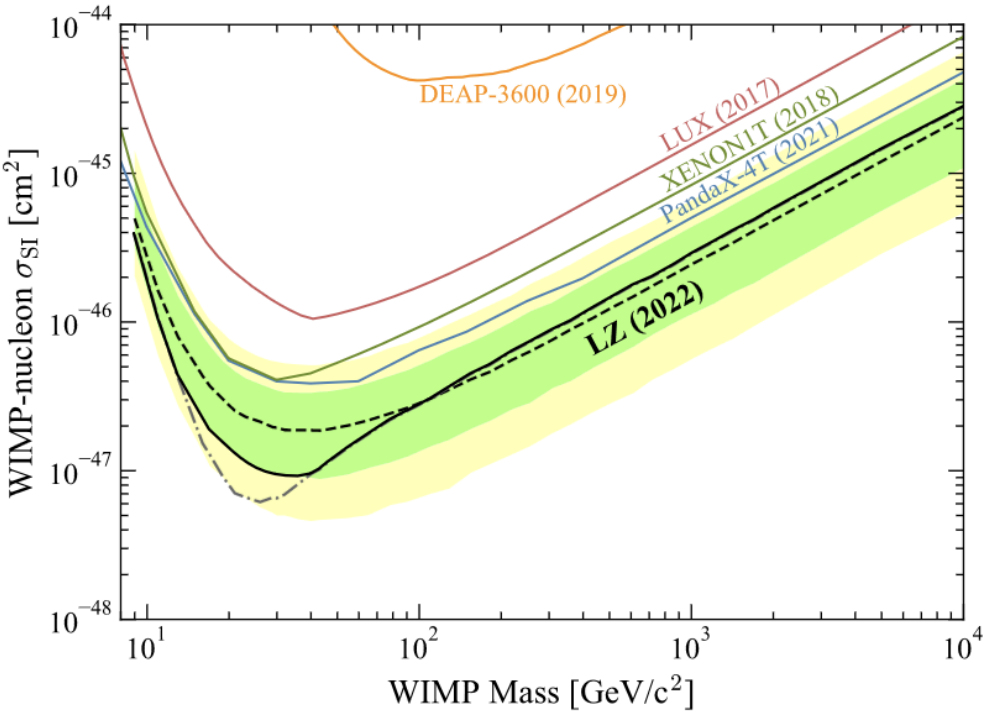

Figure 4.7 *90% confidence limit (solid black line) for the spin-independent WIMP cross section against WIMP mass obtained from [123]. The gray dash line shows the limits before applying the power constraint whereas the green and yellow bands are the 1σ and 2σ bands respectively. Other experiment limits are shown by different coloured solid lines.*

.

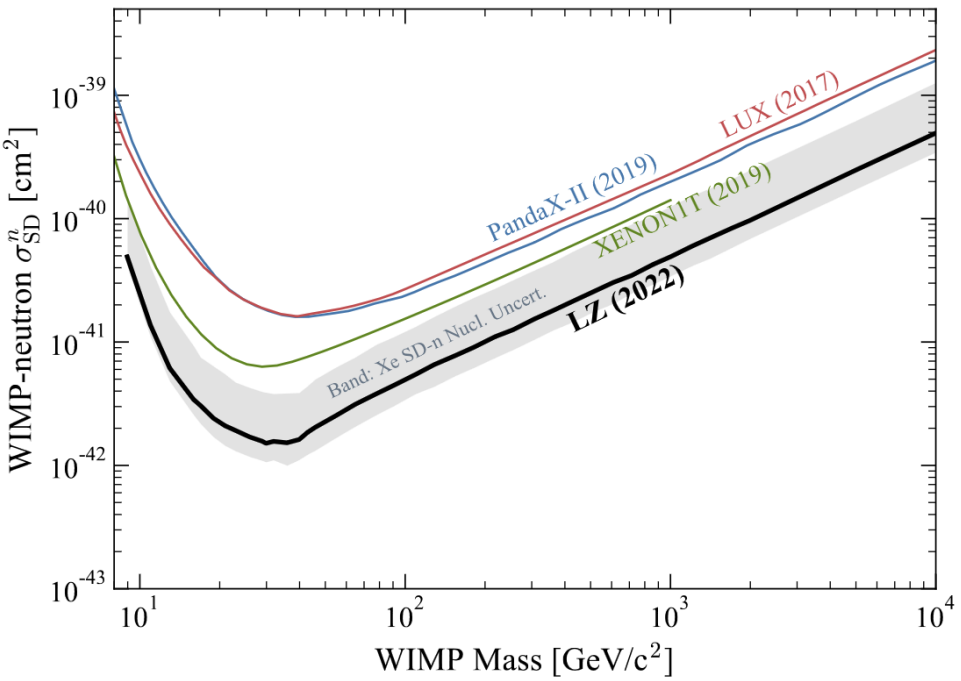

Figure 4.8 *90% confidence limit (solid black line) and uncertainty bands (gray) coming from the xenon nuclear correction factors for the spin-dependent WIMP-neutrons cross section against WIMP mass using the mean of the nuclear structure factors from [168] and range across [167–169]. This plot is obtained from [123].*

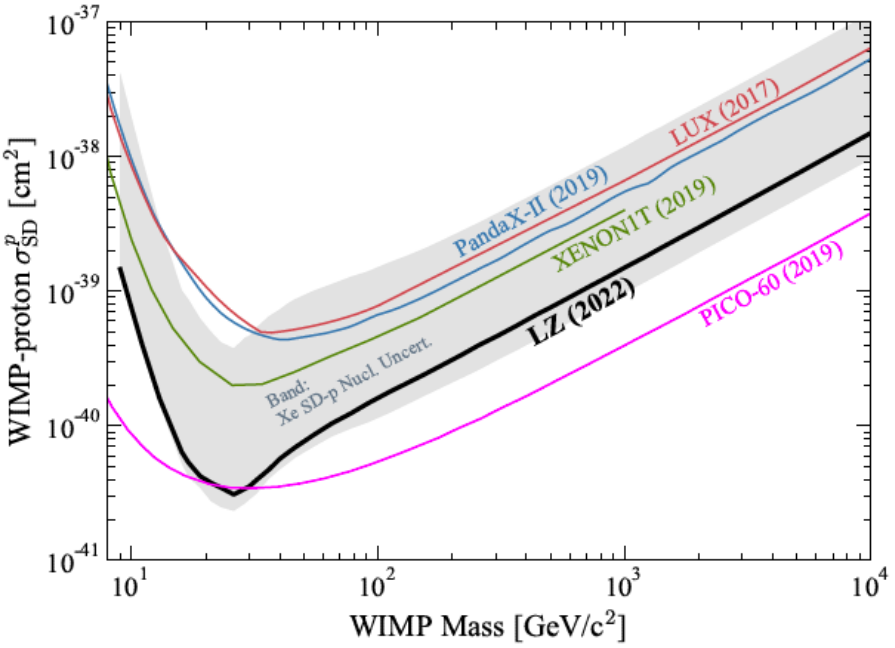

Figure 4.9 *90% confidence limit (solid black line) and uncertainty bands (gray) coming from the xenon nuclear correction factors for the spin-dependent WIMP-proton cross section against WIMP mass using the mean of the nuclear structure factors from [168] and range across [167–169]. This plot is obtained from [123].*

Chapter 5

Search for new physics via the low-energy electron recoil channel

The LZ detector is optimised for rare dark matter searches, especially for WIMPs, because of its ability to discriminate between nuclear recoil and electron recoil interactions, as previously mentioned in Chapter 2. Nevertheless, LZ is also sensitive to a multitude of other unique physics processes that are expected to produce signals in the electron recoil (ER) channel [170]. These searches focus on interactions between incoming particles and the atomic electrons of xenon via electron recoils.

Dark matter incident on a detector can scatter off an atomic nucleus or electron or be absorbed by atomic electrons. Figure 1.6 shows the three types of signal-producing interactions between the incident dark matter and the target. The expected rates will depend on the properties of the detector, as well as the characteristics and astrophysical properties of the dark matter.

For light dark matter, where $m_\chi \ll m_N$, the energy transferred in an elastic recoil with the nucleus is $E_{nr} = q^2/2m_N \sim m_\chi^2 v^2/2m_N$ [171]. Therefore, for sub-GeV dark matter masses, the nuclear recoil (NR) energies will be below the lowest possible detection threshold. Since ER interactions deposit their energies via ionisation and excitation, which only require $\sim$ eV energy transfers, they offer a feasible route for MeV/c^2 dark matter searches.

This analysis focuses on interactions that are expected to produce signals predominantly in the electron recoil bands in LZ signal space {S1c, $\log_{10}$S2c}.

These include certain (pseudo)scalar dark matter candidates [172], such as axion-like particles (ALPs) and hidden photons (HPs) from the galactic halos. Both are expected to be absorbed by Xe atomic electrons. This interaction is analogous to the photoelectric effect, except that the photon energy is replaced by the dark matter particle's rest mass. The spectral signature of this interaction is a mono-energetic peak (a line feature) corresponding to the particle's rest mass. The author works on ALP and HP searches using Science Run 1 data are published in Ref. [1]. The other analysis focuses on the electron recoils originating from mirror dark matter, particularly mirror electrons interacting within the detector. All these searches are also tested against Science Run 1 data.

5.1 Phenomenology of the signal models

All the dark matter models used in this search belong to a class of models called the "hidden sector," which was briefly introduced in Section 1.2.6. The hidden sector, also known as the dark sector, provides a straightforward way to explain the evidence for dark matter without modifying the well-established Standard Model (SM). This section focuses on the relevant theories behind each signal model and the concepts of how these models can be directly detected in liquid xenon detectors, such as LZ.

The hidden sector consists of a hypothetical collection of unobserved quantum fields and their associated dark particles. The primary interaction between particles in the hidden sector and those in the Standard Model is through gravity. However, weak indirect interactions, potentially facilitated by newly proposed particles, are also theoretically possible. This class of models has gained attention in recent years due to the lack of conclusive evidence for WIMP-like dark matter interactions.

For both ALPs and HPs, the physical parameter of interest in LZ is their respective axio-electric coupling, g_{ae}, which will be discussed in the next section. This interaction occurs when incident dark matter particles are absorbed by xenon atomic electrons via the axio-electric effect, analogous to the photoelectric effect. In the case of mirror dark matter, the interaction of interest involves the scattering of mirror electrons off xenon atomic electrons within the detector via kinetic mixing. All of these interactions result in low-energy events that are classified under the ER channels in LZ.

5.1.1 Axion-like particles

As mentioned in Section 1.2.5, ALPs (Axion-Like Particles) are generalised versions of axions that arise in various extensions of the Standard Model, including string theory and other beyond-the-Standard-Model (BSM)[1] physics [173–175], but they are not necessarily tied to the solution of the strong CP problem like axions. One can think of QCD axions as a special case within a broader family of particles that also includes ALPs. This flexibility allows ALPs to span a wide mass range, as they are not constrained by the specific relationship between their mass and coupling that applies to axions.

ALPs have characteristics that make them viable dark matter candidates: they are nearly collisionless, electrically neutral, non-baryonic, and weakly interacting with Standard Model particles. For ALPs to constitute cold dark matter, they would need to be non-thermally produced through the misalignment mechanism in the early universe.

Dark matter ALP production

If ALPs are pseudo Nambu-Goldstone Bosons (pNGBs)[2], i.e if they have a small mass due to non-perturbative effects or explicit symmetry breaking, then this makes them excellent cold dark-matter candidates. Similar to QCD axions, and for ALPs to constitute the population of cold dark matter, ALPs are hypothesised to be produced non-thermally in the early universe via the misalignment mechanism [176]. This allows us to place constraints on the ALP model as a dark matter candidate.

For a pseudo Nambu-Goldstone boson, the spontaneous symmetry breaking could take place before or after inflation. The misalignment mechanism assumes that fields in the early universe have a random initial state that is fixed as the universe expands. The timescale for the evolution of a field of mass m_i is $t \sim \frac{1}{m_i}$. After this timescale, the fields respond by attempting to minimise their potential and thus start oscillating around the minimum.

As the universe expands, if there is no significant damping through decays, then

[1] BSM theories are developed to address the limitations of the Standard Model, but as a concept, BSM is not yet fully understood.

[2] Whereas a Nambu-Goldstone Boson (NGB) is a massless particle that appears when a continuous global symmetry is spontaneously broken in the low-energy theory.

the energy density is diluted by the expansion of the universe as $\rho \propto 1/a^3$, where a is the universe scale factor. Thus, the expected cosmic mass fraction in ALP cold dark matter is given by [50, 176]:

$$\frac{\Omega_{a_i} h^2}{0.112} \approx 1.4 \times \left(\frac{m_i}{\text{eV}}\right)^{1/2} \left(\frac{f_{a_i}}{10^{11}\,\text{GeV}}\right)^2 \left(\frac{\Theta_i}{\pi}\right)^2, \tag{5.1}$$

where Θ_i is the initial misalignment angle, which determines how far the axion field is initially offset from the minimum of its potential and also influences the abundance of axions produced in the early universe, m_i is the mass of the ALP, and f_{a_i} is the ALP decay constant.

Coupling to electrons

Detection of axions via the axio-electric effect specifically measures the coupling of axions to electrons and is independent of the axion-photon coupling. Liquid xenon detectors such as LZ can perform searches for both types of axion particles: dark matter (galactic axions) and solar axions (results are published in the same paper but the work was performed by another author [1]). For dark matter ALPs, which are non-relativistic, the mass of the ALP would be converted into electron recoil energy, producing a monochromatic signal. This process depends on the dimensionless coupling of ALPs to electrons, g_{ae}, which is defined in the Lagrangian density as:

$$\mathcal{L} \supset \frac{1}{2}\partial_\mu a \partial^\mu a - \frac{1}{2} m_a^2 a^2 + \frac{g_{ae}}{2m_e} \partial_\mu a \bar{\psi}_e \gamma^\mu \gamma^5 \psi_e, \tag{5.2}$$

where a represents the ALP of mass m_a, and ψ_e denotes the Dirac field for electrons of mass m_e. For tree-level processes, such as ALP absorption, the derivative interaction term can equivalently be written in the pseudoscalar form $-ig_{ae} a \bar{\psi}_e \gamma^5 \psi_e$, as seen in much of the literature.

There has been speculation about fine-tuning the ALP model because, quantum mechanically, these interactions are nonequivalent and may include an additional coupling to photons [177, 178]. This adjustment allows ALP decays into SM particles at one-loop order, such as $a \to \gamma\gamma$, as shown in Figure 5.1 for ALP decays into di-photons. This is the dominant decay mode for a light ALP.

A viable dark matter candidate must have a lifetime longer than the universe's age. Thus, for $\frac{m_a}{2m_e} < 1$, ALPs cannot decay into electrons due to energy

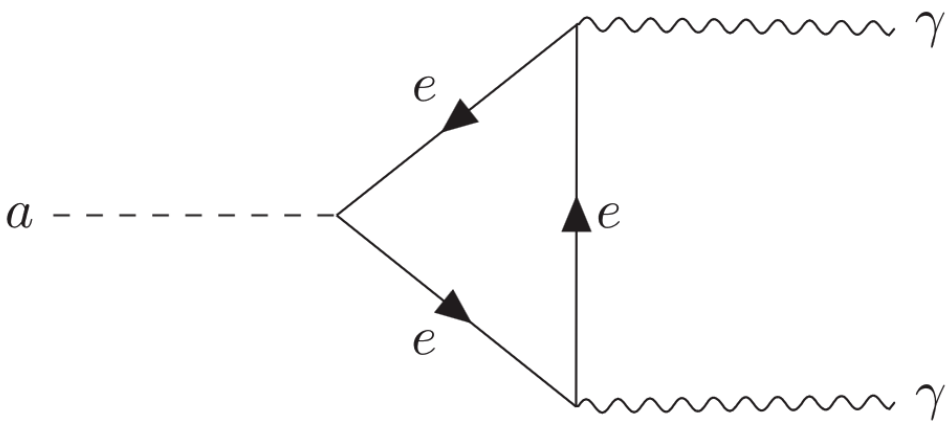

Figure 5.1 *The decay of an ALP, $a \to \gamma\gamma$, through an off-shell electron loop (both loop orientations contribute).*

conservation and remain stable at tree level. However, ALPs described by the Lagrangian in Equation 5.2 decay into two photons through a well-known one-loop process involving a triangle diagram with off-shell electrons, as shown in Figure 5.1. The $a \to \gamma\gamma$ decay rate is given by:

$$\Gamma_{a\to\gamma\gamma} = \frac{m_a^3 \left(g_{a\gamma\gamma}^{1-\text{ loop}}\right)^2}{64\pi}, \tag{5.3}$$

where the ALP-photon coupling for $\frac{m_a}{2m_e} < 1$ is detailed in Ref. [177, 179]. Crucially, for ALP masses in the keV to MeV range, the virtual electrons are not far off-shell, resulting in a potentially large decay rate. In cases where $\frac{m_a}{2m_e} \ll 1$, the resulting lifetime $\tau_{a\to\gamma\gamma}$ is given by:

$$\frac{\tau_{a\to\gamma\gamma}}{13.8\text{ Gyr}} \approx \left(\frac{1.2\times10^{-12}}{g_{ae}}\right)^2 \left(\frac{100\text{ keV}}{m_a}\right)^7. \tag{5.4}$$

The lifetime depends strongly on the ALP mass, and the radiative decay cannot be ignored for heavy ALPs. If g_{ae} is defined through the pseudoscalar coupling, there would be an additional m_a-independent contribution to the ALP-photon coupling [177, 179], further reducing the ALP lifetime. Thus, Equation 5.2 includes a conservative interaction term. This indicates that the hypothesis provided by Equation 5.2 [178] lacks self-consistency for dark matter experiments probing this parameter region.

Using X-ray and γ-ray data from NuStar, XMM-Newton, and INTEGRAL telescopes, severe constraints on the decay $a \to \gamma\gamma$ in the keV - MeV mass

range are obtained in the parameter space region where ALPs are stable enough to be dark matter [180–182]. All experimental investigations for $m_a > 6$ keV test the viable parameter range, which indirect limits exclude. However, for direct detection experiments, these astrophysical constraints do not extend to regions where ALPs are cosmologically short-lived since these assume that ALPs are a component of dark matter.

5.1.2 Hidden photons

Within the sub-GeV mass range for dark matter searches, one of the simplest hypotheses is that dark matter may belong to a "hidden sector" with interactions mediated by a massive gauge boson. First proposed in Ref. [58], the hidden photon (HP), also known as the dark photon, is a hypothetical U(1)′ vector gauge boson suggested as the force mediator for dark matter, analogous to the photon in the Standard Model. This symmetry group kinetically mixes with the SM hypercharge $\mathrm{U}(1)_\gamma$, and the coupling of this gauge boson to electric charge is expected to be suppressed in the range of 10^{-12} to 10^{-2}. Kinetic mixing between the HP, generally denoted as A', and the SM photon provides a "portal" for studying hidden sector particles, along with other candidates such as ALPs, the Higgs, and neutrinos.

In [183], Nelson and Scholtz explored the possibility that the misalignment mechanism could also generate a condensate of light vector particles, produced during inflation, as a viable dark matter candidate. The Lagrangian for the hidden photon [50], A', is given by:

$$\mathcal{L} = -\frac{1}{4} X_{\mu\nu} X^{\mu\nu} + \frac{m_{A'}^2}{2} X_\mu X^\mu + \mathcal{L}_{\text{grav}} + \mathcal{L}_I \tag{5.5}$$

where X_μ is the HP gauge field, $X^{\mu\nu}$ is its field strength, $\mathcal{L}_I$ contains interactions with Standard Model particles, and $\mathcal{L}_{\text{grav}}$ represents potential non-minimal gravitational coupling, with $\mathcal{L}_{\text{grav}} = \frac{\kappa}{12} R X_\mu X^\mu$.

Hidden photon abundance as dark matter candidate

The mass of a hidden photon (HP) could arise from either the Higgs or Stückelberg mechanisms [184–186]. Generally, in the Standard Model of particle physics,

all massive vector particles acquire their mass through the Higgs mechanism. However, if a massive vector ϕ^μ gains its mass from the Higgs mechanism during the inflationary period, the misalignment mechanism will not produce a dark matter condensate.

Given the Higgs Lagrangian:

$$\mathcal{L} = \left[\left(\partial_\mu + ig\phi_\mu\right)\varphi\right]^2 + \lambda\left(\varphi^2 - \frac{m^2}{2\lambda}\right)^2, \tag{5.6}$$

the mass term for ϕ is $M^2\phi^2 - \frac{g^2m^2\phi^2}{2\lambda}$, g is the relevant combination of coupling constants in the loop, λ is the quartic Higgs coefficient and φ is the Higgs field. If symmetry breaking occurs around $T^2 \sim \frac{m^2}{g^2}$, this implies that ϕ is massless above this temperature. To ensure there exists a time when $M \leq H(T)$ while ϕ is not massless, Ref. [183] suggests we satisfy:

$$1 \leq \frac{H}{M} = \frac{T^2}{Mm_{pl}} = \frac{m^2}{Mg^2m_{pl}} = \frac{2\lambda M}{g^4m_{pl}}, \tag{5.7}$$

where H is the Hubble parameter and is a time-dependent damping term.

$$\frac{M}{m_{pl}} \geq \frac{g^4}{2\lambda}. \tag{5.8}$$

Here, Ref. [183] assumes the upper bound of $\phi = m_{pl}$ when $M \sim H$, with this mass corresponding to a wavelength of approximately 10^{11} pc. Consider the Z boson as an illustration: the right-hand side is of the order $\frac{2g^4v^2}{m_h^2} \sim 10^{-3}$. Even for a heavy Higgs with a mass of 500 GeV, this implies that a condensate of W and Z bosons could not be generated via the misalignment mechanism.

If we take the limit where $M^2 = \frac{g^2m^2}{2\lambda}$ is fixed, but $m_h \to \infty$ and $\lambda \to \infty$, the right-hand side of Equation 5.8 becomes arbitrarily small. The vector field can retain its mass at arbitrarily high temperatures by parametrising the Higgs in polar coordinates $\varphi = (\nu + h)e^{i\theta/\nu}$ and integrating out the heavy Higgs field. In this case, the resulting Lagrangian takes the form:

$$\mathcal{L} = -\frac{1}{4}F^2 - \frac{1}{2}\left(MA^\mu + \partial^\mu\theta\right)^2, \tag{5.9}$$

which is equivalent to the Stückelberg Lagrangian [186, 187].

Hidden photon interaction and constraints

While there are various proposals for detecting dark photons in the sub-meV mass range, this discussion focuses on dark photons generated through inflationary perturbations or other non-thermal mechanisms. This is particularly relevant for WIMP-search experiments like LZ, which are sensitive to hidden photons (HPs) with masses in the 10 eV - 100 keV range. The sensitivity of liquid xenon experiments to vector particles has been previously explored in [188].

By definition, Standard Model (SM) particles are not charged under the U(1)′ symmetry, so there is no direct coupling to HPs. However, there are several hypotheses that permit very weak couplings between hidden and visible sectors. The most well-established portal is kinetic mixing, proposed by Okun [189] and Holdom [58]. This mixing appears in vacuum polarization diagrams in field theories and is also assumed in string theories. At energies below the electroweak scale, the effective Lagrangian is given by:

$$\mathcal{L} = -\frac{1}{4}F_{\mu\nu}^2 - \frac{1}{4}\chi_{\mu\nu}^2 - \frac{\epsilon}{2}F_{\mu\nu}\chi^{\mu\nu} + \frac{m_{A'}^2}{2}\chi_\mu\chi^\mu + eJ_{\text{em}}^\mu A_\mu, \tag{5.10}$$

where ϵ is the coupling constant for kinetic mixing between the HP (A') and the photon (A), with their respective field strengths $\chi_{\mu\nu}$ and $F_{\mu\nu}$. For a photon, the field strength tensor is defined as $F_{\mu\nu} = (\partial_\mu A_\nu - \partial_\nu A_\mu)$. Here, J_{em}^μ is the electromagnetic current, and $m_{A'}$ is the HP mass. The direct HP-photon mixing in Equation 5.10 is valid as long as $m_{A'} \ll m_Z$, where Z denotes the Z boson. Otherwise, additional mixing with the hypercharge component of Z would need to be considered.

The coupling ϵ represents the strength of the kinetic mixing and is generally non-zero, with a natural value approximated by:

$$\epsilon \approx \frac{eg_h}{16\pi^2}, \tag{5.11}$$

where e and g_h are the visible and hidden gauge couplings, respectively. Assuming $g_h \sim 1$ in field theories, we get $\epsilon \sim 10^{-3}$ [190]. However, in large volume string compactifications, smaller values of g_h are possible, resulting in ϵ values in the range of 10^{-12} to 10^{-3} [191].

To constrain HPs in a vacuum [192], this theory simplifies to a vector particle of mass $m_{A'}$ with a coupling $e\epsilon$ to all charged particles. Some of this simplicity

disappears when matter effects for the SM photon become significant, causing the effective mixing angle to become suppressed.

Photon-HP oscillation interactions generally form the basis for searches in the low energy (eV and below) window [193–196], whereas HP decays generated in detectors via bremsstrahlung or other mechanisms are the focus of intermediate (sub-GeV) and high (GeV - TeV) searches [197–201]. With sensitivity to mass ranges in keV/c^2 [202], the hidden-photoelectric effect from the absorption of HPs is the HP signature of interest for liquid scintillator detectors such as LZ [1] and others [203, 204]. Since HPs always interact with SM particles via kinetic mixing, different methods probe various regions of the HP parameter space defined by (m_{HP}, ϵ). For ALPs, however, this is not the case, as they couple directly to SM particles. Consequently, distinct experiments probe various ALP couplings, such as the ALP-photon $g_{a\gamma}$ or ALP-electron g_{ae} couplings.

5.1.3 Mirror dark matter

First introduced in Section 1.2.6, mirror dark matter is a specific case of a hidden sector model in which the hidden sector is isomorphic to the Standard Model (SM) [57]. This symmetry implies that the hidden sector contains a mirror counterpart for each SM particle, and each mirror particle shares the same mass, lifetime, and self-interaction properties as its corresponding SM version. Returning to the Lagrangian that describes possible non-gravitational interactions between ordinary and mirror particles, $\mathcal{L}_{mix}$, introduced in Chapter 1, we have:

$$\mathcal{L}_{\text{mix}} = \frac{\epsilon}{2} F^{\mu\nu} F'_{\mu\nu} + \lambda H'^2 H^2. \tag{5.12}$$

The two terms in the Lagrangian above (Eq.5.12) involve two dimensionless parameters: ϵ (kinetic mixing) and λ (Higgs coupling), both of which are not determined by the symmetries of the theory. Only the first term, the kinetic mixing term with ϵ, allows very weak electromagnetic interactions between mirror and SM particles, making it more relevant in the direct detection search for mirror dark matter. The Higgs-mirror Higgs portal can be probed at colliders through Higgs production and decays but does not produce observable signals in direct detection experiments.

Photon - mirror photon kinetic mixing

Since $F_{\mu\nu}(F'_{\mu\nu})$ is the ordinary (mirror) $\mathrm{U}(1)_\gamma$ gauge boson field strength tensor, the $\mathrm{U}(1)_\gamma - U(1)'_\gamma$ kinetic mixing term from equation 5.12 The physical effect of the kinetic mixing interaction is to induce a tiny ordinary electric charge for the mirror proton and mirror electron of $\pm\epsilon e$ [57], thus leading to electromagnetic interactions of the form: $\bar{e}e \to \bar{e}'e'$. The relevant Feynman diagram is shown in Figure 5.2 The cross section for such processes is suppressed by ϵ^2.

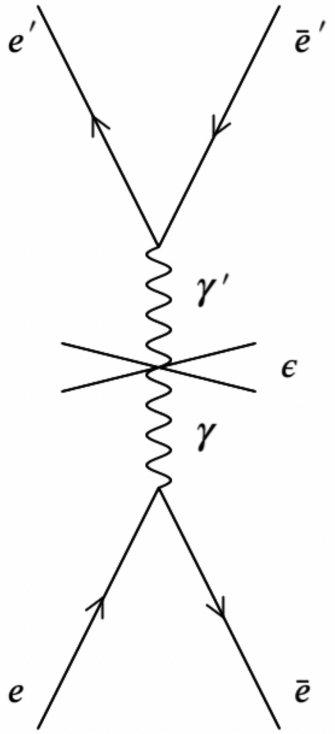

Figure 5.2 *Feynman diagram showing $\bar{e}e \to \bar{e}'e'$ induced via kinetic mixing. This interaction is signified by the cross on the photon propagator recreated from [57].*

In the mirror dark matter context, the total energy density of the universe has contributions from both ordinary and mirror particles. Thus, the Bose-Einstein/ Fermi-Dirac distributions of these particles are described by the temperatures of the relativistic species $(\gamma, \nu_\alpha(\bar{\nu}_\alpha)^3, e(\bar{e}))$ and their mirror counterparts $(\gamma', \nu'(\bar{\nu}'), e'(\bar{e})')$ that dominated the early times, where time is less and approximately equal to 1 second, i.e., T is approximately greater than 1 MeV.

[3]Here $\alpha = e, \mu, \tau$.

Mirror electron scattering rate

Since dark (specifically, mirror) electrons are electrically charged in the presence of kinetic mixing, they can scatter off ordinary electrons [205] and produce keV electron recoil signals. This can be modelled by approximating the target electrons as free and at rest relative to the speed v of the incoming mirror electrons. In this case, the Coulomb scattering of a dark electron off an electron yields a cross section of:

$$\frac{d\sigma}{dE_R} = \frac{\lambda}{E_R^2 v^2}, \tag{5.13}$$

where $\lambda \equiv \frac{2\pi\alpha^2\epsilon^2}{m_e}$, and E_R is the recoil energy of the scattered electron. Here, α is the fine structure constant, m_e is the electron rest mass, and ϵ is the kinetic mixing parameter.

Treating the target electrons as free is only valid for loosely bound atomic electrons, i.e., those with binding energy much less than E_R. Let g_T denote the number of electrons per target atom with atomic binding energy E_B, where $E_B \ll E_R$. Generally, the number of loosely bound electrons, those with $E_B \ll E_R$, far exceeds that of electrons with $E_B \sim E_R$. Thus, the approximation of the electron as free is expected to be reasonable. The electron scattering rate per target atom can then be approximated by replacing $\lambda \to g_T\lambda$ in Equation 5.13 [4]. The general differential rate of the e′-e scattering can be described as a product of the number of target atoms per kg of detector N_T, the mirror electron number density $n_{e'}$, and the integral over the differential cross section $\mathrm{d}\sigma/dE_R$ multiplied by the velocity distribution $f(\mathbf{v}; \mathbf{v}_E; \theta)$ of dark electrons arriving at the detector [57, 206]:

$$\begin{aligned} \frac{dR_e}{dE_R} &= N_T n_{e'} \int \frac{d\sigma}{dE_R} f(\mathbf{v}; \mathbf{v}_E; \theta) \, |\mathbf{v}| d^3v \\ &= g_T N_T n_{e'} \frac{\lambda}{E_R^2} I(\mathbf{v}_E, \theta), \end{aligned} \tag{5.14}$$

where the integral $I(\mathbf{v}_E, \theta)$ is defined as:

$$I(\mathbf{v}_E, \theta) \equiv \int_{|\mathbf{v}| > v_{\min}(E_R)}^{\infty} \frac{f(\mathbf{v}; \mathbf{v}_E; \theta)}{|\mathbf{v}|} d^3v. \tag{5.15}$$

[4] Note that nuclear recoils from scatterings of mirror nuclei with xenon nuclei in the detector are also expected. However, there is significant uncertainty in the rate, as the fractions of different nuclei in the mirror halo are not well known.

Here, the minimum velocity required for a recoil energy E_R is given by:

$$v_{\min} = \frac{1}{\mu}\sqrt{\frac{m_e E_R}{2}}, \tag{5.16}$$

for the special case in which the dark electron is a mirror electron, where μ, the reduced mass, is given by:

$$\mu = \frac{m_e m_{e'}}{m_e + m_{e'}} = \frac{m_e}{2}. \tag{5.17}$$

The velocity distribution $f(\mathbf{v}; \mathbf{v}_E; \theta)$ will depend on the velocity of the halo wind as measured from Earth $\mathbf{v}_E(t)$ plus the angle between the direction of the halo wind and the zenith at the detector's location θ(t).

To determine the local scattering rate of $e' - e$ in the vicinity of the Earth, assume that the velocity distribution is given by a Maxwellian distribution [206]:

$$f_{e'}(\mathbf{v}) = \left(\frac{1}{\pi v_0^2}\right)^{\frac{3}{2}} \exp\left(\frac{-\left(\mathbf{v} - \mathbf{v}_E\right)^2}{v_0^2}\right) \tag{5.18}$$

where $v_0 = \frac{2T}{m_{e'}}$, $\mathbf{v}_E$ is the bulk velocity in the Earth (detector) frame and this is 232 km/s.

Evaluating this the velocity integral (Equation 5.14) gives:

$$\frac{dR_e}{dE_R} = \frac{N_T g_T n_{e_d} \lambda}{2E_R^2 \left|\mathbf{v}_E\right|}\left[\text{erf}\left(\frac{v_{\min} + \left|\mathbf{v}_E\right|}{v_0}\right) - \text{erf}\left(\frac{v_{\min} - \left|\mathbf{v}_E\right|}{v_0}\right)\right]. \tag{5.19}$$

Here the effective number of free electrons, g_T with binding energy $E_B < 1$ keV, is 44 in a Xe detector, $v_{min} \approx 26500\ (E_R/2\ \text{keV})^{\frac{1}{2}}$ km/s from Eq. 5.16 and erf(x) indicates the error function for x. Integrating over recoil velocities from a threshold energy E_t (taken to be 2 keV [206]) give:

$$R_e = N_T g_T n_{e'} \lambda \left(\frac{2m_{e'}}{\pi T}\right)^{\frac{1}{2}}\left(\frac{e^{-\frac{E_t}{T}}}{E_t} - \frac{\Gamma\left[0, \frac{E_t}{T}\right]}{T}\right), \tag{5.20}$$

where $\Gamma[0, z]$ is the upper incomplete gamma function. The rate above has limitations, as the velocity and density distribution of the plasma, in this case MDM, are position-dependent rather than constant as assumed here. Thus, it is crucial to account for the local distributions and flux of MDM.

Expanding $n_{e'}I$ in a Taylor series around the yearly average, where $\langle n_{e'}I\rangle \equiv n_{e'}/v_c^0$, results in a simple phenomenological model with an electron scattering rate of [205]:

$$\frac{dR_e}{dE_R} = g_T N_T n_{e'} \frac{\lambda}{v_c^0 E_R^2} \left[1 + A_v \cos\omega\,(t - t_0) + A_\theta(\theta - \bar{\theta})\right]. \tag{5.21}$$

Here, v_c^0 is the modified velocity distribution at Earth, N_T is the number of target electrons, $\lambda \equiv \frac{2\pi\alpha^2\epsilon^2}{m_e}$å and $n_{e'}$ is the number density of e′ arriving at the detector. The diurnal and annual modulation caused by the Earth's rotation and spin axis variation with respect to the incoming dark matter wind is described by the $A_\theta(\theta - \bar{\theta})$ term, while the annual modulation caused by the Earth's change in velocity with respect to the dark matter halo is described by the $A_v \cos w(t - t_0)$ term. The modulation constants in this equation are $w = \frac{2\pi}{year}$, $t_0 = 153$ days (2nd of June) and the two modulation amplitudes: $A_v = 0.7$ and $A_\theta = 1$ [206]. Here, $g_T(E_R)$ is the effective number of free electrons with atomic binding energy E_b less than recoil energy E_R, modelled as a step function for the atomic shells in xenon. The next section will discuss how the effects of capture and shielding are adjusted in Section 5.21 to find the rate of electron - mirror scattering.

Effects from capture and shielding

The halo of spiral galaxies is assumed to exist as a multicomponent spherical dark-matter plasma halo consisting of e', H', He', Fe',... [206] This model assumes that the binding energy of a mirror hydrogen atom is less than the temperature of the mirror electron so that in principle this plasma can be ionised via interactions with e' or γ' collisions, leading to capture.

When dealing with plasma dark matter models, such as mirror dark matter, it is also important to consider the capture of dark matter by the Earth [207]. In this type of plasma dark matter model, MDM loses energy through kinetic mixing interactions with ordinary matter and is then captured. After a significant amount of MDM has accumulated, further capture occurs due to energy loss from self-interactions. Eventually, MDM will thermalise with ordinary matter on Earth, forming an extended distribution that acts as a "dark ionosphere" and affects incoming MDM via collisional shielding or deflection. This effect arises because the upper layers of Earth-bound dark matter can become partially ionised as a result of interactions between halo mirror electrons and Earth-bound dark

matter. The consequence is a conducting layer that induces dark electromagnetic fields, which deflect the halo wind.

For a dark matter halo in hydrostatic equilibrium, the local mirror electron temperature is

$$T = \frac{\bar{m} v_{rot}^2}{2}, \tag{5.22}$$

where $\bar{m}$ is the average mass of halo particles and $v_{\rm rot}$ is the galactic rotational velocity [60]. Early-universe cosmology arguments suggest that the mirror helium mass fraction is approximately 90% [208]. Assuming a fully ionised plasma, this corresponds to an average particle mass of $m \approx 1.1$ GeV. Using $v_{\rm rot} \approx 220$ km/s and assuming that the halo is in hydrostatic equilibrium, the expected local mirror electron temperature is around 0.3 keV. Therefore, in this analysis, only mirror electron temperatures in the range 0.1-1.0 keV are considered.

Interactions with the dark ionosphere are extremely difficult to model, but modelling the effects of collisional shielding of the detector from the halo wind due to Earth-bound dark matter is possible. Referring back to the Coulomb scattering cross section (Equation 5.13), we see that $\frac{d\sigma}{dE_R} \propto \frac{1}{v^2}$ and the collision length $\propto v^2$. Therefore, above large enough v, let's call this the cutoff velocity v_{cut}, the effect of collisions becomes negligible as the scattering length exceeds the available distance. When $v > v_{cut}$, collisions do not need to be considered whereas for $v < v_{cut}$, the collisions are significant until the e$'$ is reduced to approximately 25 keV (as after this the energy loss due to the captured mirror helium is no longer important). The cutoff velocity is modelled as [207]:

$$v_{cut}^4 \approx \frac{16\pi}{m_e^2} \alpha^2 \Sigma \log \Lambda, \tag{5.23}$$

where $\Lambda \sim \frac{T}{E_{min}} \approx 20$. The column density Σ is calculated by integrating the number density of captured mirror helium nuclei over the path of the incoming mirror dark particle as following:

$$\Sigma(\psi) = \int n_{He'} \mathrm{d}\ell = n_{he'}\left(R_E\right) \int e^{-\lambda_s d(\psi)} d\ell, \tag{5.24}$$

$$d(\psi) = \sqrt{\ell^2 + R_E^2 - 2\ell R_E \cos\psi}, \text{ for } \frac{\pi}{2} \leq \psi \leq \pi. \tag{5.25}$$

The argument ψ here is the angle between the direction of the incoming e$'$ and the

zenith at the detector's location and ℓ is the distance travelled. In this notation, for $\psi = \pi$ represents a particle travelling vertically down and in this direction, the column density is a minimum. Here, the number density of mirror helium within the Earth's atmosphere, found by solving the hydrostatic equilibrium, is given by:

$$n_{He'}(r) = n_{He'}\left(R_E\right) e^{-\lambda(r-R_E)}. \tag{5.26}$$

By substituting an energy-dependent factor for the velocity dispersion, the Maxwellian distribution that describes the velocity distribution is also altered for v below the cutoff velocity, yielding:

$$\frac{1}{v_c^0} = \frac{1}{N}\int_{|v|>y}^{\infty} \frac{e^{-v^2/v_0^2}}{v_0^3\pi^{3/2}|v|} d^3v = \frac{1}{Nv_0\sqrt{\pi}} \int e^{-y^2/v_0^2} d\cos\psi, \tag{5.27}$$

where $y = Maximum\left[v_{cut}(\phi), v_{\min}\left(E_R\right)\right]$, the velocity dispersion $v_0 = \sqrt{2T/m_e}$, $v_{min}(E_R) = \sqrt{2E_R/m_e}$ is the minimum velocity needed to produce a recoil of energy E_R and $k \equiv v_0^3\pi^{3/2}$. This was done by converting to polar coordinates. The normalisation factor N is:

$$N = \int_{|v|<v_{\rm cut}}^{\infty} \frac{e^{-v^2/v_0^2}}{v_0^3\pi^{3/2}} d^3v. \tag{5.28}$$

The number density of e' the high-velocity component arriving at the detector on Earth is related to the density far from Earth, $n_{e'}^{far} = 0.2$ cm^{-3}, by [207]:

$$n_{e'}^0 = N n_{e'}^{far}, \tag{5.29}$$

where $n_{e'}^{far} = 0.2$ cm^{-3} is the number density far from the Earth [209].

Both $n_{e'}^0$ and v_c^0 are functions in terms of the number density of He$'$ at the Earth's surface $n_{He'}(R_E)$, electron recoil energy E_R and mirror electron temperature T. Figure 5.3 shows the velocity distribution as a function of the recoil energy E_R, where at low E_R, the average $|v_c^0| >> v_{min}$, so most particles can produce recoil of energy E_R. For larger, the average E_R, $|v_c^0| < v_{min}$ so there will be mirror electrons that have sufficient energies to produce recoil. Thus, this integral is suppressed and causes a sharp rise in v_c^0.

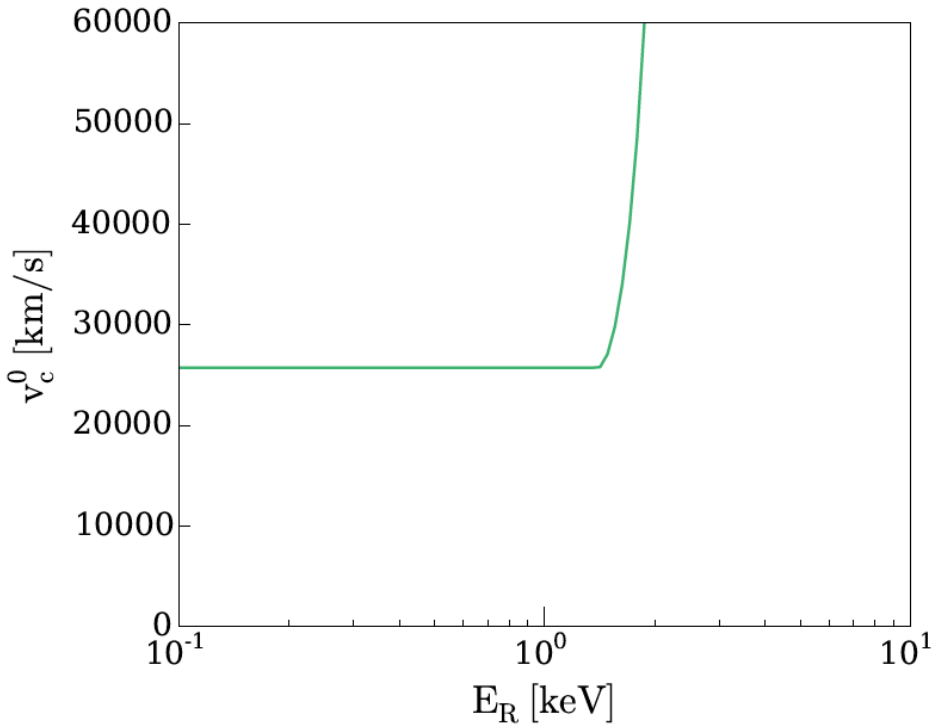

Figure 5.3 *v_c^0 as a function of electron recoil energy, constant at low energy due to independence from v_{min} then rising sharply at higher energy where v_{min} exceeds the mean particle velocity.*

Modulation

Significant yearly and sidereal modulations are predicted in plasma dark matter models [206]. The Earth's orbital motion around the Sun is the cause of both modulations, however, it was necessary to distinguish between the two different sources of modulation. The Earth's speed in relation to the dark matter halo is the source of the annual modulation, while the Earth's spin axis in relation to the wind is the source of the sidereal modulation.

Both mirror dark matter and general plasma dark matter scattering with electrons can be described by equation 5.21. As previously described, the $A_v \cos(w(t-t_0))$ term represents the annual modulation due to the variation of the Earth's speed with respect to the dark matter halo. Here, $w = 2\pi/365$ day and an annual modulation amplitude $A_v \sim 0.7$ with a maxima/ phase around June 2nd (152 days) [207].

Whereas the $A_\theta(\theta - \bar{\theta})$ term describes the sidereal modulation due to rotation of the Earth with respect to the direction of the plasma wind and the subsequent

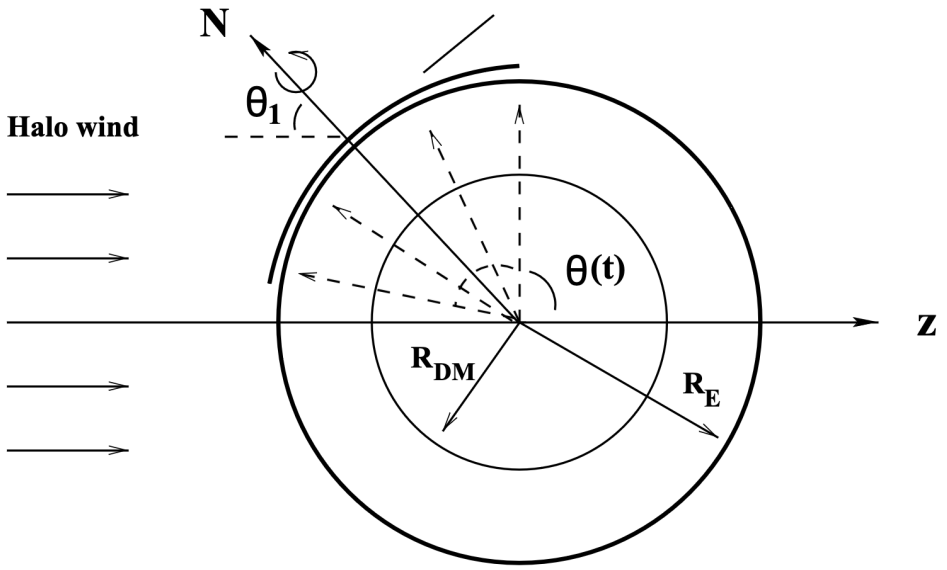

Figure 5.4 *The geometry of the dark halo wind interaction with the dark sphere of radius R_{DM} within the Earth, taken from [205]*

time-dependent position of the detector throughout the day. This is depicted as $\theta(t)$ in Figure 5.4, the time-dependent angle between the halo wind and zenith. The sidereal amplitude is approximately 1.0 and has been calculated in [210]:

$$\cos\theta(t) = -\sin\theta_1(t)\cos\theta_{lat}\cos\left(\frac{2\pi t}{T_{day}}\right) - \cos\theta_1(t)\sin\theta_{lat} \tag{5.30}$$

and $\cos\theta_1(t)$ is defined as:

$$\cos\theta_1(t) \simeq \cos\bar{\theta}_1 + y\left[\cos\bar{\theta}_1\cos\gamma\sin\left(\frac{2\pi\,(t-T_1)}{\text{year}}\right) + \sin\theta_{\text{tilt}}\,\sin\left(\frac{2\pi\,(t-T_2)}{\text{year}}\right)\right]. \tag{5.31}$$

Here, the sidereal day $T_{day} = 1$ day, the latitude of the detector's location is $\theta_{lat} = 44°$ for the LZ detector at SURF, the angle between Earth's spin axis and the normal to the ecliptic plane is $\theta_{tilt} = 23.5°$, and the angle between the normal of the ecliptic plane and the direction of the halo wind is $\gamma = 60.0°$. The time terms are $T_1 = t_0 + 1/4$ year $= 244$ days and $T_2 = 172$ days (summer solstice). The ratio of the parallel and perpendicular components of Earth's velocity is given by $y = 0.13$. The time variation of θ(t) for other laboratory locations has been evaluated in [206] by replacing $\theta_{lat} \approx 44°, 36°, 28°$, and $-37°$ for Gran Sasso, Kamioka, China Jin-Ping, and Stawell, respectively.

To compute the expected rate using Equation 5.21 for a given data collection period, the weighted average of the modulation terms is calculated and plotted,

as shown in Figure 5.5. For the SR1 period, data taking began on 23 December 2021, corresponding to the 356^{th} day of the year, and ended 117 days later. This yields an average modulation factor of -0.141 for the period.

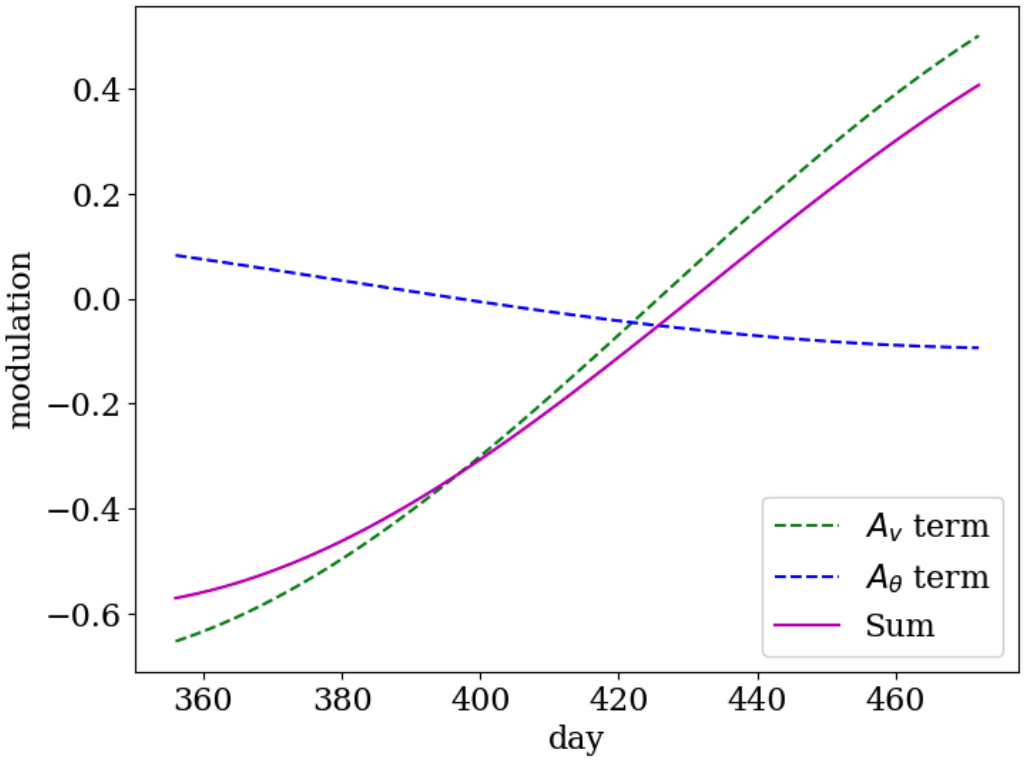

Figure 5.5 *Contributions from the modulation terms for LZ SR1 data. The starting date is 23 December 2021, and the end date of data collection is 18 April 2022. This corresponds to an average modulation factor of* -0.141 *for SR1.*

Note that this modulation factor is not used in the final analysis for two reasons. First, although the nominal SR1 data-taking period spans from 23 December 2021 to 18 April 2022, there were several pauses in data collection, and many days within this interval were excluded from the final dataset. As a result, it is uncertain whether the SR1 dataset contains sufficient data to reliably observe the expected modulation effects. Second, the modulation factor ultimately only scales the mirror electron signal spectrum and, in theory, does not affect the calculated number of "observed" events at 90% confidence level. Given that the scaling factor is approximately 0.1, small enough not to significantly affect the result, the author chooses to use a value of 1, which corresponds to the modulation effect averaged over a full annual cycle or over a sufficiently sampled dataset.

5.1.4 Other signal models

Other signal models beyond the standard model that could produce low-energy ER signals in the LZ active volume are displayed in Table 5.1. The limits for all the low-energy ER signal models using SR1 data, excluding MDM which has not been published, are reported in Ref. [1]. Only the two mono-energetic signals—ALPs and HPs plus MDM that this author worked on will be covered in depth.

5.2 Analysis framework

The general analysis framework adopted by LZ to set limits on a dark matter signal using SR1 data is shown in the workflow in Figure 5.6. In this framework, all the background spectra are already calculated, computed and simulated for a given exposure, which is SR1 data consisting of 60 livedays and 5.5 tonnes of LXe. The framework here is applied to the beyond the standard model (BSM) scenarios that would produce low energy ER signals in the active LXe, which will be discussed later in this chapter: two monoenergetic signals (ALPs and HP) and mirror dark matter (MDM).

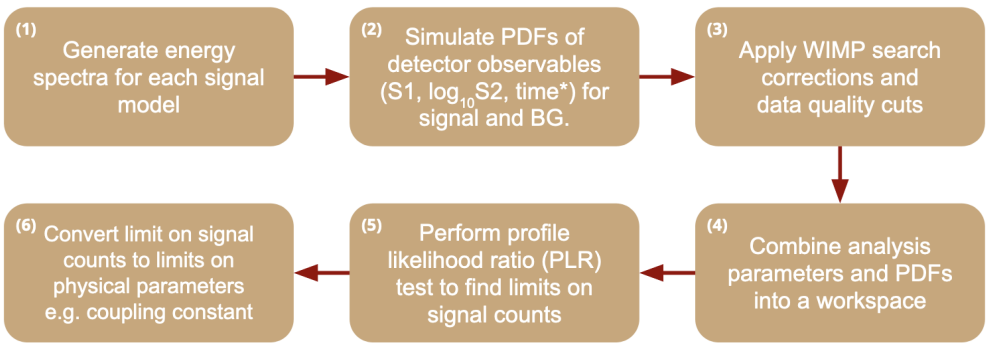

Figure 5.6 *The general analysis framework adopted by LZ to search for novel physics via the low energy electron recoil channel.*

For each stage in the analysis framework, additional details for each step is provided:

1. For each signal model, a unique energy recoil spectrum (also known as the true energy spectrum) is computed using relevant cross-section, coupling

constant or other physical parameter. For example, the energy spectrum of solar axion is computed using the cross-section for the axio-electric effect, which employs an arbitrary axion-electron coupling constant, g_{ae}.

2. The energy spectrum is input into the LZ software LZLAMA (LZ Light Analysis Montecarlo Application), which simulates the detector responses to interactions occurring inside the LZ detector. This package utilises the NEST software package [116] and produces a set of reduced quantities (RQs) in the same file format as the data collected using the LZ processing pipeline. For low-energy ER searches, time is added as a detector observable of interest, in addition to S1c and $\log_{10}$S2c used in WIMP searches. A more detailed discussion on the reasoning behind this is provided in Section 5.4.1.

3. The same data and selection treatment used in WIMP-search, previously discusses in Section 4.2.1, are applied to the simulated signal (and backgrounds) model.

4. Combine all the simulated signal and background PDFs into a workspace. The workspace should include the dataset, the expected counts, and the constraints, which are calculated from an extensive radioassay campaign conducted over six years [138], for each background component over the same exposure as the data.

5. Applying the PLR test using the workspace from point (4) using an internal software called LZStats. This calculated the number of signal at the 90% confidence level for the signal model.

6. Convert the 90% confidence level on the number of signal to 90% confidence level on the physical parameter that is relevant to the input signal model. For example in the case of solar axion, that would its axion-electron coupling constant, g_{ae}.

5.3 Signal models

Table 5.1 shows signal models [1] studied by LZ with their limits using SR1 data, excluding MDM, which is not included in the paper. The table categorises dark matter halo particles, excluding mirror dark matter, as being used to study both bosonic and fermionic dark matter models, while particles originating from

Signal model	Origin	Motivation	Interaction and coupling of interest
Neutrino magnetic moment & millicharge	Sun	BSM	Neutrino-electron scattering: 1. solar neutrino magnetic moment μ_ν and effective millicharge δ_Q
Solar Axion	Sun	BSM - broken global U(1)	Axion-electron coupling g_{ae}
Migdal effect sensitivity to WIMPs search	Galactic halo	SUSY and thermal relic abundance	Migdal effect, which is electron recoil enhancement of nuclear recoils σ_{SI}
Axion-like particles	Galactic halo	BSM - broken global U(1)	ALP absorption via the axio-electric effect g_{ae}
Hidden (dark) photon	Galactic halo	Hidden sector	Kinetic mixing κ
Mirror dark matter	Galactic halo	Hidden sector	Kinetic mixing ϵ

Table 5.1 *A summary of the searches conducted by the LZ Low Energy ER group. The table categorises each signal, its corresponding origin, theoretical motivation, and expected interaction in the LZ detector.*

the Sun are used to explore Beyond the Standard Model (BSM) physics. Both axions, ALPs, and hidden photons arise from a broken U(1) symmetry group, generating bosons. These bosons are absorbed by the xenon atomic electrons via an effect analogous to the photoelectric effect, whereas fermionic dark matter and neutrinos scatter off the electrons.

5.3.1 The monoenergetic signals: ALPs and HPs

In the LZ detector, the signature we expect to see for ALPs and HPs are mono-energetic signals since both could be detected in LZ as absorption by the atomic electron via the axio-electric effect. In the case of galactic ALPs, where the velocity is non-relativistic, the spectral signature is a mono-energetic peak (a line feature) corresponding to the ALP rest mass. Following references [172, 202] and using factors from Ref. [211], if ALPs constitute all of the cold DM in the galaxy with $\rho = 0.3$ GeV/cm^3 [212], the expected ALP event rate (kg^{-1}day^{-1}) in an earthbound detector is given by

$$R_{\mathrm{ALP}} \simeq \frac{1.5 \times 10^{19}}{A} g_{\mathrm{ae}}^2 \sigma_{\mathrm{PE}} m_{\mathrm{ALP}}, \tag{5.32}$$

where A is the average mass number of xenon (131.29), m_{ALP} is ALP mass in keV/c^2, and g_{ae} is the ALP-electron coupling constant.

Similarly, the absorption of a HP to a bound electron is again analogous to the photo-electric effect, with the photon energy replaced by the HP rest mass m_{HP}. Following the prescription in Ref. [172] and pre-factors in Ref. [211], if HP constitutes the DM in the universe, the HP absorption rate (kg^{-1}day^{-1}) in a terrestrial detector is given by

$$R_{\mathrm{HP}} \simeq \frac{4.7 \cdot 10^{23}}{A} \kappa^2 \frac{\sigma_{\mathrm{PE}}}{m_{\mathrm{HP}}}, \tag{5.33}$$

where m_{HP} is HP mass in keV/c^2, and κ is the HP kinetic mixing parameter. Both these mono-energetic signal models has a dependency on σ_{PE} which is the photo-electric cross section of the target medium, which is xenon in this case, as shown in Figure 5.7.

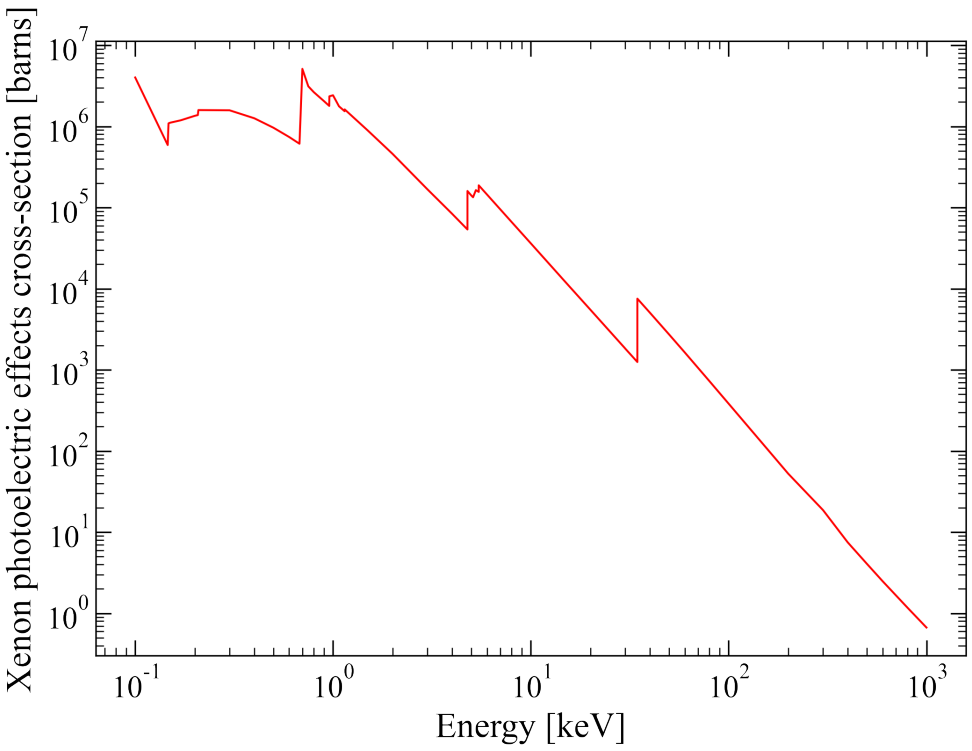

Figure 5.7 *The photoelectric cross section of xenon σ_{PE} in barns as a function of energy. Plot produced using data provided from [213].*

The expected energy deposition spectrum for these two models should be a mono-

energetic peak centred at the value of incident mass and smeared by the resolution of the detector such as shown later in Figure 5.10.

5.3.2 Mirror dark matter

Mirror dark matter could result in keV-scale electron recoils in the LZ detector via kinetic mixing interactions between mirror electrons, e', and xenon atomic electrons, e. The interaction rate is described by Equation 5.21, taking into account modulation effects, as well as the capture and shielding of mirror electrons within the Earth's atmosphere. These factors contribute to the predicted recoil energy spectra for mirror electrons as a function of temperature, as shown in Figure 5.8.

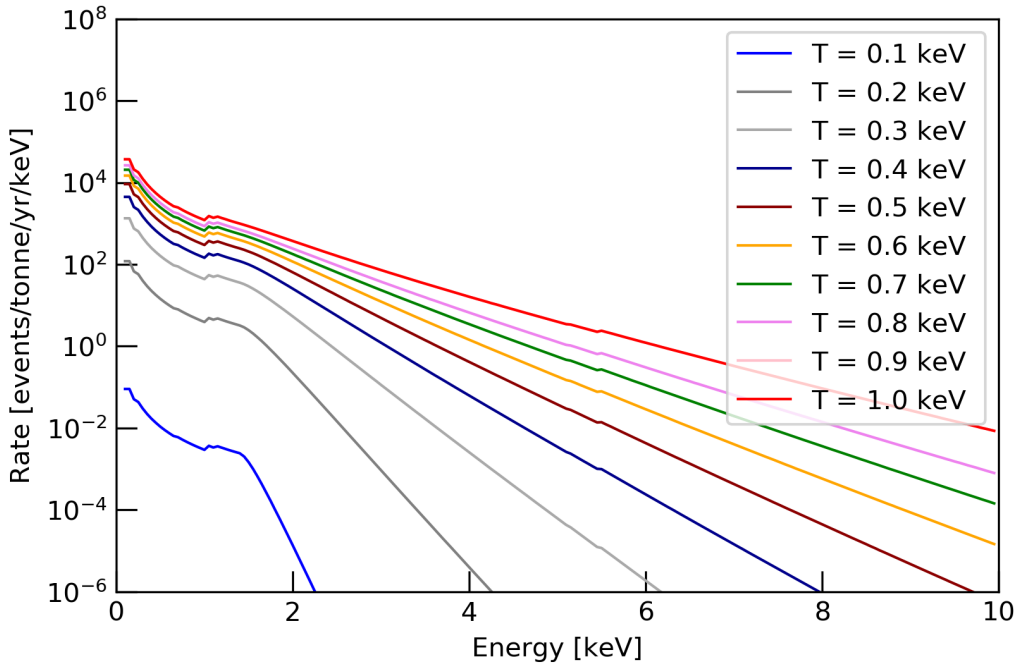

Figure 5.8 *The ER rate-energy spectrum for mirror electron as a function of temperature including the effects of shielding and capture. In this plot, the kinetic mixing is* 1×10^{-10} *for local mirror electrons temperature from 0.1 - 1.0 keV.*

As previously discussed in Section 5.1.3, assuming that the local dark matter halo is in hydrostatic equilibrium and adopting the Milky Way's rotational speed, $v_{\text{rot}} \approx 220$ km/s, the local mirror electron temperature is expected to be approximately 0.3 keV. Therefore, the temperature range chosen for this analysis is 0.1–1.0 keV. The shoulders or the dips that appear in all the mirror electron

energy spectra as shown in Figure 5.8, before 2 keV, are due to the shielding effects from the captured mirror dark matter within the Earth.

Other signals

Figure 5.9 shows the reconstructed energy spectra for all the signal models investigated in Ref. [1]. The energy range spans 0–15 keV, and the spectra are scaled to the expected rates for each model in an Earth-bound detector, in units of events/tonne/year/keV. The analysis exploits sensitivity to energy depositions within this range, benefiting from well-studied background components and simulated probability density functions (PDFs) available within the LZ collaboration.

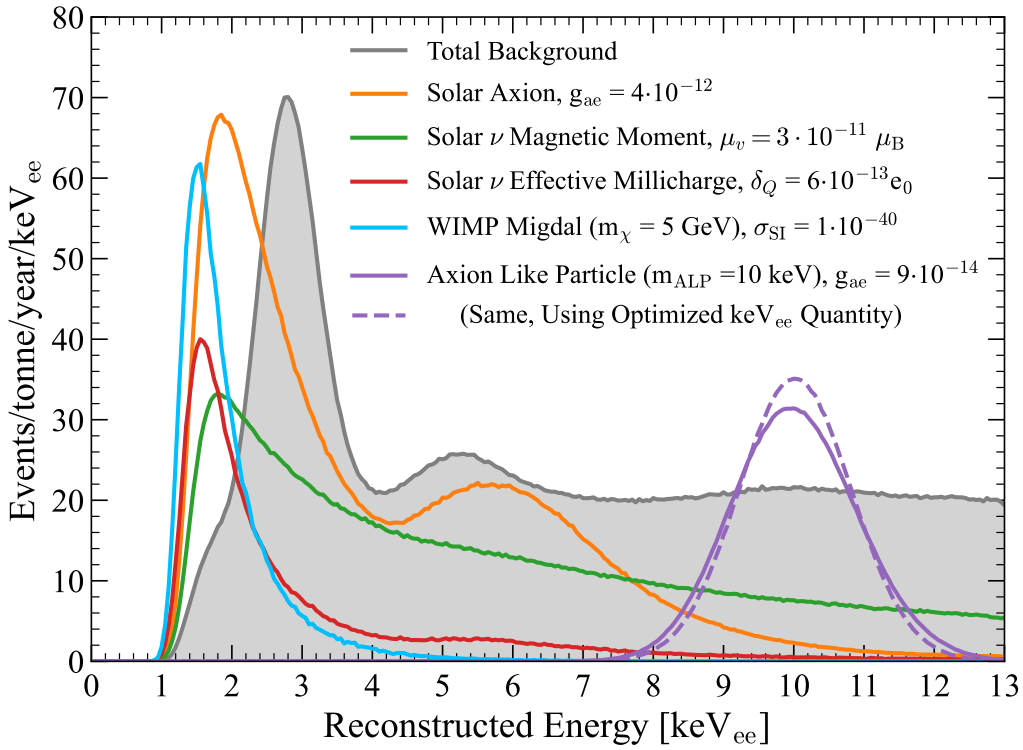

Figure 5.9 *Reconstructed energy (keV_{ee}) spectra for the background-only model (grey) and representative signal models: solar axion (orange), solar neutrino magnetic moment (green), solar neutrino millicharge (red), spin-independent (SI) WIMPs undergoing the Migdal effect (blue), and axion-like particles (ALPs) (purple). To generate these spectra, the detector S1 and S2 response are simulated and then all data selections, thresholds, and data quality acceptances are applied. The normalisation of the models in this plot, including the cross sections and coupling constants, is arbitrary and intended solely for visualisation purposes. Taken from [1].*

5.3.3 Simulation

In general, for each signal model, the computed energy spectra (true recoil energy spectra) are used to simulate detector responses in S1 and S2. All data selections, thresholds, and data quality acceptances are then applied. The simulated observables, S1 and S2, can be used to reconstruct the energy spectra as previously described by Equation 2.20 in Chapter 2 as shown in Figure 5.10, and mapping the signals into the parameter space of interest, $\{S1c, \log_{10} S2c\}$. As with the modelling of backgrounds, the same suite of data selections and data quality acceptances has been applied to these signal models in the reconstructed observable space. These simulated signal distributions in $\{S1c, \log_{10} S2c\}$ space are then employed as probability distribution functions (PDFs) for statistical inference. Figure 5.11 shows the distribution in $\{S1c, \log_{10} S2c\}$ space for a monoenergetic signal with corresponding masses of 5 and 10 keV. Similarly, for mirror electrons, Figure 5.12 shows the reconstructed energy and Figure 5.13 shows the simulated distributions of mirror electrons at different temperatures in $\{S1c, \log_{10} S2c\}$ space.

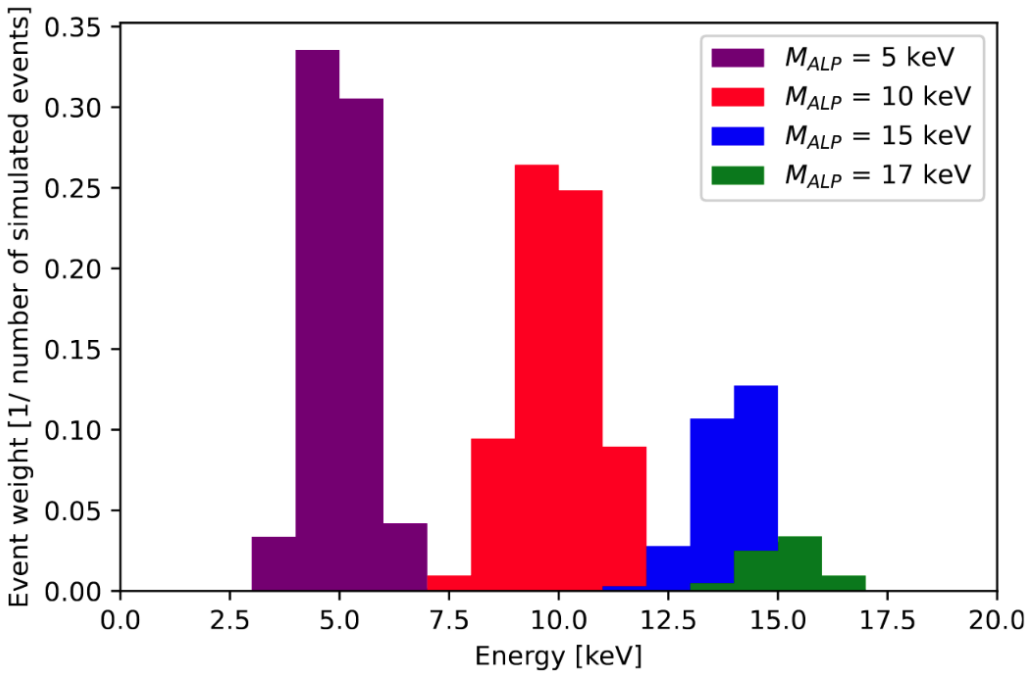

Figure 5.10 *The reconstructed energy plot for monoenergetic signals taking into account of the LZ detector's resolution and efficiency at different energies.*

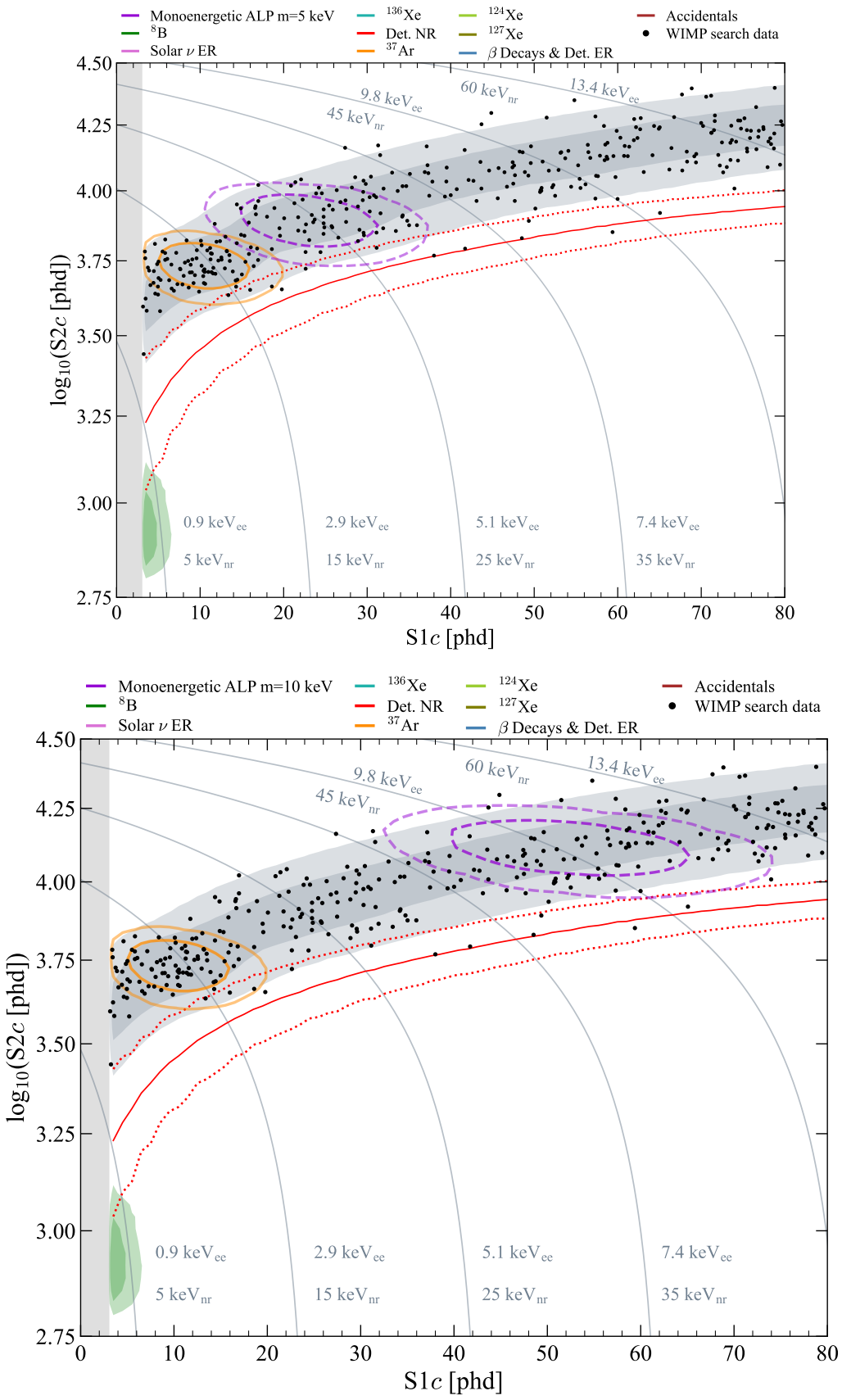

Figure 5.11 *Distribution of monoenergetic signal of masses 5 keV (top) and 10 keV (bottom) in* $\{S1c, \log_{10} S2c\}$ *signal space represented by the purple contours.*

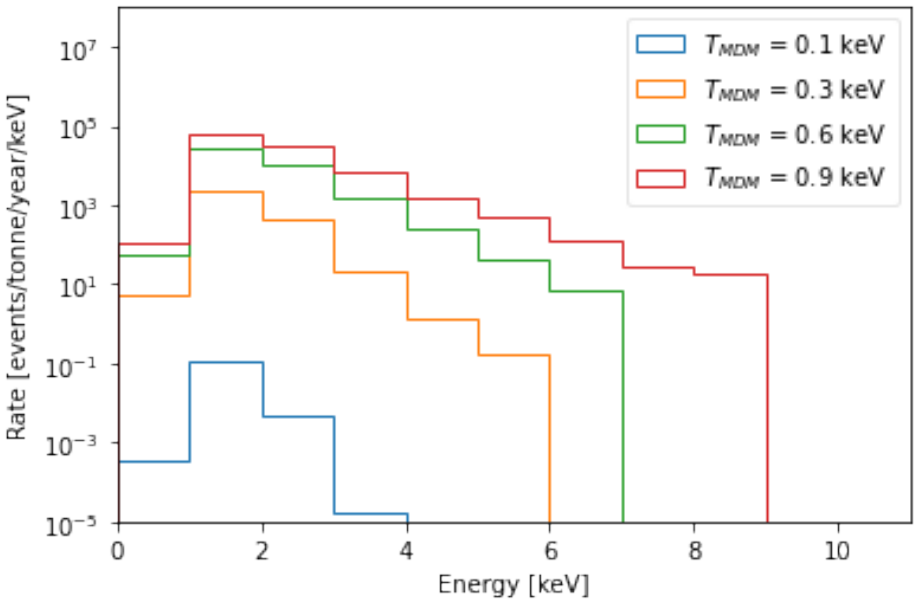

Figure 5.12 *Reconstructed energy for mirror electrons with temperatures = 0.1, 0.3, 0.6 and 0.9 keV taking into account of detector responses and efficiencies.*

5.4 Statistical analysis

The primary objective of every direct detection dark matter experiment is to test signal models against the collected data, considering the expected background rate description. If no signal is detected, it is possible to establish a statistical limit on the number of signal events or specific physical parameters of the signal model. Similar to the WIMP search, profile likelihood ratio (PLR) analysis is the preferred statistical method used in this study. This section will cover the analysis approaches used in low-energy electron-recoil searches, which is builds on the analysis and statistical framework of LZ WIMP search results in Chapter 4. The same data selection and cuts described in Section 4.2.1 for WIMP search are also applied to the low-energy ER searches.

5.4.1 Profile likelihood ratio

"Likelihood" is often referred as a function of the parameters of the statistical model, given some data. Likelihood functions describes the compatibility of a given data set with different hypotheses and it can be used to estimate parameters. This leads to the profile likelihood ratio test to be chosen as the statistical

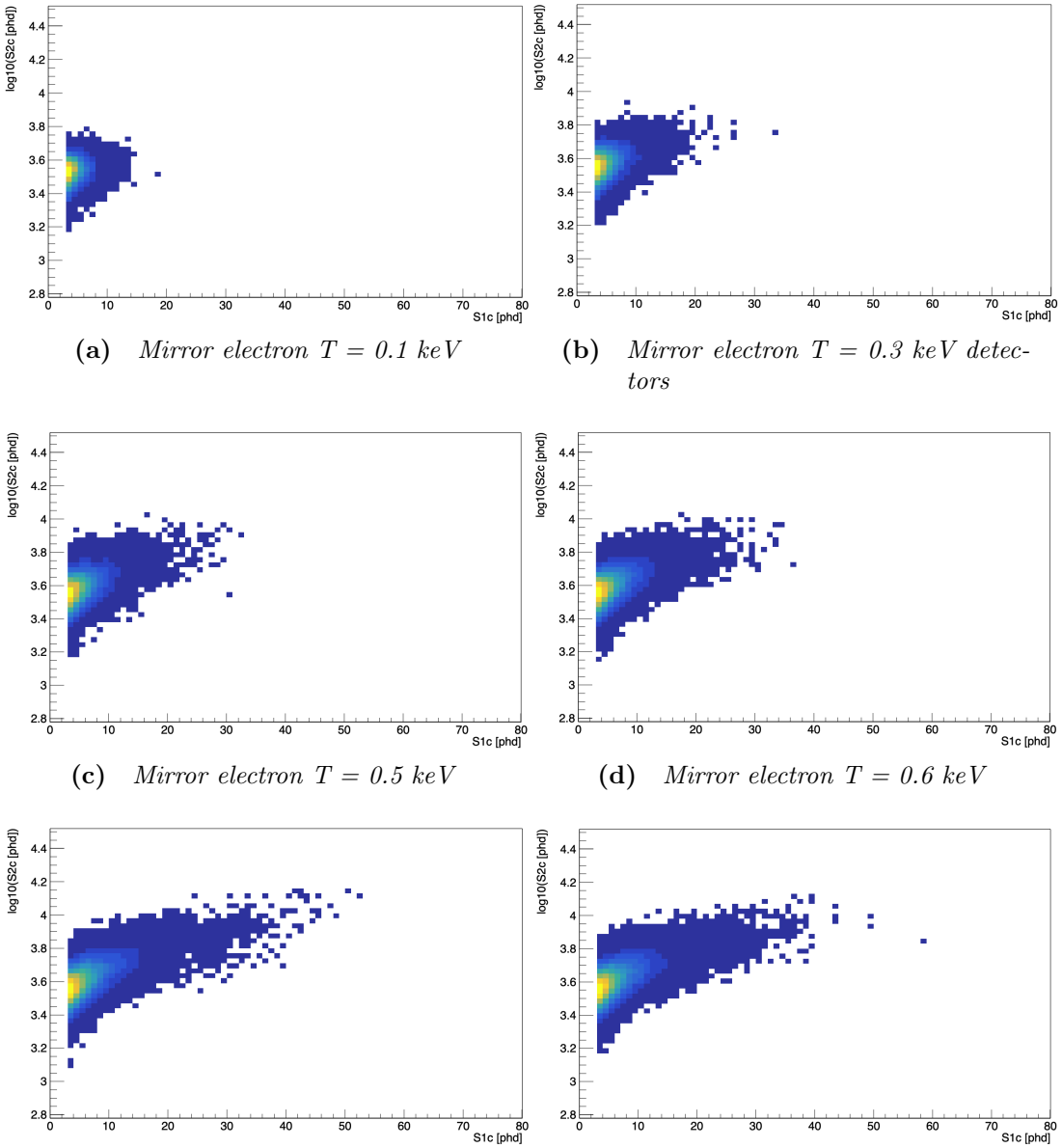

(a) *Mirror electron $T = 0.1\ keV$*

(b) *Mirror electron $T = 0.3\ keV$ detectors*

(c) *Mirror electron $T = 0.5\ keV$*

(d) *Mirror electron $T = 0.6\ keV$*

(e) *Mirror electron $T = 0.9\ keV$*

(f) *Mirror electron $T = 1.0\ keV$*

Figure 5.13 *Simulated distribution of mirror electron of temperature = 0.1, 0.3, 0.6 and 0.9 keV in $\{S1c, \log_{10} S2c\}$ space.*

approach in search experiments.

Incorporating time into the likelihood

The estimated rate of ^{37}Ar in the 10-tonne xenon volume has a prior on the number of events ranging from 0 to 288 out of a total of 333 events in the SR1 dataset, as previously reported in the WIMP search background Section 4.3 [145]. The concentration of ^{37}Ar in 10 tonnes of xenon was estimated using the Sillberg and Tsao spallation model in conjunction with the amount of time the sample was exposed above ground, resulting in a high degree of uncertainty on its rate in SR1. Compared to WIMP signals, the low energy ER signals are statistically more influenced by the ^{37}Ar background since both are likely to be found in neighbouring or overlapping regions of the ER bands in S1c-log$_{10}$S2c signal space. This is especially true for signals that are mono-energetic around 2.82 keV.

To enhance the sensitivity in low-energy ER searches, time was incorporated as an additional observable into the existing likelihood function from Equation 4.1. This approach reduces the constraints in the statistical tests for each search, particularly for ^{37}Ar and ^{127}Xe, whose rates are expected to decrease over time as they decay. The inclusion of the time variable was also investigated in the WIMP sensitivity study; however, the WIMP sensitivity was found to be robust across a wide range of ^{37}Ar rates.

Thus the likelihood function used in the low-energy electron recoil search for a low-energy ER signal model f_s is defined as:

$$\begin{aligned}\mathcal{L}\left(\mu, \boldsymbol{\theta}\right) &= \text{Poiss}\left(N_0 \mid \mu_{\text{tot}}\right) \\ &\times \frac{1}{\mu_{\text{tot}}} \prod_{i=1}^{N_0} (\mu f_s(\text{S1}c_i, \log_{10}\text{S2}c_i, \text{t}_i) + \sum_{b=1}^{9} \mu_b f_b(\ \text{S1}c_i, \log_{10}\text{S2}c_i, \text{t}_i)) \\ &\times \prod_{b=1}^{9} g_b\left(\mu_b \mid \nu_b\right),\end{aligned} \tag{5.34}$$

where the PDFs for signal and background are a product of a time-dependent component $a(t)$ and the original PDFs, f(S1c, log$_{10}$S2c) from Section 4.1 in POI: S1c and log$_{10}$S2c. The new time-dependent signal or background PDFs is redefined as:

$$f(\text{S1}c, \log_{10}\text{S2}c, t) = a(t) \times f(\text{S1}c, \log_{10}\text{S2}c). \tag{5.35}$$

The PDF $a(t)$ is the product of two separate time-dependence:

$$a(t) = T_{\text{live}} \times R(t), \tag{5.36}$$

where T_{live} is a histogram of the detector live-time over the course of the exposure, binned in 10-minute intervals and shown by the orange dashed line in Figure 5.14, and $R(t)$ encodes the time dependence associated with the expected rate for each signal or background component.

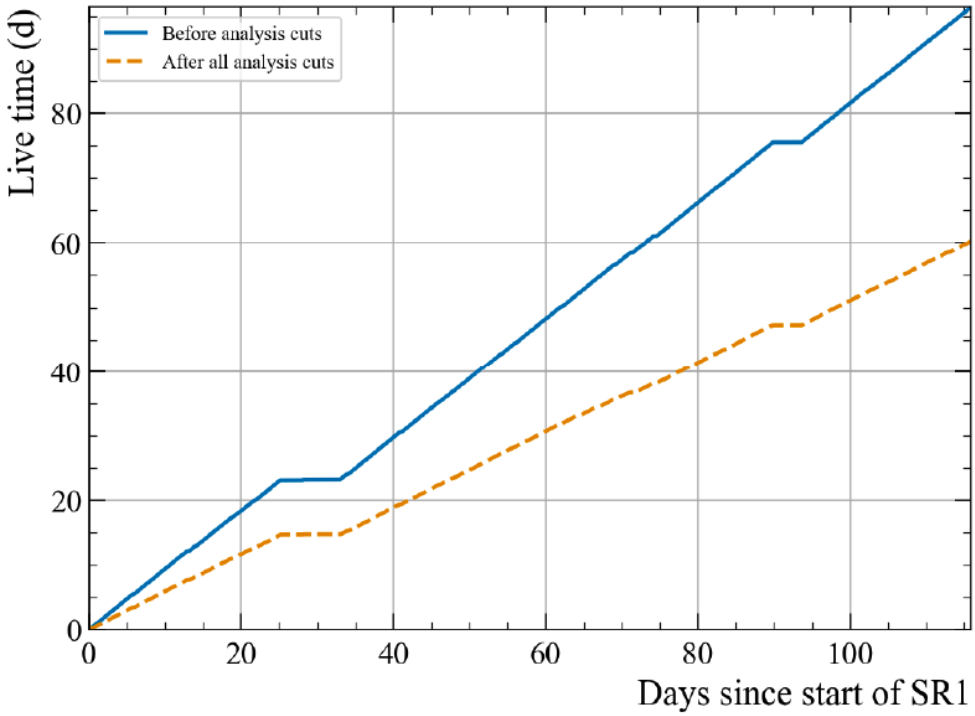

Figure 5.14 *The LZ detector's live time during the first research run (SR1), which provided data for the dark matter search. The dashed orange curve represents the live time following the application of analysis level vetoes, whereas the blue curve represents the live time corresponding to all gathered data. Plot produced by A. Fan and M. Buuck.*

The livetime histogram of T_{live} integrates to give the total live time of SR1. The function $R(t)$ is a constant for all the expected background components except for ^{37}Ar and ^{127}Xe as represented by Figure 5.15, where their time-dependence functions are modelled as exponential decays associated with their respective half-lives of 35.0 days and 36.3 days. Figure 5.15 shows the best fit of the background-only model to the data, conducted in {S1c, $\log_{10}$S2c, t} space projected onto the time axis. The results of this fit is consistent with the obtained results in 2D space {S1c, $\log_{10}$S2c} used in WIMP search. The ^{37}Ar and ^{127}Xe initial

rates are consistent with the estimation from cosmogenic activation backgrounds [145, 160], and thus the subsequent rates are consistent with exponential decay at the expected half-lives [154].

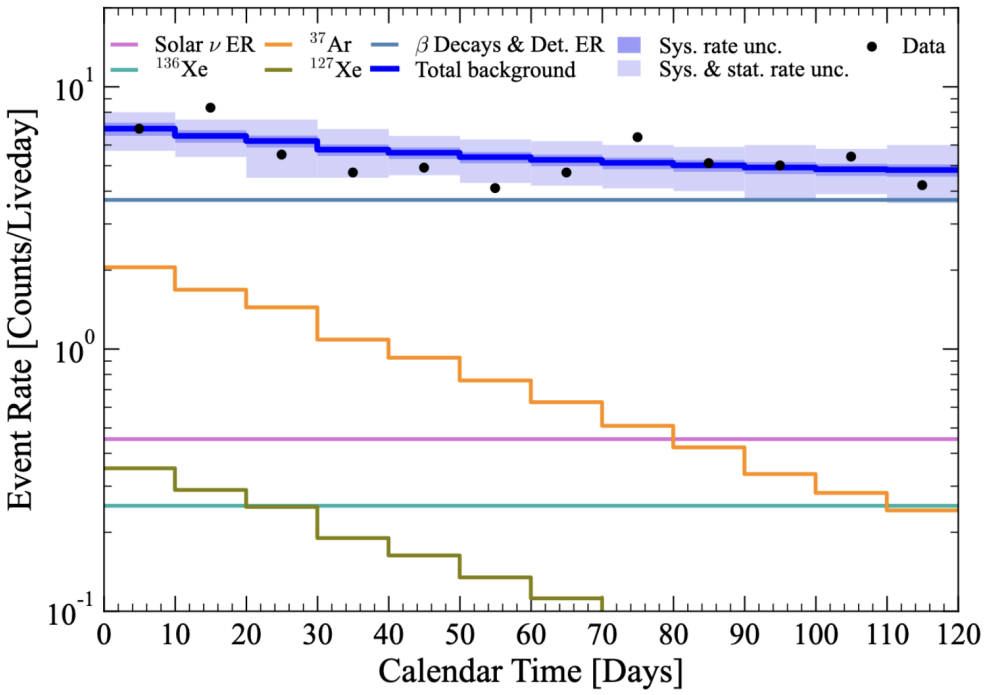

Figure 5.15 *Time dependence for all the background components and data in SR1. The blue line represents the summed background. The darker blue band shows the 1σ uncertainty in the model whereas the lighter blue band represents the combined model and statistical uncertainty. Plot taken from [1].*

Time dependence of other background components, such as ^{214}Pb, was also considered in this investigation. The variation in the rate of ^{214}Pb could potentially arise from LXe convection and thermodynamic conditions, such that the rates of ^{214}Pb progenies, ^{218}Po and ^{214}Po, were monitored. No significant time dependence for this was observed.

The new time-dependent framework was also applied to WIMP search to check the consistency in the two results [123] and there was a small improvement of <5% in the limit due to the small number of background counts expected in the NR signal regions in {S1c, $\log_{10}$S2c} space.

5.5 Results for the Low-Energy ER Searches

In all these searches, the p-value of the background-only hypothesis is greater than 10%. Once the 90% confidence limit on the number of signal events has been computed, it is converted into a 90% confidence limit on the physical parameter of the signal model in question. For ALP, HP, and MDM scenarios, the physical parameters of interest are the axioelectric coupling g_{ae}, and the kinetic mixing parameters κ and ϵ, respectively. This procedure can be generalised by denoting the relevant physical parameter as ϵ.

$$\epsilon(90\%\,\mathrm{CL}) = \epsilon(0)\left(\frac{n_{\mathrm{Sig}}(90\%\,\mathrm{CL})}{n_{\mathrm{PDF}}(0)}\right)^{n}. \tag{5.37}$$

Here, $\epsilon(0)$ is the arbitrary value of the physical parameter used to compute the signal model (true rate spectra), $n_{\mathrm{PDF}}(0)$ is the corresponding number of signal events, and $n_{\mathrm{Sig}}(90\%\mathrm{CL})$ is the 90% confidence limit on the number of signal events. For each respective signal, n depends on the associated rate equations, such as Equations 5.32, 5.33, and 5.21 for ALP, HP, and MDM, respectively. The value of n is 2 for HP, ALP, and MDM, since the rates for these signal models $\propto$ (coupling constant)^2, as shown previously.

5.5.1 Monoenergetic signals: ALP and HP results

The number of events at the 90% confidence level for monoenergetic signals as a function of mass is shown in Figure 5.16. ALP and HP masses ranging from 1 keV to 17 keV are considered. Sensitivity near the 2.82 keV energy of ^{37}Ar is enhanced by incorporating time dependence. Between 3.2 keV and 4 keV, random fluctuations in the data result in upper limits that fall more than 1σ below the median sensitivity. For this specific mass interval, we employ the Power Constrained Limit method [214] to avoid reporting a limit stronger than the -1σ boundary of the projected sensitivity. We note that the results from XENONnT searches in Ref. [215] do not apply a similar constraint to their monoenergetic models, so their 90% C.L. upper limits fall below the -1σ level for some masses.

The present work includes the time dependence of the ^{37}Ar and ^{127}Xe background contributions. To assess the impact of incorporating time dependence on the observed limits, the same statistical analysis was repeated with all time

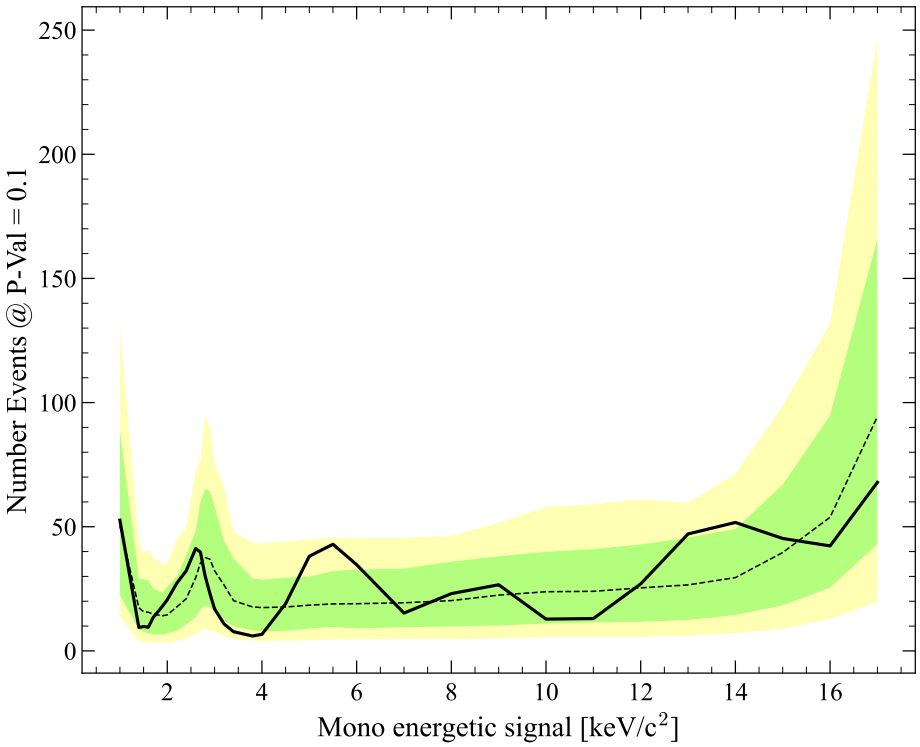

Figure 5.16 *The number of fitted signal events after background removal at 90% confidence level for SR1 as a function of mass in keV/c^2 for monoenergetic models. The solid black line shows the observed number of events, the dashed black line shows the median, and the brazil bands (green/yellow) represent the $\pm 1(2)\sigma$ of the number of events.*

dependence removed. As expected, the most significant effect occurs for monoenergetic signals near the 2.82 keV (K-shell) peak of ^{37}Ar. For example, for an ALP or HP with a mass of approximately 2.8 keV/c^2, the observed limit is weakened by a factor of three, as shown in Figure 5.17, which has been published in Ref. [1]. The inclusion of time dependence enhances sensitivity to a lesser extent for the other signals considered, in proportion to their overlap with the ^{37}Ar background—the dominant time-dependent background—centred around 2.7 keV$_{ER}$. Unfortunately, XENONnT, with an exposure of 1.16 ton-years, has stronger limits for the monoenergetic models (ALP and HP) compared to LZ, with an exposure of 0.9 ton-years. This is expected, as XENONnT has a slightly higher exposure, and there is also a difference in the ^{214}Pb rate, which gives XENONnT [215] greater sensitivity for a similar exposure.

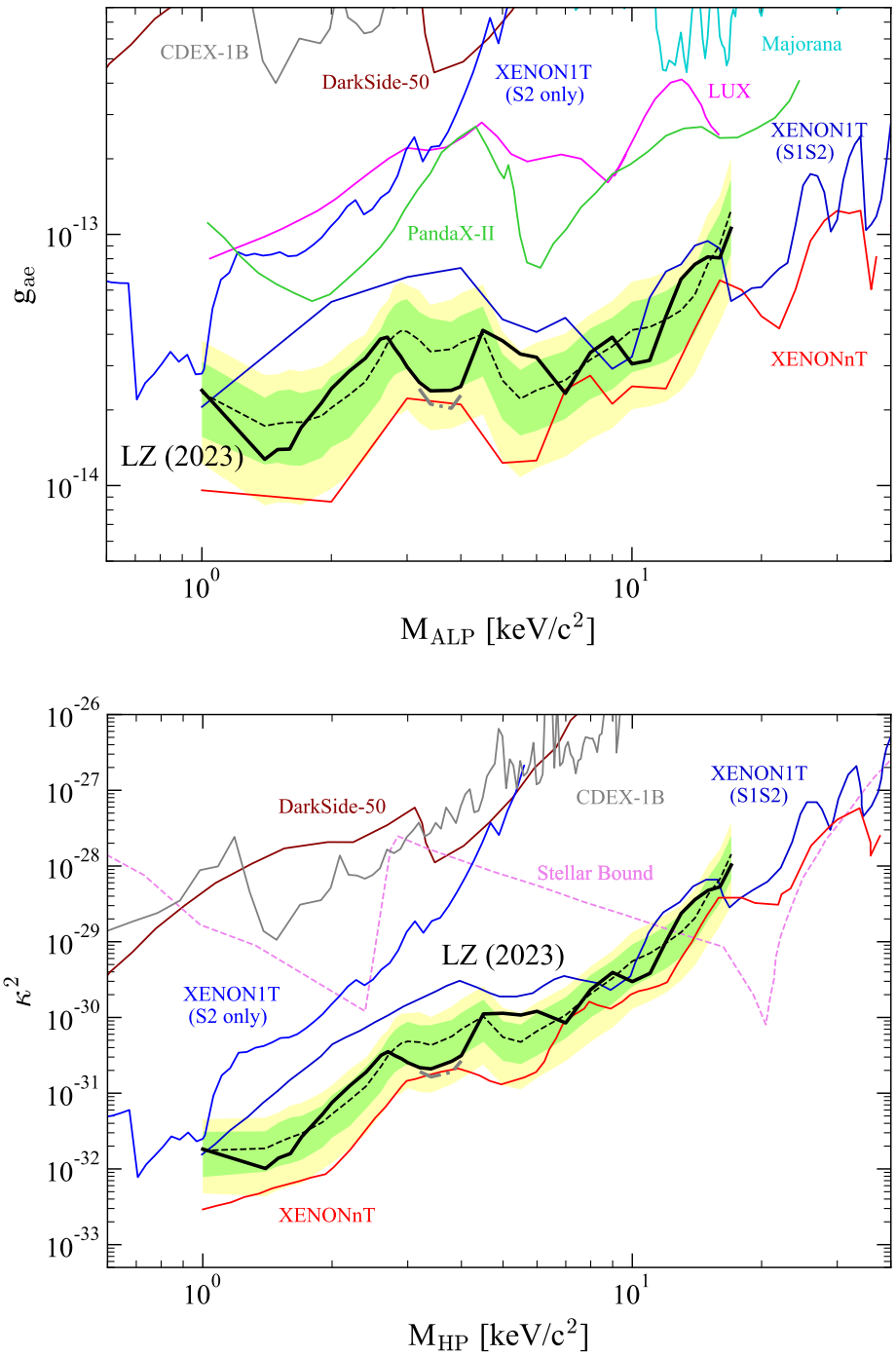

Figure 5.17 *The 90% C.L. upper limit (black line) on the ALP coupling constant, g_{ae} (top), and the HP coupling constant squared, κ^2 (bottom). The dashed grey lines represent the original 90% C.L. limit before the Power Constrained Limit procedure was applied. Selected limits from other experiments are also shown [215–223], along with astrophysical bounds in Ref. [224].*

5.5.2 Results for the MDM Search

Similarly, the number of events at the 90% confidence level for mirror electrons as a function of temperature is displayed in Figure 5.18. The MDM result shown in Figure 5.19 is not published at the time of writing this thesis. Although, as expected, the MDM search using SR1 data yields stronger limits than the LUX results, since the LUX data (118 kg × 95 days) has approximately 30 times less exposure than the SR1 data (5.5 tonnes × 60 days).

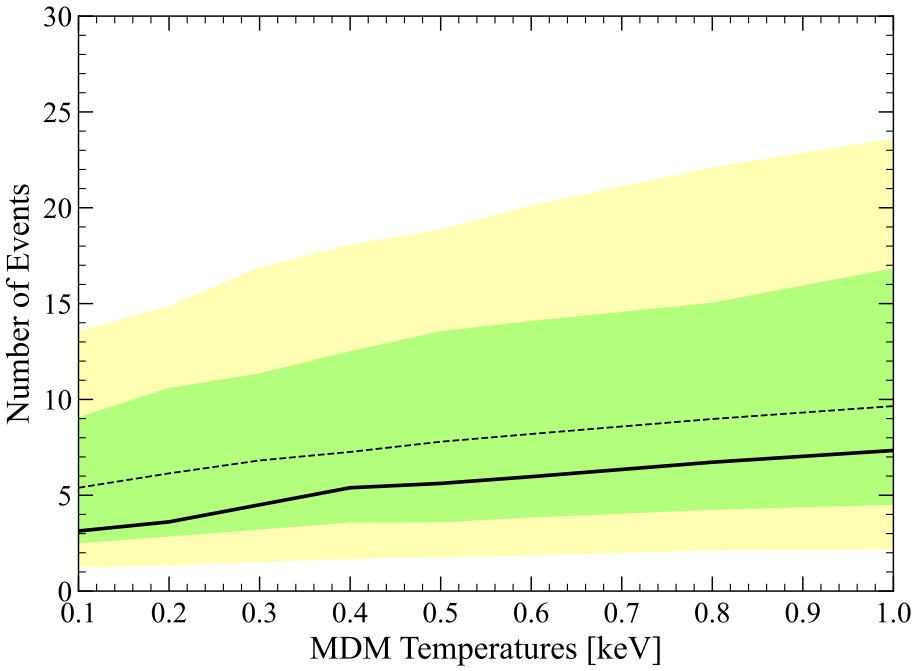

Figure 5.18 *The number of events at* 90% *confidence level for SR1 as a function of temperature in keV for mirror electrons. The solid black line shows the observed number of events, the dashed black line shows the median, and the brazil bands (green/yellow) represent the* $\pm 1(2)\sigma$ *of the number of events. The green band are the* ± 1 *band where the yellow bands are the* ± 2 *band.*

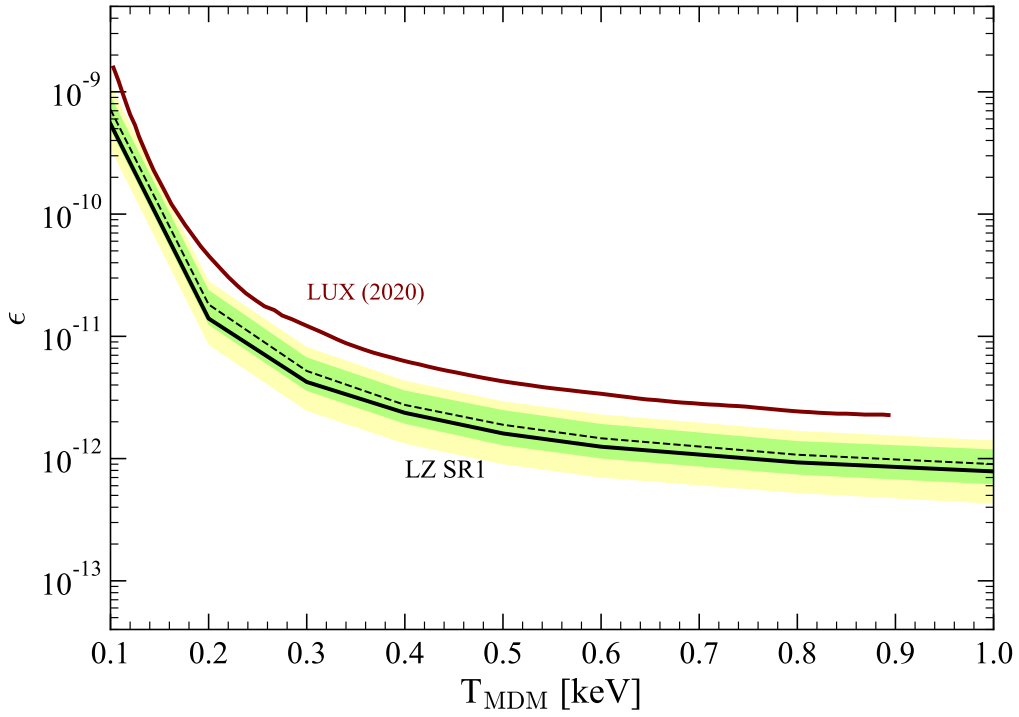

Figure 5.19 *The 90% C.L. upper limit (black line) on kinetic mixing ϵ as a function of mirror electron temperature T_{MDM}. Limit from LUX (brown) is shown in References [225].*

5.6 Conclusions for the Low-Energy ER Searches

Beyond the standard physics searches, an investigation was conducted in the low-energy electron recoil channel using the same 0.91 tonne×years exposure (SR1 data) and data selections as presented in the experiment's first WIMP results in Chapter 4.7 [226].

Following a period of calibrations and detector state optimisations, LZ is still gathering data. A recent finding for WIMP [227] that used a larger exposure of 4.2 ± 0.1 tonne years using 280 live days of data pushed the WIMP limits to the current leading limit. This included a technique to actively tag background electronic recoils from ^{214}Pb $\beta\beta$ decays for the first time. Subsequently, further analysis on low-energy ER signal models will also soon undergo full analysis, pushing the limits for all the previously featured signals in SR1 further.

Chapter 6

XIA alpha counters at Boulby

This chapter focuses on the XIA's UltraLo-1800 alpha counters that were added to the Boulby UnderGround Screening (BUGS) facility in 2018 to enhance its material screening capabilities for surface and bulk contamination. For this chapter, this author developed the Monte Carlo simulation for the UltraLo-1800 detector, which was used to improve the analysis and help differentiate between bulk and surface alpha emissions. The analysis for all the samples assayed using the UltraLo-1800 mentioned in this work was performed by this author unless stated otherwise. The content of this chapter has been published in this paper [2].

6.1 Motivation and context

6.1.1 Backgrounds in rare-event search experiments

The development of assay techniques is necessary to enable a thorough understanding of the radioactivity in materials. Particularly the entire uranium (U) and thorium (Th) decay chains due to the challenges arising from background caused by radioactive progeny contamination in materials used in the construction of the detector. The process of determining a material's radioactivity, whether intrinsic to the material or resulting from surface contamination, is often referred to as "material assay". Through careful material selection, cleaning, and assay, it is possible to reduce backgrounds and characterise residual radio-contaminants,

both of which result in improved detector sensitivity.

Neutron backgrounds are often extremely problematic in many low-background experiments, such as direct dark matter detectors and neutrinoless double beta-decay. For the latter, fast neutrons may produce a signal in the region of interest as they produce γ-rays that can generate such signals when they are captured on detector materials. Experiments like EXO include signals from neutron capture on ^{136}Xe, ^{1}H, ^{65}Cu, and ^{63}Xe as some of their dominant backgrounds [228]. On the other hand, in direct dark matter experiments such as LZ, which look for WIMPs, neutron-induced nuclear recoils inside the detector can mimic a WIMP signal, as previously discussed in Section 2.6.

Neutrons are considered cosmogenic in nature if they are produced via processes such as spallation when cosmogenic muons interact with the environment. Generally, cosmogenic neutrons are mitigated by building the detector deep underground, where the muon flux is greatly reduced. Radiogenic neutrons are the result of nuclear interactions within a given material, typically from (α,n) reactions induced by decays of radioisotopes from the naturally occurring uranium or thorium decay chains, which are embedded in the materials used in the construction of the detector. This background can be mitigated through careful material selection and characterised or tagged through material assaying and veto systems.

6.1.2 Decay chains

Focusing on the uranium and thorium decay chains, as shown in Figure 6.1, isotopes within these chains are expected to contribute the most significant backgrounds in low-background experiments. Secular equilibrium - where the amount of radioactive isotopes remains constant because the production rate matches the decay rate - is typically assumed for these chains. However, this equilibrium can be disrupted by the presence of long-lived gaseous isotopes that can emanate from materials, such as radon, an atmospheric gas ubiquitous on Earth. Materials can become contaminated as radon emanates after the manufacturing or selection processes, disrupting the equilibrium. As a result, assuming secular equilibrium for the entire decay chain may not always be accurate. Therefore, it is important to have a full understanding of the activities produced from different radioisotopes for the whole chains and expect that secular equilibrium is preserved with respect to the top of the sub-chain, starting from

radon.

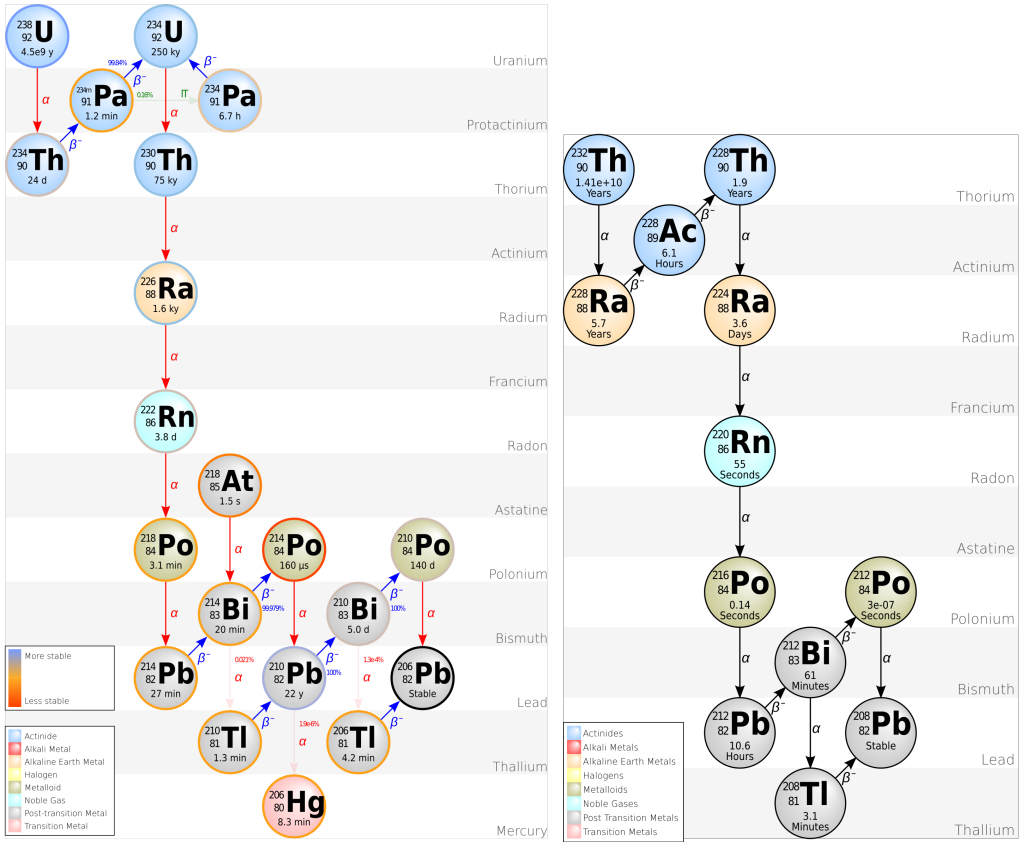

Figure 6.1 *The uranium-238 (left) [229] and thorium-232 [230] (right) decay chains with radon-222 daughters.*

Properties of radon

With an atomic number of 86, radon is a radioactive, colourless, and odourless noble gas. It is a naturally occurring atmospheric gas formed by the indirect decay of uranium and thorium and is found as a monatomic gas with only radioactive isotopes. The most abundant radioactive isotopes of radon are ^{222}Rn (named radon) and ^{220}Rn (called thoron), from the natural ^{238}U and ^{232}Th decay chains, respectively.

Out of the 36 radioactive isotopes of radon that have been reported, their atomic masses range from 193 to 228. Figure 6.1 displays the decay chains of thorium and uranium, which are the later decay chain from the decays of ^{226}Ra and ^{224}Th isotopes, respectively. As ^{226}Ra is practically everywhere in rocks and soils, this means that radon is ubiquitous in any construction material made from them.

As a noble gas, radon is inert, and combined with its relatively long half-life of

3.8 days (and 55 seconds in the thorium decay chain), it is difficult to physically seal against or remove chemically. This is a major challenge for all earth-bound low-background experiments that are sensitive to radon and its progeny decays. The diffusion length, L_i, of radon in a material is defined by:

$$L_i = \sqrt{\frac{D_i}{\lambda}}, \tag{6.1}$$

where D_i is the diffusion coefficient and λ is the decay constant. In addition to being highly diffusive, when the parent ^{226}Ra (from the uranium chain) decays by emitting an alpha particle, the resulting radon daughter recoils in the opposite direction to conserve momentum, with an initial energy of 86 keV. The distance that the recoiled radon can travel depends on the material, its density, and composition. Sme of these recoils, such as ^{210}Po recoils can pose a background for low-background experiments.

Radon concentrations are heavily dependent on location. Typically, the concentration of outdoor radon can range between 1 and 100 Bq/m^3, with an annual average estimated to be 10 Bq/m^3 [231]. Indoor radon concentrations can vary drastically, ranging from a few Bq/m^3 to more than 70 kBq/m^3, with an average of approximately 40 Bq/m^3 [232], depending on the location of the building, construction materials, and ventilation. In cleanrooms, the level of radon is usually reduced to less than 5 Bq/m^3 due to good ventilation and lack of exposed brickwork. In underground laboratories, the concentrations of radon activity depend on the surrounding rock content, ranging from a few kBq/m^3 in uranium mines to a few Bq/m^3 in salt mines [233].

Outside of physics, precise radon measurement is of significant interest to the general public due to health concerns. Once inhaled, radon decays into radioactive daughters that will subsequently decay inside the body, increasing the risk of developing cancer. Due to its abundance and tendency to accumulate in places with low ventilation such as basements, radon is one of the leading causes of lung cancer [234]. Thus, there are many commercial devices available to measure radon activity with sensitivities ranging from 0.1 Bq/m^3 to 1 MBq/m^3. However, current and next-generation rare-event search experiments require radon activity to be much lower than this sensitivity, necessitating custom-made detectors and designs to measure more precisely the concentrations of radon and its progeny contamination.

Radon progeny

The decay of radon produces electrically charged daughters which can "plate out" onto nearby surfaces [235]. Subsequent decays of surface deposits may cause the progeny to implant themselves to depths of several micrometres, embedding the radon progeny deeper into the materials and hindering removal and material selection efforts.

Several radon daughter isotopes, notably ^{210}Po (138.376 $\pm$ 0.002 days) and ^{210}Pb (22.20 $\pm$ 0.22 years), undergo alpha decays with relatively long half-lives [236]. If these isotopes are in the vicinity of instrument materials with large (α,n) cross-sections, such as ^{19}F found in the PTFE structure covering the LZ TPC, previously mentioned in Section 2.2, their subsequent alpha decay can produce neutrons within the detector [140].

Polonium-210 is a radon progeny in the uranium chain that decays to stable ^{206}Pb by emitting an alpha particle with energy of approximately 5.3 MeV and a branching ratio of nearly 100% [236]. Alpha particles from ^{210}Po decay have a typical range of several tens of μm in most solid materials, which becomes problematic if present in rare-event search materials, as it can lead to (α,n) reactions. The impact of this background on the experiment depends on the material in which the radon progeny (Po-210 isotopes) are embedded.

One of the more diverse applications of ^{210}Po has been the retrospective determination of atmospheric ^{222}Rn concentrations through the measurement of ^{210}Po deposited on surfaces [237]. This chapter focuses on measuring the concentrations of ^{210}Po on material surfaces and the use of Monte Carlo simulations to determine ^{210}Po bulk contamination in a material.

6.1.3 The neutron yield (α,n)

The focus here is on neutron yields produced by (α,n) processes, but it is also worth mentioning that neutron background can be generated through other processes such as spontaneous fission. The rate of these processes depends on the trace amounts of uranium and thorium present in each detector component, rather than contamination in the material itself. In the context of the LZ experiment, these sources are generally well-characterised due to comprehensive radio-assay and material selection efforts, using various screening techniques, as discussed in

Section 2.6. A schematic of the decay reactions from radon progeny plate-out undergoing (α,n) reactions with PTFE is shown in Figure 6.2.

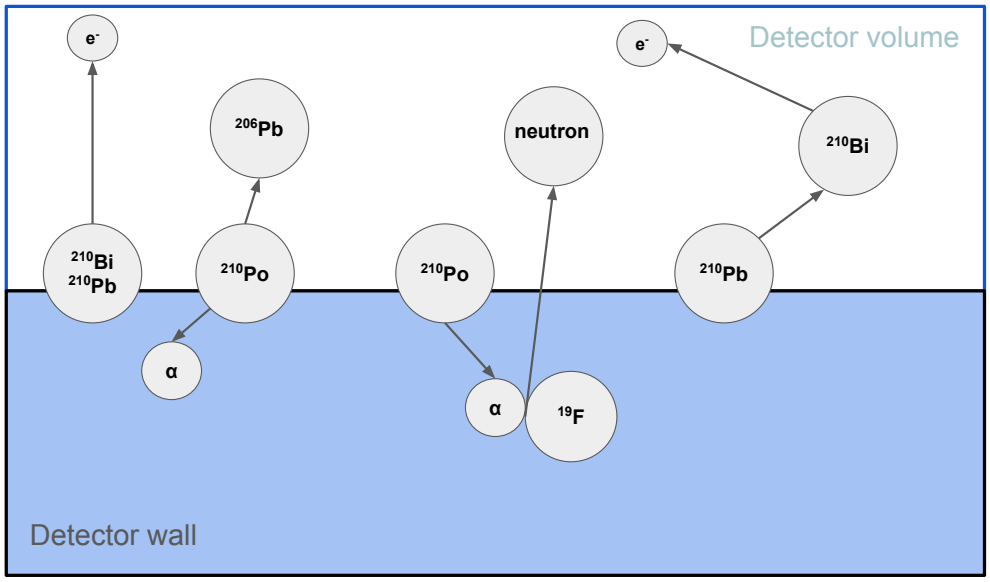

Figure 6.2 *Decay reactions of radon progeny leading to production of neutrons via (α,n) reactions with the ^{19}F in a rare event search detector.*

The neutron yield from the (α,n) reactions depends on the energy of the α-particle emitted, the material composition, the cross-section of the reaction, and the stopping power of alpha particles of a given energy in the material. Software like Neutron Calculator Based on TALYS (NeuCBOT) and SOURCES-4C have been developed and used to calculate the (α,n) yields of various materials [238]. However, the alpha energies and expected activity still need to be specified, and this becomes more complex when the radon progeny are embedded in the bulk of the materials, and alpha particles also lose energy as they travel through a material.

6.2 Radioassay facilities at Boulby Underground Laboratory

The UK's deep underground science facility, the Boulby Underground Laboratory (Figure 6.3), is located 1.1 km beneath the surface in the Boulby Mine, an active polyhalite and salt mine in North East England. Boulby is one of the few sites worldwide capable of supporting deep underground and ultra-low-background research programmes. It offers a unique location for scientific exploration, where

natural background radiation is virtually non-existent.

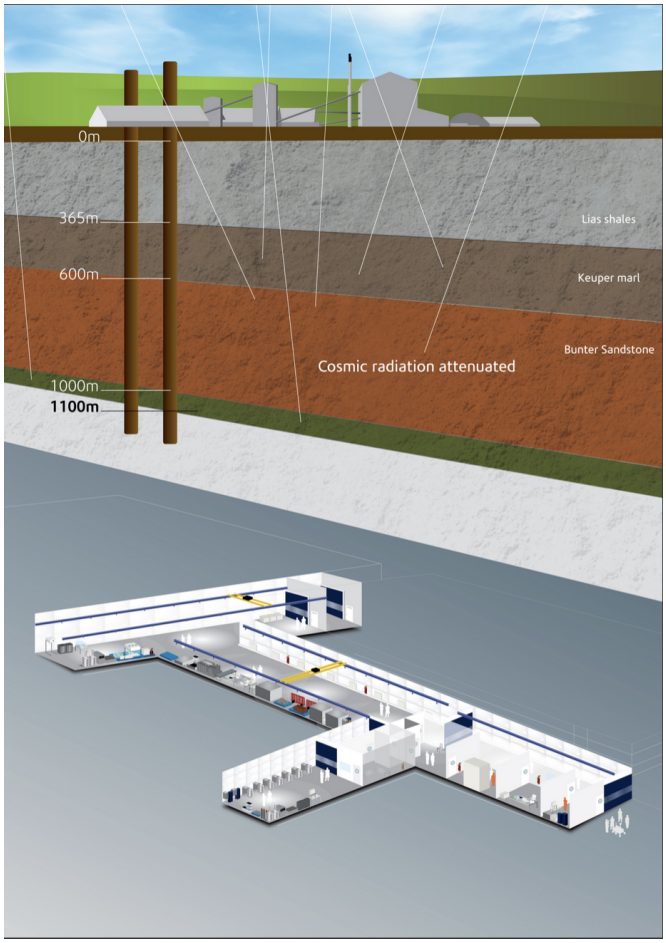

Figure 6.3 *A cross-sectional layout of the Boulby underground laboratory at the mine (not to scale).*

Since mining operations began in 1968, nearly 1,000 km of tunnels have been excavated at Boulby, creating an extensive network of underground roads and caverns. The mined salt and potash seams are remnants of the ancient Zechstein Sea, which evaporated around 250 million years ago. The primary access routes and long-lasting tunnels are carved through rock salt. With 1,100 m of rock above the Boulby Underground Laboratory, the cosmic ray flux is reduced by a factor of one million compared to surface levels. Combined with the low natural background radioactivity in the surrounding rock salt, Boulby provides an ideal environment for ultra-low-background and deep underground scientific projects, with a low atmospheric radon content of around 3 Bq/m^3 [239], which is 86% lower than the average radon level in UK homes.

The Boulby Laboratory hosts and supports numerous particle physics experiments, including those searching for dark matter and neutrinos, such as DRIFT

[240], ZEPLIN [241], NAIAD [242], CYGNUS [243], DM-Ice [244], and NEWS-G/Dark-Sphere R&D [245, 246]. It is also home to the Boulby Underground Screening (BUGS) facility, a world-class, ultra-low-background material assay laboratory that has provided material screening for LZ. For both current and next-generation low-background experiments, the ability to radio-assay materials with ever-increasing sensitivity is essential. BUGS played a critical role in supporting material assays for LZ [138] and other rare-event search experiments, and it remains vital for future dark matter and other low-background studies.

In these experiments, intrinsic radioactivity in the materials used to construct the detectors is a primary source of background radiation. This background can be reduced to the levels necessary to meet the experiment's scientific goals through a comprehensive material radio-assay programme, involving meticulous material selection and cleaning. It is crucial that the experiment's background model is precisely characterised to account for any residual activity, allowing any observed excess to be accurately evaluated as a potential signal.

The Boulby Underground Laboratory consists of more than 4,000 m^3 of clean lab space, 3,000 m^3 of outside space, along with class 1000 and 10,000 cleanrooms. BUG facility has been operating since 2015 as an ultra-low background screening facility [247]. BUGS is one of the few underground low-background material assay facilities in the world, alongside SNOLAB [248], Laboratori Nazionali del Gran Sasso (LNGS) [249], Sanford Underground Research Facility (SURF) [250], Laboratoire Souterrain de Modane (LSM) [251], Laboratorio Subterraneo de Canfranc (LSC) [252], and Kamioka Observatory [253].

The BUGS facility currently consists of six high purity germanium (HPGe) detectors, a dual-detector radon emanation system, an Agilent-8900 Inductively Coupled Plasma Mass Spectrometer (ICP-MS), and two XIA surface alpha counters [254].

At the BUGS facility, radioactive assay techniques are divided into two types: destructive and non-destructive techniques. Destructive techniques, such as ICP-MS, involve dissolving or digesting the materials, meaning they cannot be used to construct the experiment. These techniques allow the direct measurement of long-lived uranium and thorium concentrations in a material but are not effective in determining the concentration of the radioisotopes lower in the decay chain with shorter half-lives. Non-destructive techniques include gamma-ray spectrometry using the HPGe detectors, radon emanation studies, and surface alpha counting

using the UltraLo-1800 detectors. These techniques are used to study the isotopes lower in the decay chain, where either gamma or alpha particle emission is measurable depending on the technique. Combining all the techniques allows for a more thorough understanding of the activities due to different radioisotopes in the uranium and thorium chains, and helps to identify breaks in equilibrium, which is not achievable through mass spectrometry alone.

6.2.1 Alpha screening using the UltraLo-1800

Schematic of the UltraLo-1800 alpha counter

The UltraLo-1800 is an alpha particle counter manufactured by XIA LLC [255] that employs a dual-channel pulse shape analysis technique. This method allows the alpha counter to distinguish between particles originating from the assayed sample and those emitted by the detector components, unlike traditional proportional alpha counters, as shown in Figure 6.4.

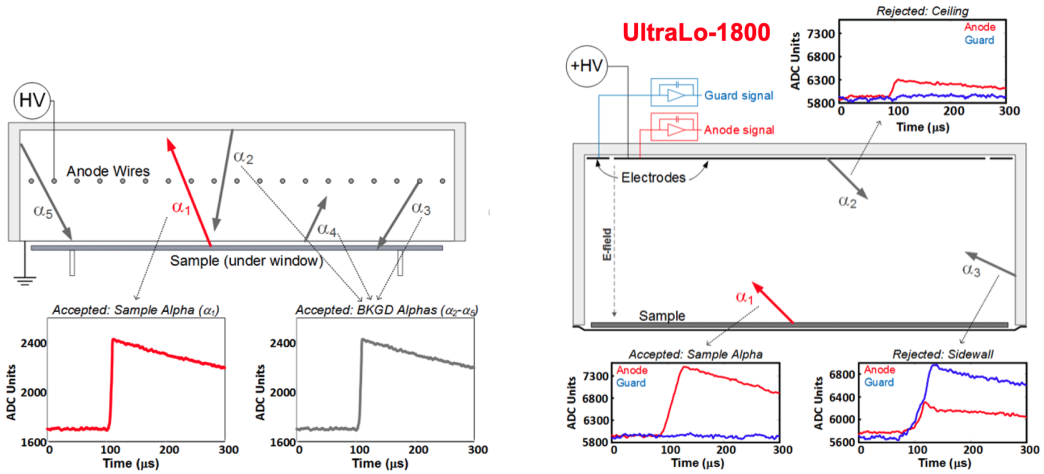

Figure 6.4 *Contrast between a conventional proportional counter (left) and the XIA UltraLo-1800 (right) in terms of alpha signal and background detection, Figure taken from [255].*

The active volume of the UltraLo-1800 is filled with high-purity argon gas and is separated by two conductive plates at a variable distance D (in a possible range x to y) apart. The top plate consists of a pair of positively charged electrodes: the anode, placed directly above the sample, and the guard, which surrounds and encloses the anode. Both electrodes are connected to charge-integrating preamplifiers, where the output signals are digitised and processed using a digital pulse shape analyser. The top plate is held at a voltage V, while the bottom

plate, also known as the sample tray, is held at ground potential. The potential difference between the two plates produces an electric field, E, across the active volume with a field strength of V/D. A picture showing a generic XIA counter is shown in Figure 6.5.

Figure 6.5 *A photograph of a generic UltraLo-1800 alpha counter taken from [255]*

When a radioactive isotope on the sample tray decays, the emitted alpha particle creates an ionisation track of argon ions and electrons. The electric field across the active volume causes the electrons to move upward, inducing a time-varying charge on the anode that is registered as current by the preamplifier. The extracted current is integrated to produce an output pulse, which is then digitised and analysed to extract its risetime, amplitude, and shape.

6.2.2 Signal generation

When a radioactive isotope on the sample decays and emits an alpha particle in a random direction, the particle leaves the atom and is stopped in the counting argon gas after traveling a certain distance. This distance, d, traveled by the emitted alpha particle is dependent on its energy and the gas species, which in this case is argon. As the alpha particle moves through the gas, it loses energy by ionising the gas molecules, producing a track of N ion-electron pairs. The applied electric field drifts the electrons towards the positive electrode and the

ions towards the tray.

The velocity of each drift with respect to its mobility μ in the gas can be written as:

$$v_e = E \cdot \mu_e = V \cdot \frac{\mu_e}{D}, \tag{6.2}$$

where the subscript $(_e)$ indicates electron. The mobility of electrons is thousands of times higher than that of ions, so electrons drift to the electrode much faster than ions drift to the tray. The drift time for an electron freed from a distance d from the top electrode is simply $t_e = d \cdot \frac{D}{V} \cdot \mu_e$.

All the electrons in the track are assumed to have the same drift velocity[1] so the initial geometry is preserved from t_0 until the first electron reaches the electrode at t_s, and until all the electrons are absorbed by the electrode at t_r. Using Gauss's Law, the net electric flux through any closed surface is proportional to the enclosed electric charge. This implies that any changes in flux correspond to changes in the present charges, and therefore the current in the circuitry connected to the electrode is proportional to the rate of change of the flux. As described by the Shockley-Ramo theorem [256], as the electrons drift towards the electrode, they induce a current in the attached electronics. This induction only occurs while the electron is in motion; once it reaches the electrode, its electric field disappears, the changing flux goes to zero, and consequently, the induced current goes to zero.

An emitted alpha particle from a detector component, such as the anode or the sidewall, still produces an ionisation track of argon ions and electrons. However, the UltraLo-1800 is designed such that the output pulses associated with these non-sample alphas have different risetimes, amplitudes, and shapes, allowing the built-in analysis software to veto these events.

Figure 6.6 shows the digitised signal produced when an alpha event emitted from the assayed sample is recorded. Some electrons in the track will induce the current for longer than others, and once the track begins to reach the electrode, at time t_s, the rate of induction starts to slow down. The rate at which induction slows is proportional to the angle of the track relative to the electrode. This slowing is shown as a rounding in the pulse from t_s to t_r, as illustrated in Figure 6.7.

Hence, for a track originating from an alpha particle emitted from the sample

[1]The electron drift speed is assumed to be uniform and known for the counting gas used, which in this case is argon. The counting gas must also be pure, as a concentration of water as low as 100 ppm can drastically increase risetimes.

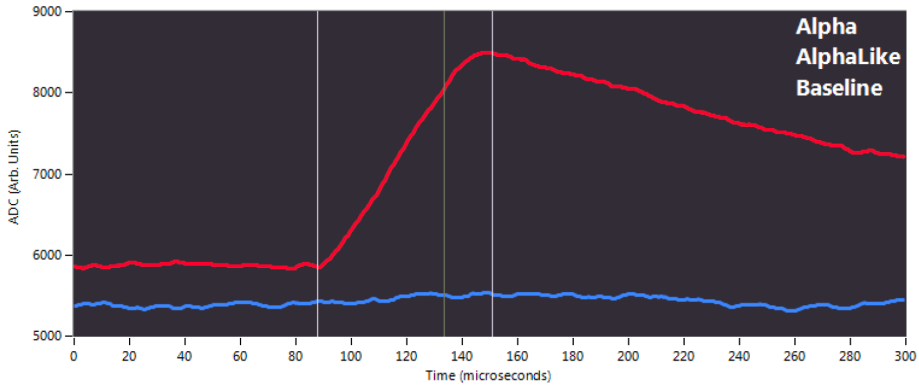

Figure 6.6 *Example of an alpha event emitted from the sample assayed. The red line represents the anode and the blue line represents the guard. The three vertical lines represent the key times in the drift of the produced electrons, from left to right: t_0, t_s, and t_r. This plot is taken from [255].*

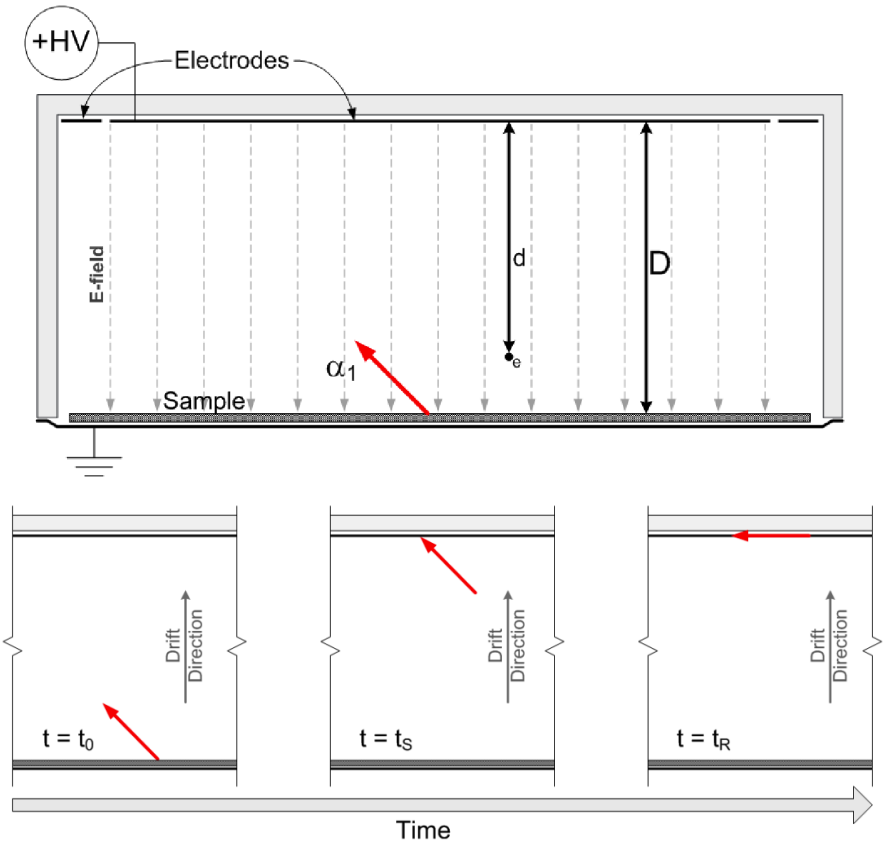

Figure 6.7 *Schematic showing the UltraLo-1800's active volume with an arbitrary alpha particle α_1 emitted from a sample (top) and the location of the electron track produced by the emitted alpha at the three key times: t_0, t_s, and t_r. These plots are taken from the manual [255].*

(α_1), as shown on the right of Figure 6.4, there are two distinct regions marked by the key times of the track, as highlighted by the vertical lines in Figure 6.6. One region is between t_0 and t_s, where the electron drift is linear, and the other is between t_s and t_r, where the slowing begins, and the electrons are disappearing linearly in time which gives the shape of a parabolic. Thus, we can write the resultant integrated signal as $S(t)$ for the two regions in terms of the detector capacitance C_f as following:

$$S(t) = \frac{Ne\mu_e V}{C_f D^2}\left(t - t_0\right), \tag{6.3}$$

for t_0 to t_s. Then for t_s to t_r:

$$S(t) = \frac{Ne\mu_e V}{C_f D^2}\left(t - \frac{(t - t_s)^2}{2\left(t_r - t_s\right)}\right). \tag{6.4}$$

Where we defined the terms that define the key times in the drift of the produced electrons as:

$$t_s = \frac{d_s D}{\mu_e V}, \tag{6.5}$$

$$t_r = \frac{D^2}{\mu_e V}. \tag{6.6}$$

$$S_{MAX} = \frac{Ne}{2C_f}(1 + \frac{d_s}{D}), \tag{6.7}$$

where d_s is the distance between the topmost electron in the track to the electrode. Note that S_{MAX} scales with N so final pulse amplitude is proportional to the energy of the alpha particle.

The classification mechanism

The UltraLo-1800 is an ionisation counter, and typically, the most common type of alpha counters available are proportional counters, as depicted in Figure 6.4. Both counters are filled with inert gas and utilise the drift of electron-ion pairs produced by emitted alpha particles to generate signals when these are collected by the electrodes.

The main physical difference between the two types of alpha counters is the strength of the electric field. Ionisation counters require the electric field to be fairly low and uniform, while gas proportional counters have stronger fields

to create electron avalanches. An electron avalanche is generated through a process called gas multiplication, where the electrons produced by ionisation are accelerated to create more electron-ion pairs, resulting in an "avalanche" of electrons. To induce this gas multiplication, a proportional counter has an anode composed of thin wires to create a "multiplication region" of high electric field close to the wire.

The advantage of this higher electric field is that proportional counters generally have a large internal gain, producing larger signals that are easier to process. However, this comes with increased electronic noise and, more importantly, proportional counters lose the ability to determine the location of the emission site.

In general, ionisation counters like the UltraLo-1800 are favoured for low-rate, large-area alpha counting due to their ability to differentiate the origin of the particle track. Further details on how the UltraLo-1800 classifies different alpha events based on the location of emission, using the risetimes and amplitude of the generated pulses, are presented using Figure 6.8 and Table 6.1.

Background sources in the UltraLo-1800

Although the UltraLo-1800 is capable of differentiating alpha tracks originating from its internal surfaces, there are several known sources that can induce signals mimicking those emitted from a sample. In general, these sources are expected to contribute a background rate of 0.0005 counts/hr/cm^2 in the alpha counter at sea level, with no significant overhead shielding. High-energy cosmic ray particles also induce background through several mechanisms: directly interacting with detector materials, producing secondary particles, or activating detector materials via nuclear reactions. However, when operated deep underground at the BUGS facility, cosmic background fluxes are reduced by a factor of one million compared to surface levels. This makes the Boulby Underground Laboratory an ideal location for hosting material screening campaigns for other rare event searches.

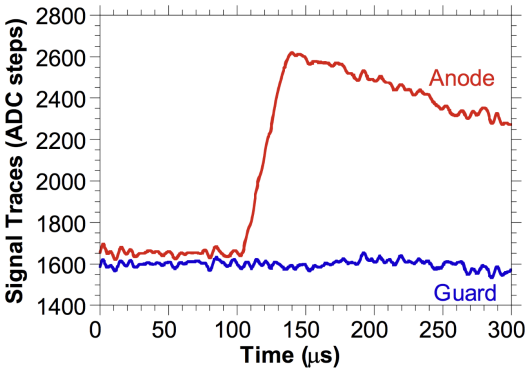

(a) *Alpha emitted from the sample.*

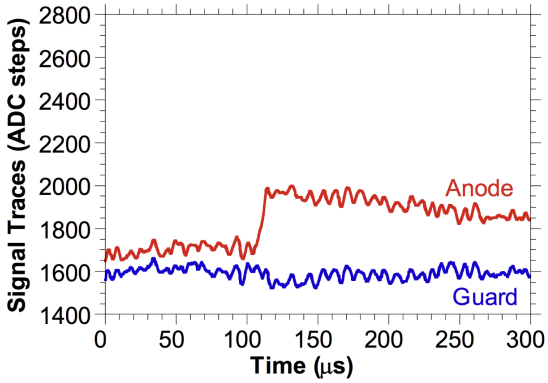

(b) *Alpha emitted from the ceiling.*

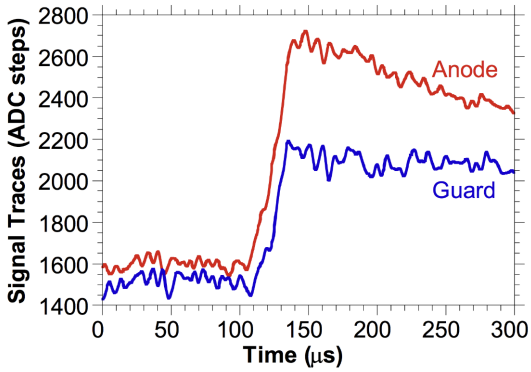

(c) *Alpha emitted from the edge of the sample*

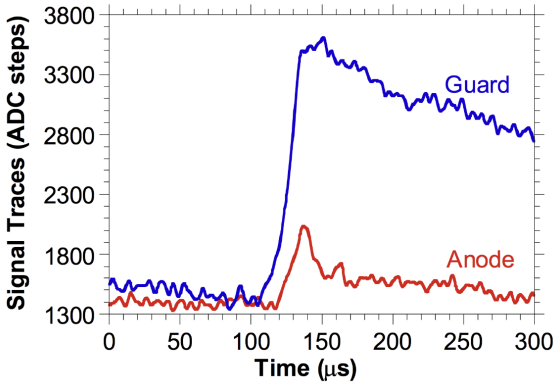

(d) *Alpha emitted from the sidewall.*

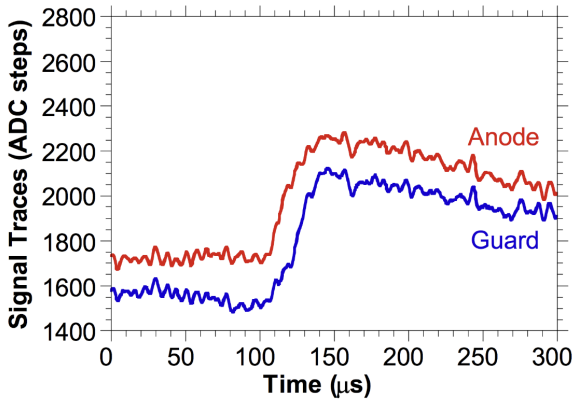

(e) *Another alpha emitted from the sidewall.*

Figure 6.8 *The reconstructed anode (red) and guard (blue) pulses for different alphas originating from different locations in the counter. Table 6.1 provides further details on the features of each plot. The plots were produced by LZ collaborator XinRan Liu.*

Table 6.1 *Different types of classified alpha events are based on the location of the emission inside the UltraLo-1800 alpha counter. Figure 6.8 shows the common anode and guard pulse outputs associated with each type of alpha emission.*

Label	Origin	Feature
6.8a	Sample	The anode pulse is linear at first and becomes parabolic until the all the electrons in the track is absorbed by the electrode.
6.8b	Electrode/ ceiling	For a track originating from the electrode, both the risetimes and maximum amplitude are much shorter than the sample alpha pulse. This is due to the ratio of the the two alphas' risetimes is given by $\frac{sample}{electrode} = \frac{D}{d_a}$. In this case, d_a is the track length normal to the electrode for the track originating from the electrode. The main difference between a sample and ceiling alphas would be the anode pulse (red) for ceiling alpha would have a smaller amplitude due to smaller risetime.
6.8c, 6.8d & 6.8e	Sidewalls and near the boundary of the electrode/- guard	Tracks originating from the sidewalls or near the boundary of the electrode (including alphas emitted from the sample) would induce pulses on the guard (blue) and can be vetoed by the UltraLo-1800 event classifier. This results in the UltraLo-1800 has a counting efficiency that decreases with higher alpha energies, since higher energy alphas have longer track lengths, and longer track lengths are more likely to cross over to the guard.

6.3 Simulation

To better understand the detector's response to various materials, assess its counting efficiency, and improve the contamination analysis for both surface and bulk emissions from samples, a Geant4 simulation was developed for this alpha counter. The Geant4 version 10.5.1 [257] simulation includes libraries such as G4EmStandardPhysics, PhysListEmPenelope, and PhysListEmLivermore to model electromagnetic processes, while G4HadronElasticPhysicsHP was used to model hadronic interactions. The geometry of the UltraLo-1800 alpha counter, as described in Section 6.2.1, was implemented in the simulation, incorporating all physical aspects such as the argon active volume and electric field.

The sample sources were modelled using G4GeneralParticleSource, which allows

the user to define different macros to specify the sample's shape, material, dimensions, and the manner in which the alpha particles are emitted. The energy resolutions were modelled using Gaussian distributions, with the standard deviations derived from the full width at half maximum (FWHM) obtained by fitting energy peaks in the calibration data. Calibration was performed using ^{210}Po (5.3 MeV) and spectroscopic-grade ^{230}Th (4.6 MeV) sources.

6.4 Analysis and results

6.4.1 Calibration and energy reconstruction

To ensure that the energy reconstruction and resolution of the two detectors are accurate and stable over time, the Boulby UltraLo-1800 alpha counters are routinely calibrated using a custom-made ^{210}Po alpha particle source provided by Spectrum Techniques [258]. This source is suitable for energy calibration but is too "hot" for rate calibration.

Figure 6.9 presents the Monte Carlo simulation for the UltraLo-1800 alpha counter alongside a set of calibration data. Since the UltraLo measures the energy deposited in the gas, unless the alpha emission occurs directly at the surface of the sample, there will be some self-absorption, leading to "tails" in the energy spectra. These tails affect the Gaussian fits and resolution computations.

It is accurate to state that the energy resolution decreases at lower energies, as the signal-to-noise ratio decreases accordingly. Following this, we observe slightly better resolution at higher energies, where the signal-to-noise ratio improves. To model the energy resolution in Geant4, a linear variation from low to high energies (1-10 MeV), passing through the known resolutions at 4.6 MeV (^{230}Th) and 5.3 MeV (^{210}Po), is implemented to improve the model. Another factor influencing noise is the detector's capacitance, which depends on whether it operates in the 707 cm^2 wafer mode or the 1800 cm^2 "full" mode. These modes correspond to different electrode sizes, which affect the detector's counting efficiency. For a 6 MeV alpha particle, the overall efficiency is approximately 85% in wafer mode and about 90% in full mode.

The energy resolution and reconstructed alpha particle energies showed stability over three years of regular calibrations using the ^{210}Po source. The centroid of

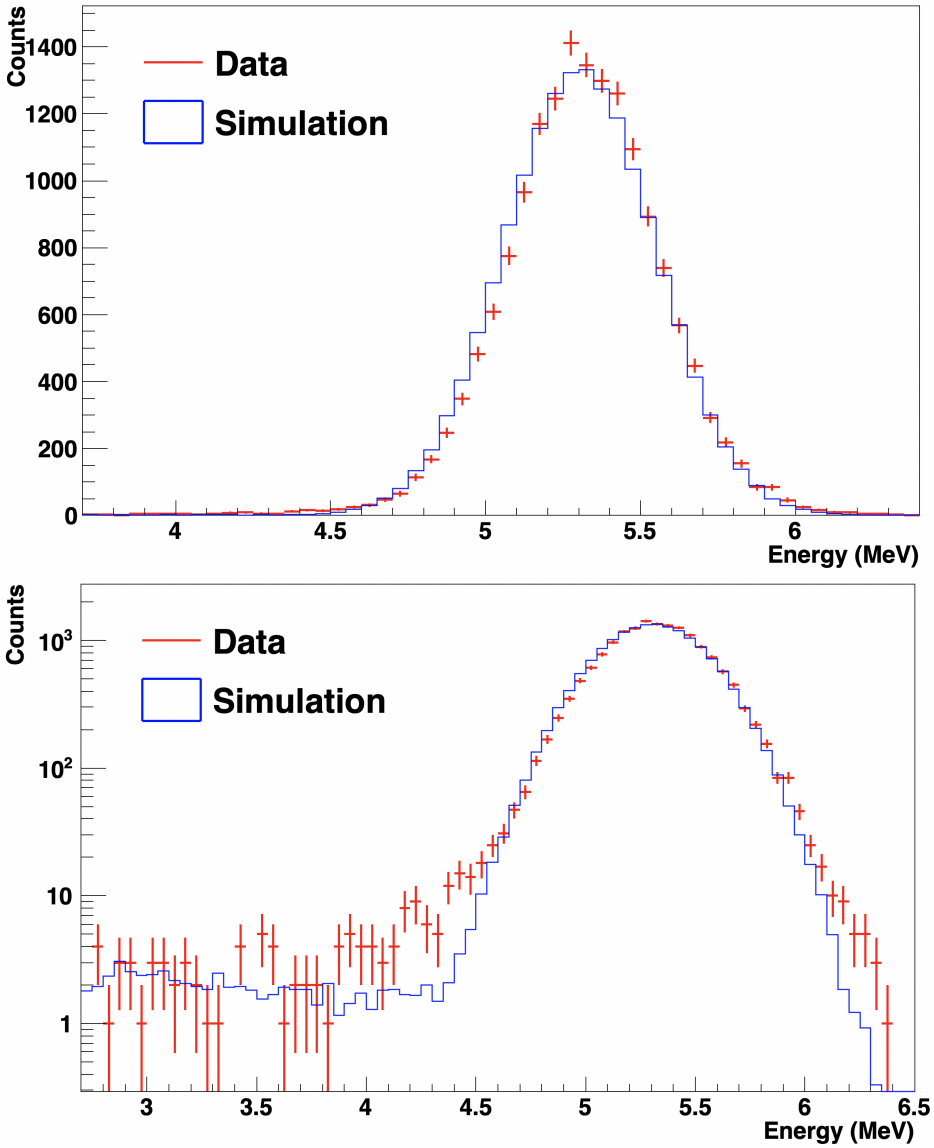

Figure 6.9 *Calibration spectra from a ^{210}Po source on the UltraLo-1800 detector. Data (red) and simulation (blue) are illustrated with linear (top) and logarithmic (bottom) scales.*

the reconstructed energy showed a change in value of less than 0.1 MeV while the energy resolution retained consistently around 0.57 MeV FWHM for a 5.3 MeV alpha source.

A ^{220}Th source is also employed to extend a previous study [259] producing alphas of energies 4.62 MeV (23%) and 4.69 MeV (76%) [260]. This allows the analysis at lower alpha energies to be conducted and also produced a low-energy tail in the energy spectra.

6.4.2 Background measurements

The sample tray is a crucial component of the detector as it holds the material being assayed and determines the sensitive area exposed to the detector. In general, for any sample being assayed by the UltraLo-1800 counter, unless the sample fully covers the surface area of the tray, the energy spectrum of the assay will also include alpha events emitted from the tray in addition to those from the sample. Given that the sample tray's inherent background may affect the assayed sample's energy spectrum, it is essential to fully understand it.

We obtained background measurements for a manufacturer-provided stainless steel tray (left) and a tray made from a 0.05 mm thick sheet of conductive-graphite-filled PTFE (right), as shown in Figure 6.10. As illustrated in Figure 6.11, it was found that the alpha background from the stainless steel sample tray can be significantly reduced by using a highly radio-pure liner positioned on top of the tray. The PTFE liner, made from a 0.05 mm thick sheet of graphite-filled PTFE by DeWAL [261], is shown on the right of Figure 6.10, placed over the stainless steel tray.

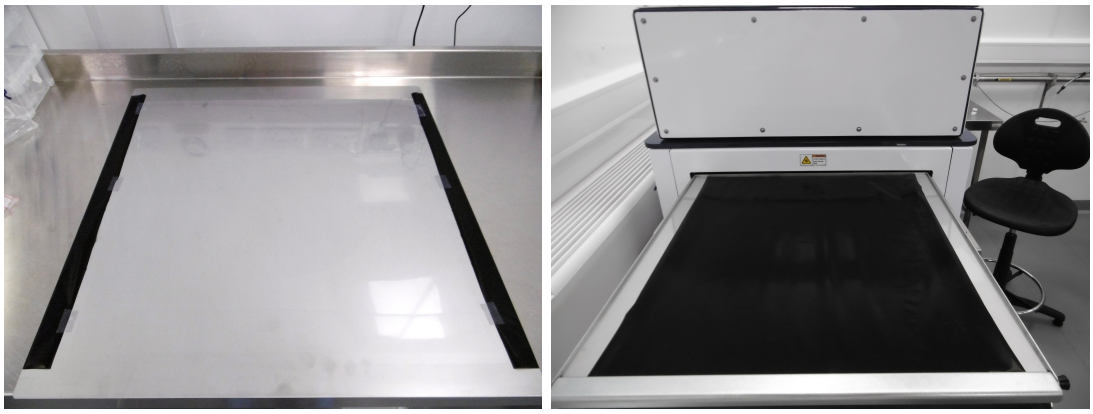

Figure 6.10 *Photographs of the UltraLo-1800 stainless steel sample tray (left) only and with the PTFE-graphite liner (right) installed.*

From multiple measurements, presented in Figure 6.11, the average activities are $1.28 \pm 0.03\ \alpha/\mathrm{cm}^2/\mathrm{khr}$ for the stainless steel (SS) tray and $0.14 \pm 0.01\ \alpha/\mathrm{cm}^2/\mathrm{khr}$ for the PTFE-lined tray. The result for the stainless steel tray is consistent with results from other facilities that also use the UltraLo-1800 [262–264].

Different research groups have adopted various purge periods for the UltraLo-1800, ranging from as short as 1 hour [259] to a full day [264]. At Boulby, a 48-hour purge period following sample assays is implemented. This extended

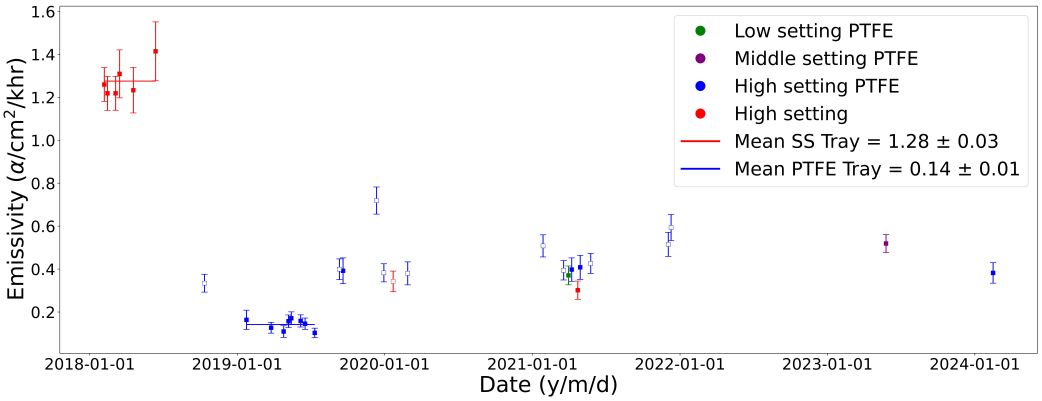

Figure 6.11 *Long-term background investigation for various tray configurations for the UltraLo-1800 detector. The measuring period was roughly six years long, from 2018 to 2024. The filled blue data points indicate the decrease in activity after a graphite-filled PTFE liner was placed into the tray, while the filled red data points depict the activity during the first operation utilising the stainless steel (SS) tray. The measurements taken immediately after the sample tests are represented by the unfilled blue data points. This suggests that a purging interval is necessary for the graphite-filled PTFE tray to return to its low background configuration.*

period allows for the thorough removal of potential contaminants and ensures the detector returns to a stable background before further measurements. The consistent stability in our long-term background data supports the effectiveness of this approach. While a systematic study of purge times could provide additional insights into optimizing this process, it lies beyond the scope of this work and may be explored in future studies.

6.4.3 Bulk and surface measurements

Materials exposed to radon-contaminated environments experience surface plate-out [265]. The primary source of alpha-particle emission from high-purity material surfaces in such environments is ^{210}Po, due to the accumulation of radon progeny over the material's lifetime. Another important progeny is ^{210}Pb, a radionuclide with a relatively long half-life of 22.3 years, which decays almost exclusively via beta emission [266]. Naturally, unless exceptional care has been taken, most detector components will contain ^{210}Po mixed into the bulk during production and manufacturing. In this context, "bulk" refers to the internal substance of the material.

Typically, when a sample is assayed, the energy spectrum reveals two primary components of contamination, as shown in Figure 6.12: the 5.3 MeV alpha particles emitted by surface-deposited ^{210}Po (surface alphas), and lower-energy alpha particles emitted from ^{210}Po embedded within the bulk of a copper sheet (bulk alphas). Figure 6.13 shows the tracks of alpha particles simulated using the Geant4 visualisation software, OpenGL. From this figure, it is evident that alpha particles emitted from within the bulk travel only a short distance before losing all their energy, unlike those emitted from the surface, which travel farther. As a result, most bulk alphas would not be detected by the XIA alpha counter.

Bulk alpha particles lose some of their original energy as they traverse through the material toward the surface. Depending on the material and the initial energy of the emitted alpha particle, bulk alphas can escape from depths of up to several tens of micrometres in certain solids. Generally, the main peak in the alpha energy spectrum arises from alpha emissions at or near the surface, with a broad tail of events extending to lower energies, as shown by the "sum" black line in Figure 6.12. The cut-off threshold in this simulation is set to around 1.5 MeV, based on the quoted value from the manual [255]. At 2.5 MeV, the efficiency is approximately 0.5; however, in reality, the cut-off threshold of the alpha counter varies between individual counters, as it depends on the anode trigger threshold.

To understand the efficiency[2] of the detector detecting ^{210}Po bulk alphas in different materials, these behaviours are explored using Geant4. Various methods were employed to study the emission from within the bulk, one is to simulat ing

[2]Here, efficiency is defined as the fraction of ^{210}Po alpha particles that are detected by the XIA alpha counter in the simulation—accounting for the coded detector response and threshold—out of all the simulated alpha events.

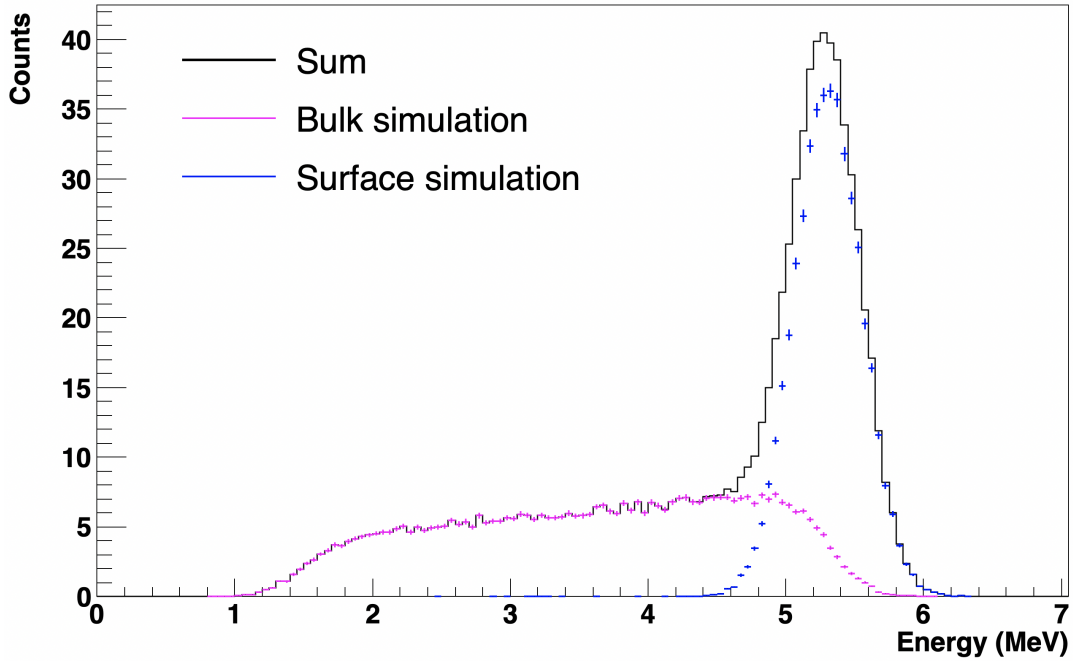

Figure 6.12 *Spectra illustrating simulations of energy depositions from surface and bulk ^{210}Po alpha particles in titanium. Pink represents the how the emissions of ^{210}Po alpha particles in the "bulk" deposited energies while blue shows the energy depositions of ^{210}Po alphas emitted from the surface. The sum of the surface and bulk ^{210}Po alpha particles are the solid black line.*

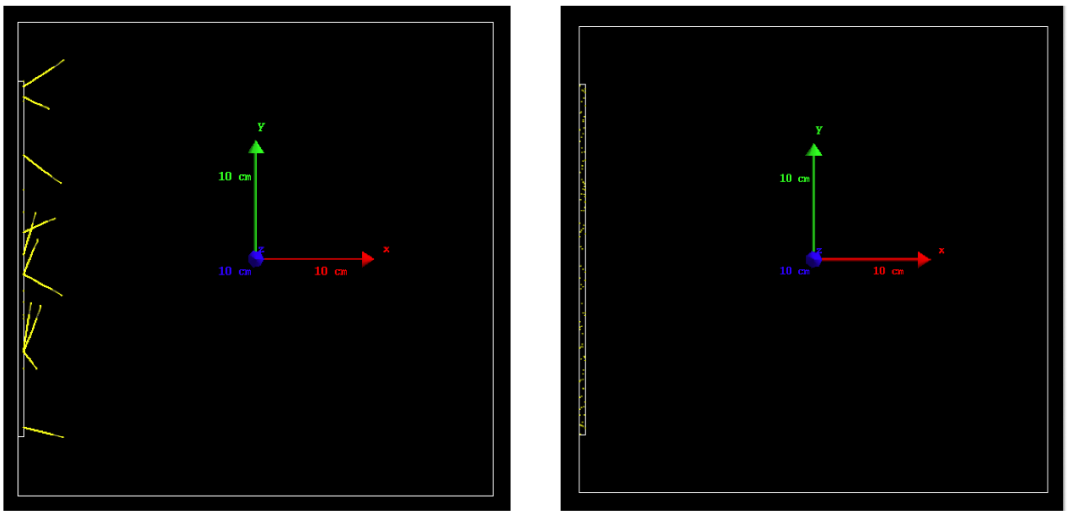

Figure 6.13 *Geant4 simulations modelling alpha emissions from the surface plane of a sample (left) and alpha emission from a sample volume (right). The yellow lines represent the tracks of the emitted alpha particles in each simulation.*

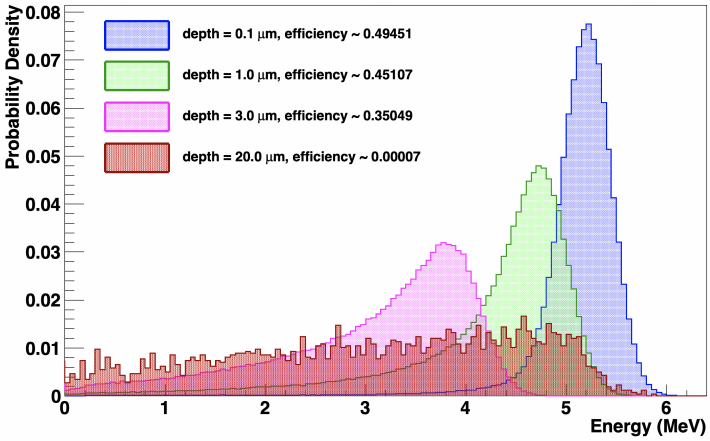

(a) *Copper*

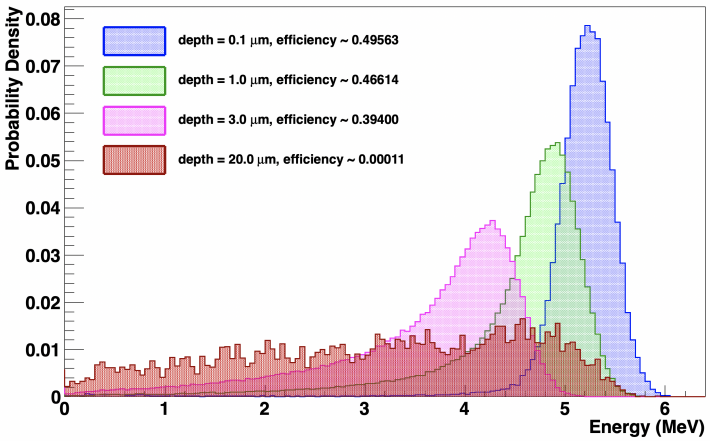

(b) *Lead*

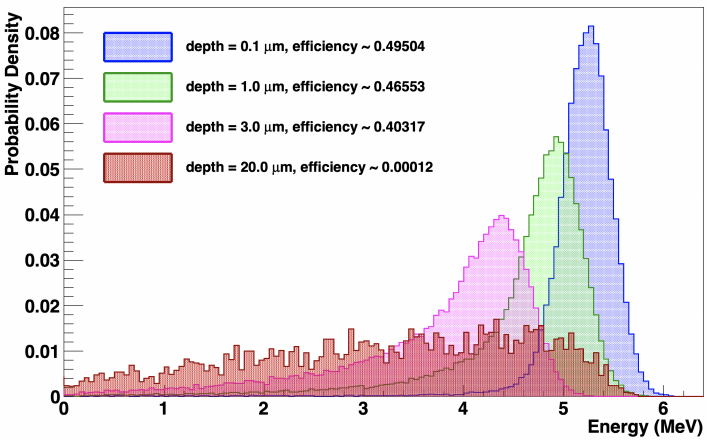

(c) *Titanium*

Figure 6.14 *Simulated depth profiles of ^{210}Po alpha emissions in Cu, Pb, and Ti (from top to bottom). These simulations show the energy spectra and corresponding yields of alpha particles emitted at various depths in three materials commonly used in particle physics. Here, the efficiency refers to the fraction of ^{210}Po alphas that are detected by the XIA alpha counter, out of all those simulated at a given depth.*

the energy spectra and efficiencies for ^{210}Po alphas emitted at different depths in some materials, shown in Figure 6.14. Another way is by simulating the alpha particles emitted at different layers of sequentially increasing depth, the efficiencies of the detectable ^{210}Po alphas are presented in Figure 6.15 for copper and titanium.

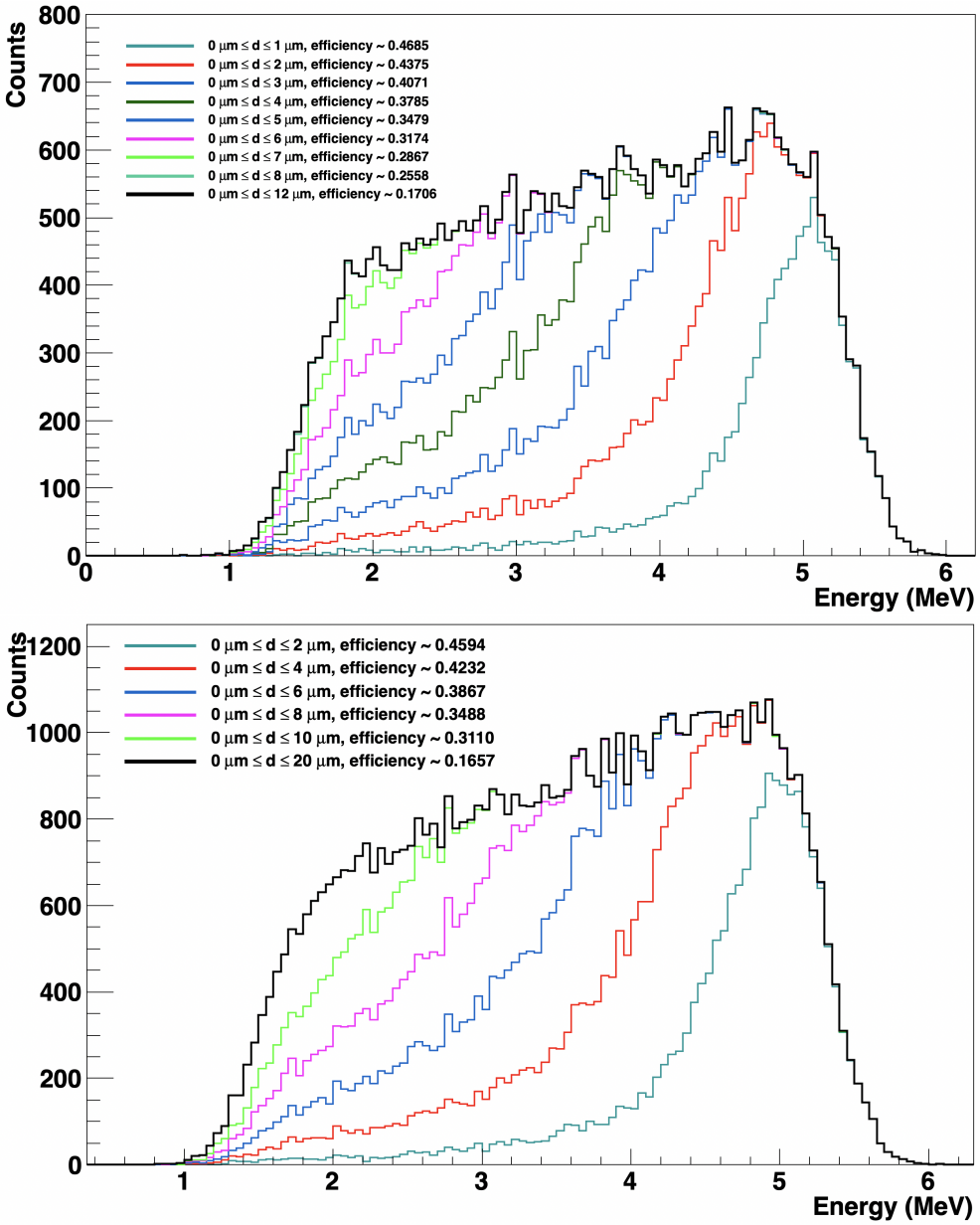

Figure 6.15 *Detected alpha particle energy spectra from simulation of 10^5 ^{210}Po decays in successive 1 μm thick slices of copper (top) and titanium (bottom). The efficiency quoted for each label in these figures is defined as the fraction of ^{210}Po alphas that are detected by the XIA alpha counter, out of all those simulated.*

In contrast, decays of ^{210}Po embedded on the surface of the material generate a

Gaussian distribution centered around 5.3 MeV, smeared due to the detector's resolution at this energy. The black curve represents the overall shape expected if we were to assay a copper sample contaminated with ^{210}Po radionuclides in 6.12.

Fittings of radon progeny contaminants

Data from a titanium tray was used to study radon progeny "plate-out" onto surfaces and in bulk. This titanium tray was assayed using the UltraLo-1800 for 138 hours, with the results binned as the lilac histogram in Figure 6.16. For a relatively long assay duration like this, additional alpha particles from the radon decay chains, such as ^{218}Po (6.0 MeV), ^{212}Po (6.05 MeV), ^{216}Po (6.78 MeV), ^{214}Po (7.69 MeV), and ^{212}Po (6.78 MeV), were observed. Since these radon progeny also contribute to the overall alpha spectrum, simulations of their contamination were added and fitted to the data, including contamination from ^{210}Po (5.3 MeV).

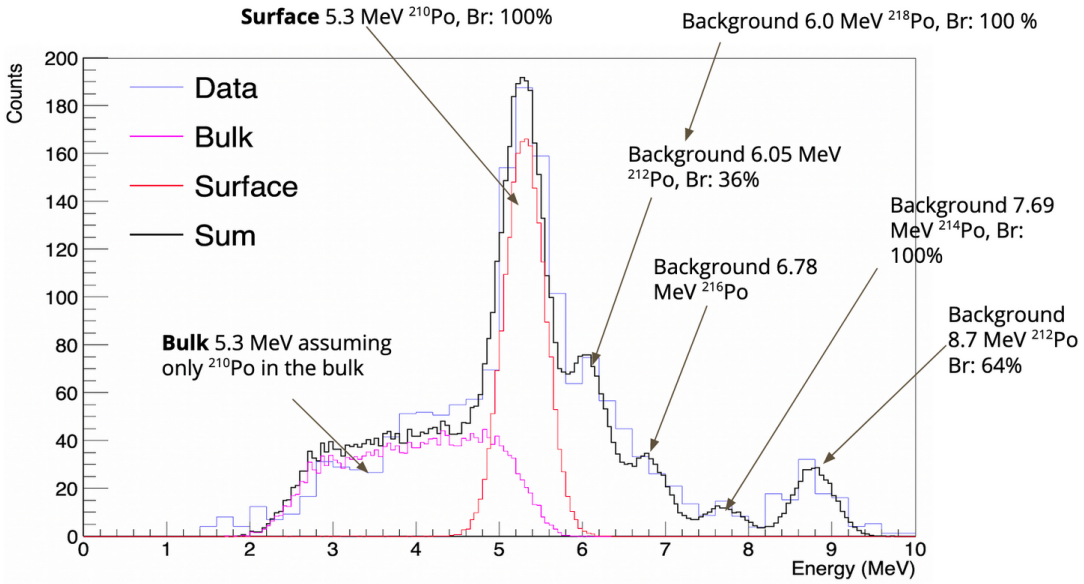

Figure 6.16 *A titanium tray was assayed using the XIA alpha counter for over 138 hours. The lilac line represents the data, while the pink and red lines are the simulated, normalised, and scaled bulk and surface energy spectra, assuming only ^{210}Po decays in the titanium sheet. The black line is the sum of the pink, red, and other simulated decays from α-emitting radon progenies, with energy spectra scaled to the same number of events as the data, to compare the fit with the titanium assay data. "Br" is shortened for the branching ratio of the labelled decay.*

The black line represents the sum of all the simulated radon progeny contaminants, fitted and scaled to match the total number of alpha events detected by

the UltraLo-1800. The overall fit was performed by fitting multiple polynomials to each individual component. Gaussian functions were used to model the "monoenergetic" peaks of detected surface alpha particles from decays of various radon progenies, whereas the energy deposition of the bulk alphas was fitted using a third-order polynomial, with the range defined from 2.5 MeV to 4.6 MeV. It was noted that a fourth-order polynomial resulted in overfitting, while a second-order polynomial underfitted the data. The simulation for each contaminant was then scaled according to the fits and the total number of detected alpha events.

The simulation provided the efficiencies for bulk and surface alphas in titanium. For this particular analysis, the titanium sample was modelled as a sheet with dimensions of 30 cm × 15 cm and a thickness of 4.9 mm, matching the dimensions of the assayed titanium. The efficiencies for the detected alphas, focusing on two radon progenies: ^{210}Po and ^{210}Pb, are shown in Table 6.2.

Isotope	Energy (keV)	Bulk efficiency $\varepsilon_{\text{bulk}}$	Surface efficiency $\boldsymbol{\varepsilon}_{\text{surf}}$
Po-210	5304	0.000715	0.486
Pb-210	3792	0.000377	0.503

Table 6.2 *Table showing the efficiencies for bulk and surface alphas of two radon progeny in a titanium sheet that has 30 cm × 15 cm with a thickness of 4.9 mm.*

The detected yields for each of these contributions reflect the activity level of the radionuclide in the gas, its decay branching ratio (which determines the probability of emitting alpha particles), and the detector efficiency at that energy, which affects how well the alpha particles are detected. For this titanium assay, the calculated surface activity is 0.0364 ± 0.0073 Bq/m^2, and the bulk activity is 0.962 ± 0.240 Bq/kg for ^{210}Po decays. In general, when assaying a sample using the UltraLo-1800 for a rare-event search experiment, we provide the quoted values for the sample's surface and bulk activities in Bq/m^2 and Bq/kg respectively.

6.4.4 Characterisation of cleanliness procedures

Assay of copper plate-out and activity

To investigate and improve cleaning procedures, measurements of surface and bulk alpha particle emissions from copper sheeting were conducted to meet future requirements for rare event searches. An ultra-pure electroformed copper sheet

was used as the sample in this investigation, and it was evaluated both before and after extended exposure to environmental radon, allowing ^{210}Po to accumulate.

The copper sheet, measuring 43 cm × 43 cm with a thickness of 0.6 mm, was positioned at the centre of the PTFE sample tray for measurements. The dimensions of the copper were purposely chosen to maximise detection efficiency and reduce background contributions from the sample tray by optimising the ratio of the sample to tray surface areas.

Before being inserted into the detector, the copper sheet was carefully cleaned with isopropyl alcohol (IPA) and left to air dry. IPA was used as a starting point for cleaning, despite its limited effectiveness in removing all dust and contamination. As shown in Figure 6.17, the results yielded activities of 0.247 ± 0.024 mBq for ^{210}Po, and the surface activity of the sample was measured at 0.137 ± 0.013 μBq/cm^2, as detailed in Table 6.3.

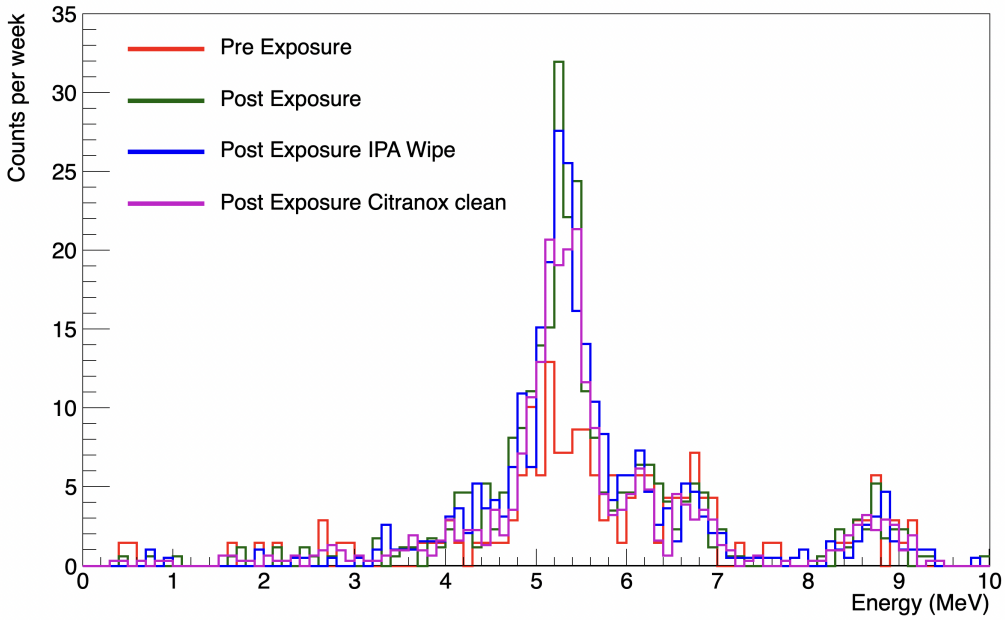

Figure 6.17 *Spectra of energy deposition from alpha particles originating from radon plate-out on a copper sample: before exposure to radon-contaminated air in the laboratory (red), 458 days after exposure (green), after cleaning with an IPA wipe (blue), and following cleaning with Citranox (purple). The corresponding computed surface activities for each stage are shown in Table 6.3.*

The copper sheet was then placed in the BUGS cleanroom, where it was exposed to 2.30 ± 0.03 Bq/m^3 of radon for 458 days [267]. This exposure duration was chosen based on prior experience with radon exposure and was designed to facilitate significant plate-out of radon progeny, including ^{210}Po, onto the

copper surface, thereby increasing the activity levels. The sample was then reinserted into the detector without further cleaning, and measurements were conducted over 15 days. A significant increase in activity was observed, with ^{210}Po detected at 0.504 ± 0.022 mBq, and a corresponding surface ^{210}Po alpha activity of approximately 0.280 ± 0.012 μBq/cm^2.

Subsequently, the sample was cleaned again with IPA and allowed to air dry. In the same region of interest, this resulted in a measured activity of 0.485 ± 0.020 mBq, with a corresponding surface activity of 0.269 ± 0.011 μBq/cm^2. Following this, the copper sheet was cleaned with Citranox [268], yielding an observed ^{210}Po activity of 0.336 ± 0.013 mBq, or a surface activity of 0.187 ± 0.007 μBq/cm^2. Comparing the results after the two cleaning methods, it was found that Citranox was more effective than IPA at removing ^{210}Po contamination from the copper surface. This finding is consistent with previous research [269, 270].

Effectiveness of cleaning

At various stages of the copper sample's treatment, the ^{210}Po surface activities were summarised in Table 6.3. It is important to note that the main effect of these cleaning techniques is on surface contamination; bulk activity is not expected to be significantly impacted.

Potential reasons for the remaining alpha activity after cleaning with Citranox could be due to the embedded ^{210}Po within the copper bulk, which is not removed by surface cleaning. Additionally, the copper's microstructures or porosity may trap contaminants, making them less susceptible to cleaning agents.

Future research will focus on optimising the cleaning process by combining mechanical and chemical cleaning methods. This will include investigating the effectiveness of ultrasonic cleaning in conjunction with chemical agents, potentially improving the removal of embedded contaminants. Furthermore, systematic research must be conducted to thoroughly assess the effectiveness of various cleaning techniques on a range of materials commonly used in detector construction.

Overall, the alpha particle emissions from the copper surface were successfully reduced by our cleaning techniques. However, despite the use of Citranox acid wipes—which were shown to be more effective than IPA at reducing alpha activity [269]—the alpha activity remained higher than what is preferred for sensitive

Table 6.3 *The measured activities of ^{210}Po emanating from an ultra-pure copper sheet, along with the implications of each state for cleanliness procedures. Data were collected by Christopher Tooth and analysed by Anh Nguyen.*

Name	**Description**	**^{210}Po Activity (μBq/cm^2)**	**Implications**
Pre-exposure	Assayed when the copper sheet first arrived at the laboratory, without exposure to air.	0.137 ± 0.013	Baseline measurement for comparison with subsequent measurements.
Post-exposure	Assayed after the copper sheet was left in the laboratory for 458 days.	0.280 ± 0.012	Demonstrates an increase in activity due to radon exposure.
Post-exposure IPA wipe	Assayed after wiping the post-exposure copper sheet with IPA.	0.269 ± 0.011	Indicates IPA's modest effectiveness in reducing activity.
Post-exposure Citranox clean	Assayed after wiping the post-exposure copper with IPA, then Citranox acid.	0.187 ± 0.007	Reveals a significant reduction in activity, highlighting Citranox's superior cleaning efficiency.

detectors. Consequently, further optimisation of the cleaning process is needed. Table 6.3 has identified that certain cleaning methods are not as effective as we hope they are.

6.5 Conclusion

It has been determined that the XIA UltraLo-1800 detector, housed within the Boulby UnderGround Screening (BUGS) facility, can sustain stable internal backgrounds over long periods of time. Stability is crucial for detecting low levels of radioactivity in materials used for rare-event searches.

Understanding and reducing contamination in detector materials requires the ability to distinguish between bulk and surface alpha emissions, which was achieved using a Geant4 simulation model. This model replicates the behaviour of alpha particles emitted from both the surface and bulk, providing insights into how the depth of emission influences detection probabilities. The fits to various radon progeny contaminants have shown excellent agreement with the simulation, as demonstrated with the ^{210}Po calibration and titanium data.

Operating in a deep underground laboratory, which effectively shields the detector from cosmic ray-induced backgrounds, has significantly contributed to this improvement. Additionally, the UltraLo-1800 detector has been employed to assess the effectiveness of various surface-cleaning methods for materials frequently used in particle physics experiments.

In this study, we validated the predictions of our Geant4 simulation model by demonstrating the UltraLo-1800 detector's capability to accurately monitor both surface and bulk alpha emissions. This capability establishes the UltraLo-1800 as an essential component of the material screening program at the BUGS facility. The detector has already been used to assay titanium plates for the LZ experiment and is expected to play an even more significant role in upcoming material assays for LZ's successor, the XLZD consortium, as part of the BUGS facility.

Chapter 7

Conclusions

This thesis presents the author's contributions to the LZ dark matter search and advancements in low-background techniques at Boulby Laboratory.

As part of the LZ collaboration, the author contributed to ensuring detector stability and maintaining data quality as a PMT supervisor during active data collection, as well as performing PMT testing and calibration during offline periods. Beyond the primary WIMP search, the work expanded to explore other signals expected in the electron recoil channel of the LZ detector, including axion-like particles, hidden photons, and mirror dark matter. Using data from LZ's first science run (60 live days and 5.5 tonnes fiducial mass), significant areas of the parameter space for these models were ruled out. While no events beyond expectations from known background sources were observed, future runs with higher exposure are expected to improve sensitivities and impose stricter constraints on these models, or reveal a discovery!

In the broader context of direct detection, enhancing detector sensitivity remains a critical priority. This thesis also highlights efforts to advance material assaying techniques, particularly at the Boulby Underground Screening (BUGS) facility, which supports rare-event search experiments like LZ. The addition of XIA UltraLo-1800 alpha particle counters has significantly improved the facility's assaying capabilities, enabling more precise characterisation of residual radio-contaminants in detector materials. For future experiments, such as those planned by the XLZD consortium, the BUGS facility will play a key role in providing essential material assaying support for next-generation detectors.

The collective efforts described in this thesis - ruling out parameter space for dark matter models and advancing low-background techniques - represent meaningful steps toward the ultimate goal of uncovering the properties of dark matter.

Bibliography

[1] J. Aalbers *et al.* (LZ), Phys. Rev. D **108**, 072006 (2023), arXiv:2307.15753 [hep-ex].

[2] S. E. M. Ahmed Maouloud *et al.*, (2024), arXiv:2408.06925 [physics.ins-det].

[3] W. Thomson and B. Kelvin, *Baltimore Lectures on Molecular Dynamics and the Wave Theory of Light* (2010).

[4] H. Poincare, Popular Astronomy **14**, 475 (1906).

[5] F. Zwicky, **86**, 217 (1937).

[6] H. Andernach and F. Zwicky, "English and spanish translation of zwicky's (1933) the redshift of extragalactic nebulae," (2017), arXiv:1711.01693 [astro-ph.IM].

[7] M. Schwarzschild, **59**, 273 (1954).

[8] V. C. Rubin and W. K. Ford, Jr., Astrophys. J. **159**, 379 (1970).

[9] V. C. Rubin, J. Ford, W. K., and N. Thonnard, **225**, L107 (1978).

[10] A. Bosma, *The distribution and kinematics of neutral hydrogen in spiral galaxies of various morphological types*, Ph.D. thesis, University of Groningen, Netherlands (1978).

[11] T. S. van Albada, J. N. Bahcall, K. Begeman, and R. Sancisi, **295**, 305 (1985).

[12] P. Schneider, J. Ehlers, and E. E. Falco, *Gravitational Lenses* (1992).

[13] A. Einstein, Science **84**, 506 (1936).

[14] J. D. Cohn, C. S. Kochanek, B. A. McLeod, and C. R. Keeton, **554**, 1216 (2001), arXiv:astro-ph/0008390 [astro-ph].

[15] L. V. E. Koopmans and T. Treu, The Astrophysical Journal **568**, L5 (2002).

[16] D. Clowe, M. Bradac, A. H. Gonzalez, M. Markevitch, S. W. Randall, C. Jones, and D. Zaritsky, Astrophys. J. Lett. **648**, L109 (2006), arXiv:astro-ph/0608407.

[17] D. Clowe, M. Bradač, A. H. Gonzalez, M. Markevitch, S. W. Randall, C. Jones, and D. Zaritsky, The Astrophysical Journal **648**, L109 (2006).

[18] A. A. Penzias and R. W. Wilson, **142**, 419 (1965).

[19] D. J. Fixsen, E. S. Cheng, J. M. Gales, J. C. Mather, R. A. Shafer, and E. L. Wright, **473**, 576 (1996), arXiv:astro-ph/9605054 [astro-ph].

[20] G. Hinshaw *et al.*, The Astrophysical Journal Supplement Series **208**, 19 (2013).

[21] D. N. Spergel *et al.* (WMAP), Astrophys. J. Suppl. **148**, 175 (2003), arXiv:astro-ph/0302209.

[22] N. Aghanim *et al.* (Planck), Astron. Astrophys. **641**, A6 (2020), [Erratum: Astron.Astrophys. 652, C4 (2021)], arXiv:1807.06209 [astro-ph.CO].

[23] N. Aghanim *et al.* (Planck), Astron. Astrophys. **641**, A6 (2020), [Erratum: Astron.Astrophys. 652, C4 (2021)], arXiv:1807.06209 [astro-ph.CO].

[24] L. A. Kofman, N. Y. Gnedin, and N. A. Bahcall, Astrophys. J. **413**, 1 (1993).

[25] V. Springel *et al.*, Nature **435**, 629 (2005), arXiv:astro-ph/0504097.

[26] L. A. Kofman, N. Y. Gnedin, and N. A. Bahcall, **413**, 1 (1993).

[27] S. D. McDermott, H.-B. Yu, and K. M. Zurek, Phys. Rev. D **83**, 063509 (2011), arXiv:1011.2907 [hep-ph].

[28] A. D. Dolgov, S. L. Dubovsky, G. I. Rubtsov, and I. I. Tkachev, Physical Review D **88** (2013), 10.1103/physrevd.88.117701.

[29] E. Polisensky and M. Ricotti, Phys. Rev. D **83**, 043506 (2011), arXiv:1004.1459 [astro-ph.CO].

[30] A. Klypin, A. V. Kravtsov, O. Valenzuela, and F. Prada, The Astrophysical Journal **522**, 82–92 (1999).

[31] B. Moore, S. Ghigna, F. Governato, G. Lake, T. Quinn, J. Stadel, and P. Tozzi, **524**, L19 (1999), arXiv:astro-ph/9907411 [astro-ph].

[32] P. Bode, J. P. Ostriker, and N. Turok, The Astrophysical Journal **556**, 93–107 (2001).

[33] V. Acciari *et al.*, Physics of the Dark Universe **22**, 38–47 (2018).

[34] D. Harvey, R. Massey, T. Kitching, A. Taylor, and E. Tittley, Science **347**, 1462–1465 (2015).

[35] D. N. Schramm and M. S. Turner, Reviews of Modern Physics **70**, 303–318 (1998).

[36] R. N. Mohapatra and V. L. Teplitz, Phys. Lett. B **462**, 302 (1999), arXiv:astro-ph/9902085.

[37] D. S. Graff and K. Freese, Astrophys. J. Lett. **467**, L65 (1996), arXiv:astro-ph/9602051.

[38] K. Freese, B. D. Fields, and D. S. Graff, in *MPA / ESO Workshop on the First Stars*, ESO Astrophysics Symposia European Southern Observatory (2000) pp. 18–23, arXiv:astro-ph/0002058.

[39] C. Alcock *et al.* (MACHO), Astrophys. J. **542**, 281 (2000), arXiv:astro-ph/0001272.

[40] R. Ansari, in *International Conference on Cosmic Rays and Dark Matter* (2004) arXiv:astro-ph/0407583.

[41] K. Freese, Int. J. Mod. Phys. **1**, 325 (2017), arXiv:1701.01840 [astro-ph.CO].

[42] J. Silk *et al.*, *Particle Dark Matter: Observations, Models and Searches*, edited by G. Bertone (Cambridge Univ. Press, Cambridge, 2010).

[43] P. Nath and R. L. Arnowitt, in *8th Les Rencontres de Physique de la Vallee d'Aoste: Results and Perspectives in Particle Physics* (1994) arXiv:hep-ph/9406403.

[44] G. Servant and T. M. P. Tait, Nucl. Phys. B **650**, 391 (2003), arXiv:hep-ph/0206071.

[45] D. Hooper and S. Profumo, Phys. Rept. **453**, 29 (2007), arXiv:hep-ph/0701197.

[46] D. Scott, in *International School of Physics "Enrico Fermi" in collaboration with the summer schools ISAPP: Neutrino Physics, Astrophysics and Cosmology* (2024) arXiv:2402.16243 [astro-ph.CO].

[47] M. Aker *et al.* (KATRIN), Nature Phys. **18**, 160 (2022), arXiv:2105.08533 [hep-ex].

[48] R. D. Peccei and H. R. Quinn, Phys. Rev. Lett. **38**, 1440 (1977).

[49] W. Yang, Y. Sun, Y. Wang, K. Schutz, Y. Li, C. Leung, W. Hu, S. Shu, K. Masui, and X. Chen, (2025), arXiv:2502.08913 [astro-ph.CO].

[50] P. Arias, D. Cadamuro, M. Goodsell, J. Jaeckel, J. Redondo, and A. Ringwald, JCAP **06**, 013 (2012), arXiv:1201.5902 [hep-ph].

[51] J. Alexander *et al.* (2016) arXiv:1608.08632 [hep-ph].

[52] B. A. Dobrescu, Phys. Rev. Lett. **94**, 151802 (2005), arXiv:hep-ph/0411004.

[53] L. D. Duffy and K. van Bibber, New J. Phys. **11**, 105008 (2009), arXiv:0904.3346 [hep-ph].

[54] O. Baker, A. Afanasev, T. Lagouri, J. Pan, and C. Weber, Symmetry **14**, 2238 (2022).

[55] M. Fabbrichesi, E. Gabrielli, and G. Lanfranchi, (2020), 10.1007/978-3-030-62519-1, arXiv:2005.01515 [hep-ph].

[56] D. V. Naumov, EPJ Web Conf. **207**, 04004 (2019), arXiv:1901.00151 [hep-ph].

[57] R. Foot, Int. J. Mod. Phys. A **29**, 1430013 (2014), arXiv:1401.3965 [astro-ph.CO].

[58] B. Holdom, Phys. Lett. B **166**, 196 (1986).

[59] R. Foot, H. Lew, and R. R. Volkas, Phys. Lett. B **272**, 67 (1991).

[60] R. Foot and R. R. Volkas, Phys. Rev. D **70**, 123508 (2004), arXiv:astro-ph/0407522.

[61] I.-M. Gregor and A. Straessner, "The LHC Detectors," in *The Large Hadron Collider. Harvest of Run 1*, edited by T. Schörner-Sadenius (2015) pp. 57–94.

[62] M. Aaboud *et al.* (ATLAS), Eur. Phys. J. C **77**, 393 (2017), arXiv:1704.03848 [hep-ex].

[63] A. M. Sirunyan *et al.* (CMS), Eur. Phys. J. C **81**, 13 (2021), [Erratum: Eur.Phys.J.C 81, 333 (2021)], arXiv:2008.04735 [hep-ex].

[64] A. M. Sirunyan *et al.* (CMS), JHEP **03**, 025 (2020), arXiv:1908.01713 [hep-ex].

[65] C. Pérez de los Heros, Symmetry **12**, 1648 (2020), arXiv:2008.11561 [astro-ph.HE].

[66] A. Albert *et al.* (Fermi-LAT, DES), Astrophys. J. **834**, 110 (2017), arXiv:1611.03184 [astro-ph.HE].

[67] R. Abbasi *et al.* (IceCube), Phys. Rev. D **108**, 102004 (2023), arXiv:2303.13663 [astro-ph.HE].

[68] M. G. Aartsen *et al.* (IceCube), Eur. Phys. J. C **77**, 146 (2017), [Erratum: Eur.Phys.J.C 79, 214 (2019)], arXiv:1612.05949 [astro-ph.HE].

[69] A. Albert *et al.* (ANTARES), Phys. Lett. B **805**, 135439 (2020), arXiv:1912.05296 [astro-ph.HE].

[70] L. Goodenough and D. Hooper, (2009), arXiv:0910.2998 [hep-ph].

[71] R. Bartels, S. Krishnamurthy, and C. Weniger, Phys. Rev. Lett. **116**, 051102 (2016), arXiv:1506.05104 [astro-ph.HE].

[72] I. Cholis, D. P. Finkbeiner, L. Goodenough, and N. Weiner, JCAP **12**, 007 (2009), arXiv:0810.5344 [astro-ph].

[73] M. Aguilar *et al.* (AMS), Phys. Rev. Lett. **110**, 141102 (2013).

[74] M. Aguilar *et al.* (AMS), Phys. Rev. Lett. **117**, 091103 (2016).

[75] F. Mayet *et al.*, Phys. Rept. **627**, 1 (2016), arXiv:1602.03781 [astro-ph.CO].

[76] M. C. Smith *et al.*, Mon. Not. Roy. Astron. Soc. **379**, 755 (2007), arXiv:astro-ph/0611671.

[77] R. Essig, J. Mardon, and T. Volansky, Phys. Rev. D **85**, 076007 (2012), arXiv:1108.5383 [hep-ph].

[78] M. Schumann, J. Phys. G **46**, 103003 (2019), arXiv:1903.03026 [astro-ph.CO].

[79] R. Bernabei *et al.*, Nucl. Phys. Atom. Energy **19**, 307 (2018), arXiv:1805.10486 [hep-ex].

[80] J. Amaré *et al.*, Moscow Univ. Phys. Bull. **77**, 322 (2022).

[81] G. Adhikari *et al.* (COSINE-100), Phys. Rev. Lett. **123**, 031302 (2019), arXiv:1903.10098 [astro-ph.IM].

[82] Y. S. Yoon *et al.* (KIMS), JHEP **06**, 011 (2016), arXiv:1604.01825 [hep-ex].

[83] I. Arnquist *et al.* (DAMIC-M), SciPost Phys. Proc. **12**, 014 (2023), arXiv:2210.12070 [hep-ex].

[84] L. Barak *et al.* (SENSEI), Phys. Rev. Lett. **125**, 171802 (2020), arXiv:2004.11378 [astro-ph.CO].

[85] Z. Y. Zhang *et al.* (CDEX), Phys. Rev. Lett. **129**, 221301 (2022), arXiv:2206.04128 [hep-ex].

[86] Q. Arnaud *et al.* (EDELWEISS), Phys. Rev. Lett. **125**, 141301 (2020), arXiv:2003.01046 [astro-ph.GA].

[87] D. W. Amaral *et al.* (SuperCDMS), Phys. Rev. D **102**, 091101 (2020), arXiv:2005.14067 [hep-ex].

[88] R. Agnese *et al.* (SuperCDMS), Phys. Rev. D **99**, 062001 (2019), arXiv:1808.09098 [astro-ph.CO].

[89] G. Angloher *et al.* (CRESST), Eur. Phys. J. C **76**, 25 (2016), arXiv:1509.01515 [astro-ph.CO].

[90] R. Ajaj *et al.* (DEAP), Phys. Rev. D **100**, 022004 (2019), arXiv:1902.04048 [astro-ph.CO].

[91] K. Abe *et al.* (XMASS), Phys. Lett. B **789**, 45 (2019), arXiv:1804.02180 [astro-ph.CO].

[92] M. Schumann, JINST **9**, C08004 (2014), arXiv:1405.7600 [astro-ph.IM].

[93] P. Agnes *et al.* (DarkSide), Phys. Rev. D **98**, 102006 (2018), arXiv:1802.07198 [astro-ph.CO].

[94] D. N. McKinsey *et al.*, J. Phys. Conf. Ser. **203**, 012026 (2010).

[95] D. S. Akerib *et al.* (LZ), Nucl. Instrum. Meth. A **953**, 163047 (2020), arXiv:1910.09124 [physics.ins-det].

[96] E. Aprile *et al.* (XENON), (2024), arXiv:2402.10446 [physics.ins-det].

[97] Y. Meng *et al.* (PandaX-4T), Phys. Rev. Lett. **127**, 261802 (2021), arXiv:2107.13438 [hep-ex].

[98] C. Amole *et al.* (PICO), Phys. Rev. D **100**, 022001 (2019), arXiv:1902.04031 [astro-ph.CO].

[99] E. Behnke *et al.*, Astropart. Phys. **90**, 85 (2017), arXiv:1611.01499 [hep-ex].

[100] J. B. R. Battat *et al.* (DRIFT), Astropart. Phys. **91**, 65 (2017), arXiv:1701.00171 [astro-ph.IM].

[101] N. Du (ADMX), Springer Proc. Phys. **245**, 17 (2020).

[102] D. F. Jackson Kimball *et al.*, Springer Proc. Phys. **245**, 105 (2020), arXiv:1711.08999 [physics.ins-det].

[103] N. F. Bell, P. Cox, M. J. Dolan, J. L. Newstead, and A. C. Ritter, Phys. Rev. D **109**, L091902 (2024), arXiv:2305.04690 [hep-ph].

[104] S. A. Hertel, A. Biekert, J. Lin, V. Velan, and D. N. McKinsey, Phys. Rev. D **100**, 092007 (2019), arXiv:1810.06283 [physics.ins-det].

[105] D. S. Akerib *et al.*, Phys. Procedia **61**, 74 (2015).

[106] H. Araujo (ZEPLIN-III), AIP Conf. Proc. **1441**, 506 (2012).

[107] V. Chepel and H. Araujo, JINST **8**, R04001 (2013), arXiv:1207.2292 [physics.ins-det].

[108] V. Chepel and H. Araújo, Journal of Instrumentation **8**, R04001 (2013).

[109] A. Hitachi, T. Doke, and A. Mozumder, Phys. Rev. B **46**, 11463 (1992).

[110] M. Szydagis *et al.*, Instruments **5**, 13 (2021), arXiv:2102.10209 [hep-ex].

[111] L. Baudis, P. Sanchez-Lucas, and K. Thieme, Eur. Phys. J. C **81**, 1060 (2021), arXiv:2109.07151 [physics.ins-det].

[112] G. Anton *et al.* (EXO-200), Phys. Rev. C **101**, 065501 (2020), arXiv:1908.04128 [physics.ins-det].

[113] T. Shutt, C. E. Dahl, J. Kwong, A. Bolozdynya, and P. Brusov, Nucl. Instrum. Meth. A **579**, 451 (2007), arXiv:astro-ph/0608137.

[114] D. S. Akerib *et al.* (LUX), (2016), arXiv:1608.05381 [physics.ins-det].

[115] M. Berger, J. Hubbell, S. Seltzer, J. Coursey, and D. Zucker, en"Xcom: Photon cross section database (version 1.2)," (1999).

[116] M. Szydagis, N. Barry, K. Kazkaz, J. Mock, D. Stolp, M. Sweany, M. Tripathi, S. Uvarov, N. Walsh, and M. Woods, JINST **6**, P10002 (2011), arXiv:1106.1613 [physics.ins-det].

[117] M. Szydagis *et al.*, (2022), arXiv:2211.10726 [hep-ex].

[118] A. al Mulsahi, *Searches for rare nuclear decays in the LUX-ZEPLIN experiment*, Ph.D. thesis, University of Oxford (2023).

[119] T. Doke, A. Hitachi, J. Kikuchi, K. Masuda, H. Okada, and E. Shibamura, Jap. J. Appl. Phys. **41**, 1538 (2002).

[120] P. Sorensen and C. E. Dahl, Phys. Rev. D **83**, 063501 (2011).

[121] C. E. Dahl, *The physics of background discrimination in liquid xenon, and first results from Xenon10 in the hunt for WIMP dark matter*, Ph.D. thesis, Princeton U. (2009).

[122] F. Bezrukov, F. Kahlhoefer, and M. Lindner, Astroparticle Physics **35**, 119 (2011).

[123] J. Aalbers *et al.* (LZ), Phys. Rev. Lett. **131**, 041002 (2023), arXiv:2207.03764 [hep-ex].

[124] B. J. Mount *et al.*, (2017), arXiv:1703.09144 [physics.ins-det].

[125] D. Y. Akimov, A. I. Bolozdynya, Y. V. Efremenko, V. A. Kaplin, A. V. Khromov, Y. A. Melikyan, and V. V. Sosnovtsev, Nucl. Instrum. Meth. A **794**, 1 (2015), arXiv:1504.07651 [physics.ins-det].

[126] F. Neves, A. Lindote, A. Morozov, V. Solovov, C. Silva, P. Bras, J. P. Rodrigues, and M. I. Lopes, JINST **12**, P01017 (2017), arXiv:1612.07965 [physics.ins-det].

[127] R. Linehan *et al.*, Nucl. Instrum. Meth. A **1031**, 165955 (2022), arXiv:2106.06622 [physics.ins-det].

[128] S. J. Haselschwardt, S. Shaw, H. N. Nelson, M. S. Witherell, M. Yeh, K. T. Lesko, A. Cole, S. Kyre, and D. T. White, Nucl. Instrum. Meth. A **937**, 148 (2019), arXiv:1808.05595 [physics.ins-det].

[129] W. Turner, A. Baxter, H. J. Birch, B. Boxer, S. Burdin, E. Fraser, A. Greenall, S. Powell, and P. Sutcliffe, Nucl. Instrum. Meth. A **1010**, 165551 (2021), arXiv:2102.06281 [physics.ins-det].

[130] D. S. Akerib *et al.* (LUX), Phys. Rev. D **93**, 072009 (2016), arXiv:1512.03133 [physics.ins-det].

[131] M. Arthurs, D. Q. Huang, C. Amarasinghe, E. Miller, and W. Lorenzon, (2020), arXiv:2009.06069 [physics.ins-det].

[132] K. Pushkin *et al.*, Nucl. Instrum. Meth. A **903**, 267 (2018), arXiv:1805.11306 [physics.ins-det].

[133] V. N. Solovov *et al.*, IEEE Trans. Nucl. Sci. **59**, 3286 (2012), arXiv:1112.1481 [physics.ins-det].

[134] D. S. Akerib *et al.* (LUX), JINST **13**, P02001 (2018), arXiv:1710.02752 [physics.ins-det].

[135] J. Aalbers *et al.* (LZ), (2024), arXiv:2406.12874 [physics.ins-det].

[136] J. B. Albert *et al.* (EXO-200), Phys. Rev. C **92**, 045504 (2015), arXiv:1506.00317 [nucl-ex].

[137] J. I. Collar, Phys. Rev. Lett. **110**, 211101 (2013), arXiv:1303.2686 [physics.ins-det].

[138] D. S. Akerib *et al.* (LZ), Eur. Phys. J. C **80**, 1044 (2020), [Erratum: Eur.Phys.J.C 82, 221 (2022)], arXiv:2006.02506 [physics.ins-det].

[139] N. I. Chott and R. W. Schnee (LUX-ZEPLIN), AIP Conf. Proc. **2908**, 080004 (2023), arXiv:2211.11857 [physics.ins-det].

[140] V. A. Kudryavtsev, P. Zakhary, and B. Easeman, Nucl. Instrum. Meth. A **972**, 164095 (2020), arXiv:2005.02499 [physics.ins-det].

[141] K. T. Lesko, Phys. Procedia **61**, 542 (2015).

[142] M. L. Cherry, M. Deakyne, K. Lande, C. K. Lee, R. I. Steinberg, B. Cleveland, and E. J. Fenyves, Phys. Rev. D **27**, 1444 (1983).

[143] F. E. Gray, C. Ruybal, J. Totushek, D. M. Mei, K. Thomas, and C. Zhang, Nucl. Instrum. Meth. A **638**, 63 (2011), arXiv:1007.1921 [nucl-ex].

[144] D. S. Akerib *et al.* (LZ), Astropart. Phys. **116**, 102391 (2020), arXiv:1904.02112 [physics.ins-det].

[145] J. Aalbers *et al.* (LZ), Phys. Rev. D **105**, 082004 (2022), arXiv:2201.02858 [hep-ex].

[146] D. S. Akerib *et al.* (LZ), Phys. Rev. D **101**, 052002 (2020), arXiv:1802.06039 [astro-ph.IM].

[147] L. Si *et al.* (PandaX), Research **2022**, 9798721 (2022), arXiv:2205.12809 [nucl-ex].

[148] A. Gando *et al.* (KamLAND-Zen), Phys. Rev. C **85**, 045504 (2012), arXiv:1201.4664 [hep-ex].

[149] J. B. Albert *et al.* (EXO-200), Phys. Rev. C **89**, 015502 (2014), arXiv:1306.6106 [nucl-ex].

[150] E. Aprile *et al.* (XENON), Nature **568**, 532 (2019), arXiv:1904.11002 [nucl-ex].

[151] J. R. de Laeter, J. K. Böhlke, P. D. Bièvre, H. Hidaka, H. S. Peiser, K. J. R. Rosman, and P. D. P. Taylor, Pure and Applied Chemistry **75**, 683 (2003).

[152] J. Aalbers *et al.* (LZ), Nucl. Instrum. Meth. A **1068**, 169712 (2024), arXiv:2405.14732 [physics.ins-det].

[153] D. S. Akerib *et al.* (LUX), Phys. Rev. D **102**, 092004 (2020), arXiv:2004.07791 [physics.ins-det].

[154] J. Aalbers *et al.* (LZ), Phys. Rev. D **108**, 012010 (2023), arXiv:2211.17120 [hep-ex].

[155] N. Vinyoles, A. M. Serenelli, F. L. Villante, S. Basu, J. Bergström, M. C. Gonzalez-Garcia, M. Maltoni, C. Peña Garay, and N. Song, Astrophys. J. **835**, 202 (2017), arXiv:1611.09867 [astro-ph.SR].

[156] B. Aharmim *et al.* (SNO), Phys. Rev. C **88**, 025501 (2013), arXiv:1109.0763 [nucl-ex].

[157] M. Agostini *et al.* (Borexino), Phys. Rev. D **100**, 082004 (2019), arXiv:1707.09279 [hep-ex].

[158] L. Baudis, A. Ferella, A. Kish, A. Manalaysay, T. Marrodan Undagoitia, and M. Schumann, JCAP **01**, 044 (2014), arXiv:1309.7024 [physics.ins-det].

[159] M. Schumann, L. Baudis, L. Bütikofer, A. Kish, and M. Selvi, JCAP **10**, 016 (2015), arXiv:1506.08309 [physics.ins-det].

[160] D. S. Akerib *et al.* (LUX), Phys. Rev. D **96**, 112011 (2017), arXiv:1709.00800 [physics.ins-det].

[161] D. Baxter *et al.*, Eur. Phys. J. C **81**, 907 (2021), arXiv:2105.00599 [hep-ex].

[162] R. L. Workman *et al.* (Particle Data Group), PTEP **2022**, 083C01 (2022).

[163] W. A. Rolke, A. M. Lopez, and J. Conrad, Nucl. Instrum. Meth. A **551**, 493 (2005), arXiv:physics/0403059.

[164] G. Cowan, K. Cranmer, E. Gross, and O. Vitells, Eur. Phys. J. C **71**, 1554 (2011), [Erratum: Eur.Phys.J.C 73, 2501 (2013)], arXiv:1007.1727 [physics.data-an].

[165] A. Biekert, *Searching for Sub-Gev Dark Matter with Liquid Xenon and Superfluid Helium*, Ph.D. thesis, UC Berkeley (2023).

[166] G. Cowan, K. Cranmer, E. Gross, and O. Vitells, (2011), arXiv:1105.3166 [physics.data-an].

[167] B. S. Hu, J. Padua-Argüelles, S. Leutheusser, T. Miyagi, S. R. Stroberg, and J. D. Holt, Phys. Rev. Lett. **128**, 072502 (2022), arXiv:2109.00193 [nucl-th].

[168] M. Hoferichter, J. Menéndez, and A. Schwenk, Phys. Rev. D **102**, 074018 (2020), arXiv:2007.08529 [hep-ph].

[169] P. Pirinen, J. Kotila, and J. Suhonen, Nucl. Phys. A **992**, 121624 (2019).

[170] D. S. Akerib *et al.* (LZ), Phys. Rev. D **104**, 092009 (2021), arXiv:2102.11740 [hep-ex].

[171] R. Essig, J. Mardon, and T. Volansky, Physical Review D **85** (2012), 10.1103/physrevd.85.076007.

[172] M. Pospelov, A. Ritz, and M. Voloshin, Physical Review D **78** (2008), 10.1103/physrevd.78.115012.

[173] E. Witten, Commun. Math. Phys. **92**, 455 (1984).

[174] J. P. Conlon, JHEP **05**, 078 (2006), arXiv:hep-th/0602233.

[175] A. Arvanitaki, S. Dimopoulos, S. Dubovsky, N. Kaloper, and J. March-Russell, Phys. Rev. D **81**, 123530 (2010), arXiv:0905.4720 [hep-th].

[176] M. Cicoli, M. Goodsell, and A. Ringwald, JHEP **10**, 146 (2012), arXiv:1206.0819 [hep-th].

[177] M. Bauer, M. Neubert, and A. Thamm, JHEP **12**, 044 (2017), arXiv:1708.00443 [hep-ph].

[178] R. Z. Ferreira, M. C. D. Marsh, and E. Müller, Phys. Rev. Lett. **128**, 221302 (2022).

[179] M. Pospelov, A. Ritz, and M. B. Voloshin, Phys. Rev. D **78**, 115012 (2008), arXiv:0807.3279 [hep-ph].

[180] K. C. Y. Ng, B. M. Roach, K. Perez, J. F. Beacom, S. Horiuchi, R. Krivonos, and D. R. Wik, Phys. Rev. D **99**, 083005 (2019), arXiv:1901.01262 [astro-ph.HE].

[181] R. Laha, J. B. Muñoz, and T. R. Slatyer, Phys. Rev. D **101**, 123514 (2020), arXiv:2004.00627 [astro-ph.CO].

[182] J. W. Foster, M. Kongsore, C. Dessert, Y. Park, N. L. Rodd, K. Cranmer, and B. R. Safdi, Phys. Rev. Lett. **127**, 051101 (2021), arXiv:2102.02207 [astro-ph.CO].

[183] A. E. Nelson and J. Scholtz, Phys. Rev. D **84**, 103501 (2011), arXiv:1105.2812 [hep-ph].

[184] P. W. Higgs, Phys. Rev. Lett. **13**, 508 (1964).

[185] F. Englert and R. Brout, Phys. Rev. Lett. **13**, 321 (1964).

[186] E. C. G. Stueckelberg, Helv. Phys. Acta **11**, 225 (1938).

[187] D. Feldman, Z. Liu, and P. Nath, Phys. Rev. D **75**, 115001 (2007), arXiv:hep-ph/0702123.

[188] K. Arisaka, P. Beltrame, C. Ghag, J. Kaidi, K. Lung, A. Lyashenko, R. D. Peccei, P. Smith, and K. Ye, Astropart. Phys. **44**, 59 (2013), arXiv:1209.3810 [astro-ph.CO].

[189] L. B. Okun, Sov. Phys. JETP **56**, 502 (1982).

[190] F. Brummer and J. Jaeckel, Phys. Lett. B **675**, 360 (2009), arXiv:0902.3615 [hep-ph].

[191] M. Goodsell, J. Jaeckel, J. Redondo, and A. Ringwald, JHEP **11**, 027 (2009), arXiv:0909.0515 [hep-ph].

[192] H. An, M. Pospelov, J. Pradler, and A. Ritz, Phys. Lett. B **747**, 331 (2015), arXiv:1412.8378 [hep-ph].

[193] J. Suzuki, T. Horie, Y. Inoue, and M. Minowa, JCAP **09**, 042 (2015), arXiv:1504.00118 [hep-ex].

[194] M. Silva-Feaver *et al.*, IEEE Trans. Appl. Supercond. **27**, 1400204 (2017), arXiv:1610.09344 [astro-ph.IM].

[195] A. Wagner *et al.* (ADMX), Phys. Rev. Lett. **105**, 171801 (2010), arXiv:1007.3766 [hep-ex].

[196] L. H. Nguyen, A. Lobanov, and D. Horns, JCAP **10**, 014 (2019), arXiv:1907.12449 [hep-ex].

[197] S. Andreas, Frascati Phys. Ser. **56**, 23 (2012), arXiv:1212.4520 [hep-ph].

[198] R. Essig, M. Fernandez-Serra, J. Mardon, A. Soto, T. Volansky, and T.-T. Yu, JHEP **05**, 046 (2016), arXiv:1509.01598 [hep-ph].

[199] A. A. Aguilar-Arevalo *et al.* (MiniBooNE), Phys. Rev. Lett. **118**, 221803 (2017), arXiv:1702.02688 [hep-ex].

[200] D. Curtin, R. Essig, S. Gori, and J. Shelton, JHEP **02**, 157 (2015), arXiv:1412.0018 [hep-ph].

[201] P. Ilten, J. Thaler, M. Williams, and W. Xue, Phys. Rev. D **92**, 115017 (2015), arXiv:1509.06765 [hep-ph].

[202] K. Arisaka *et al.*, Astropart. Phys. **44**, 59 (2013).

[203] E. Aprile *et al.* (XENON100), Phys. Rev. D **96**, 122002 (2017), arXiv:1709.02222 [astro-ph.CO].

[204] K. Abe *et al.* (XMASS), Phys. Lett. B **787**, 153 (2018), arXiv:1807.08516 [astro-ph.CO].

[205] R. Foot, Phys. Lett. B **785**, 403 (2018), arXiv:1804.11018 [hep-ph].

[206] J. D. Clarke and R. Foot, JCAP **01**, 029 (2016), arXiv:1512.06471 [astro-ph.GA].

[207] R. Foot, Phys. Lett. B **789**, 592 (2019), arXiv:1806.04293 [hep-ph].

[208] P. Ciarcelluti and R. Foot, Phys. Lett. B **690**, 462 (2010), arXiv:1003.0880 [astro-ph.CO].

[209] J. D. Clarke and R. Foot, Phys. Lett. B **766**, 29 (2017), arXiv:1606.09063 [hep-ph].

[210] R. Foot, JCAP **04**, 014 (2012), arXiv:1110.2908 [hep-ph].

[211] I. M. Bloch *et al.*, JHEP **06**, 087 (2017).

[212] D. Baxter *et al.*, Eur. Phys. J. C **81**, 907 (2021), 2105.00599.

[213] M. Berger, J. Hubbell, S. Seltzer, J. Coursey, and D. Zucker, "Nist xcom: Photon cross sections database," (2025).

[214] G. Cowan *et al.*, (2011), arXiv:1105.3166 [physics.data-an].

[215] E. Aprile *et al.* (XENON), Phys. Rev. Lett. **129**, 161805 (2022).

[216] E. Aprile *et al.* (XENON), Phys. Rev. Lett. **123**, 251801 (2019).

[217] E. Aprile *et al.* (XENON), Phys. Rev. D **102**, 072004 (2020).

[218] Y. Wang *et al.* (CDEX), Phys. Rev. D **101**, 052003 (2020).

[219] M. Agostini *et al.* (GERDA), Phys. Rev. Lett. **125**, 011801 (2020), [Erratum: Phys.Rev.Lett. 129, 089901 (2022)].

[220] D. S. Akerib *et al.* (LUX), Phys. Rev. Lett. **118**, 261301 (2017).

[221] N. Abgrall *et al.* (Majorana), Phys. Rev. Lett. **118**, 161801 (2017).

[222] C. Fu *et al.* (PandaX-II), Phys. Rev. Lett. **119**, 181806 (2017).

[223] P. Agnes *et al.* (DarkSide Collaboration), Phys. Rev. Lett. **130**, 101002 (2023).

[224] H. An *et al.*, Phys. Lett. B **747**, 331 (2015).

[225] D. S. Akerib *et al.* (LUX), Phys. Rev. D **101**, 012003 (2020), arXiv:1908.03479 [hep-ex].

[226] J. Aalbers *et al.* (LZ), Phys. Rev. Lett. **131**, 041002 (2023).

[227] J. Aalbers *et al.* (LZ Collaboration), (2024), arXiv:2410.17036 [hep-ex].

[228] J. B. Albert *et al.*, Phys. Rev. C **92**, 015503 (2015), arXiv:1503.06241 [physics.ins-det].

[229] W. contributor: Eelsirhc, "Decay chain of uranium 238," (2024).

[230] W. contributor: BatesIsBack, "A modification of the original image to fix the half-life of pb-212," (2011).

[231] U. N. S. C. on the Effects of Atomic Radiation, *Effects of Ionizing Radiation, United Nations Scientific Committee on the Effects of Atomic Radiation (UNSCEAR) 2006 Report, Volume I* (United Nations, 2008).

[232] U. UNSCEAR *et al.*, United Nations Scientific Committee on the Effects of Atomic Radiation (2000).

[233] X. R. Liu, *Low background techniques for the SuperNEMO experiment*, Ph.D. thesis, University College London (2017).

[234] M. Riudavets, M. Garcia de Herreros, B. Besse, and L. Mezquita, Cancers **14** (2022), 10.3390/cancers14133142.

[235] M. A. Tabatabai, Journal of Environmental Quality **18**, 132 (1989).

[236] N. N. D. Center, "Information extracted from the nudat database,," .

[237] V. Schmidt and P. Hamel, Science of The Total Environment **272**, 189 (2001), radon in the Living Environment.

[238] S. Westerdale and P. D. Meyers, Nucl. Instrum. Meth. A **875**, 57 (2017), arXiv:1702.02465 [physics.ins-det].

[239] P. R. Scovell, E. Meehan, S. M. Paling, M. Thiesse, X. Liu, C. Ghag, M. Ginsz, P. Quirin, and D. Ralet, JINST **19**, P01017 (2024), arXiv:2308.03444 [physics.ins-det].

[240] E. Daw *et al.*, EAS Publ. Ser. **53**, 11 (2012), arXiv:1110.0222 [physics.ins-det].

[241] R. Luscher, Eur. Phys. J. C **33**, S968 (2004), arXiv:astro-ph/0305310.

[242] B. Ahmed *et al.*, Astropart. Phys. **19**, 691 (2003), arXiv:hep-ex/0301039.

[243] S. E. Vahsen *et al.*, (2020), arXiv:2008.12587 [physics.ins-det].

[244] W. C. Pettus (DM-Ice), in *12th Conference on the Intersections of Particle and Nuclear Physics* (2015) arXiv:1510.00378 [physics.ins-det].

[245] M. M. Arora *et al.* (NEWS-G), (2024), arXiv:2407.12769 [hep-ex].

[246] L. Balogh *et al.* (NEWS-G), Phys. Rev. D **108**, 112006 (2023), arXiv:2301.05183 [hep-ex].

[247] P. R. Scovell, M. Thiesse, S. Ahmed Maouloud, C. Ghag, and J. Dobson, Frontiers in Physics **11** (2023), 10.3389/fphy.2023.1310146.

[248] I. Lawson, J. Phys. Conf. Ser. **1342**, 012086 (2020).

[249] L. Baudis, A. D. Ferella, A. Askin, J. Angle, E. Aprile, T. Bruch, A. Kish, M. Laubenstein, A. Manalaysay, T. M. Undagoitia, and M. Schumann, Journal of Instrumentation **6**, P08010 (2011).

[250] B. J. Mount *et al.*, Appl. Radiat. Isot. **126**, 130 (2017).

[251] P. Loaiza, V. Brudanin, F. Piquemal, E. Rukhadze, N. Rukhadze, I. Stekl, G. Warot, and M. Zampaolo, AIP Conference Proceedings **1672**, 130002 (2015), https://pubs.aip.org/aip/acp/article-pdf/doi/10.1063/1.4928012/13721135/130002_1_online.pdf.

[252] I. Bandac, S. Borjabad, A. Ianni, R. Nuñez Lagos, C. Pérez, S. Rodríguez, and J. A. Villar, Appl. Radiat. Isot. **126**, 127 (2017).

[253] K. Ichimura *et al.*, PTEP **2023**, 123H01 (2023), arXiv:2308.05302 [physics.ins-det].

[254] P. R. Scovell, M. Thiesse, S. Ahmed Maouloud, C. Ghag, and J. Dobson, Front. in Phys. **11**, 1310146 (2023).

[255] X. LLC, XIA LLC (2013).

[256] S. Ramo, Proc. Ire. **27**, 584 (1939).

[257] S. Agostinelli *et al.*, Nucl. Instrum. Meth. A **505**, 250 (2003).

[258] Spectrum Techniques LLC, `https://www.spectrumtechniques.com`, Accessed: 2023-06-05.

[259] J. Ange, R. Calkins, and A. Posada, JINST **18**, P01027 (2023), arXiv:2209.08002 [physics.ins-det].

[260] Y. A. AKOVALI, Nucl. Data Sheets **77**, 433 (1996).

[261] DeWal Industries Inc, DW 105 Skived PTFE Film, `https://usa.exportersindia.com/dewal-industries-inc/dw-105-skived-ptfe-film-2922713.htm`, Accessed: 2023-06-05.

[262] M. Z. Nakib, J. Cooley, V. E. Guiseppe, B. Kara, H. Qiu, K. Rielage, R. W. Schnee, and S. Scorza, AIP Conf. Proc. **1549**, 78 (2013).

[263] B. D. McNally, S. Coleman, W. K. Warburton, J.-L. Autran, B. M. Clark, J. Cooley, M. S. Gordon, and Z. Zhu, Nucl. Instrum. Meth. A **750**, 96 (2014), arXiv:1401.1845 [physics.ins-det].

[264] K. Abe *et al.* (XMASS), Nucl. Instrum. Meth. A **884**, 157 (2018), arXiv:1707.06413 [physics.ins-det].

[265] W. W. Nazaroff and A. V. Nero, (1988).

[266] R. B. Firestone, V. S. Shirley, C. M. Baglin, S. Y. Chu, and J. Zipkin, (1997).

[267] P. Scovell, "Private communication," (2023).

[268] Alconox, Inc., Citranox: Acid Cleaner and Detergent, `https://alconox.com/products/citranox/`, Accessed: 2023-06-05.

[269] P. R. Scovell, M. Thiesse, S. Ahmed Maouloud, C. Ghag, and J. Dobson, Frontiers in Physics **11** (2023).

[270] M. Stein, D. Bauer, R. Bunker, R. Calkins, J. Cooley, B. Loer, and S. Scorza, Nuclear Instruments and Methods in Physics Research Section A: Accelerators, Spectrometers, Detectors and Associated Equipment **880**, 92 (2018).